Norman

^{40}Ar/^{39}Ar DATING OF BARITE AND CHARACTERIZATION OF ORE FLUIDS AT THE LONE TREE GOLD DEPOSIT, HUMBOLDT COUNTY, NEVADA

By

Cem KAMALI

Submitted in Partial Fulfillment of the Requirements for the
Degree of Master of Science in Geology

Department of Earth and Environmental Science
New Mexico Institute of Mining and Technology
Socorro, NM 87801
July 1996

This thesis is accepted on behalf of the faculty

of the institute by the following committee:

David I. Norman

Advisor

Andrew Campbell

William X. Chávez Jr. 18 July, 1996

July 18 1996

Date

ABSTRACT

The Lone Tree gold deposit, Nevada is hosted in Paleozoic calcareous sedimentary rocks. Mineralization is dominantly controlled by high-angle normal faults and fracture sets, as is alteration. Mineralization occurs in the form of disseminations, micro and macro veins, and as a matrix to angular breccia clasts. The paragenesis of minerals indicate four stages of mineralization. The first stage is identified by brecciated quartz and minor pyrite. The second stage is the main gold stage of mineralization comprising quartz veins, kaolinite, pyrite, marcasite, arsenopyrite, gold, sphalerite, and chalcopyrite. This is overprinted by a third stage economic gold mineralization along with barite and pyrite. Free gold grains in stage 2 occur in a quartz and clay mineral assemblage in association with pyrite. The last stage is supergene mineralization producing covellite, chalcocite, native copper, hematite, and goethite.

Main alteration types are decarbonatization, silicification by multiple generations of silica, and argillization due to the development of kaolinite, illite/smectite, and alunite.

Fluid inclusion and gas composition data indicate multiple sources for fluids that gave rise to main stage gold mineralization. These fluids were magmatic, crustal, and meteoric in origin. Fluid inclusion microthermometry data indicate that fluids had a temperature range of 185 and 411 °C and salinity of 1.2 to 41.4 eq. wt. % NaCl. Halite-bearing fluid inclusions have salinities between 28.6 and 41.4 eq. wt. % NaCl and homogenization of 201 to 362 °C. These high salinity fluids have N_2/Ar ratios greater than that in the atmosphere as well as high CO_2 concentrations suggesting a magmatic contribution to the ore fluids. Nitrogen concentrations are highest in first stage mineralizing fluids, that are analogues to stage 2 fluids in many other ways, indicating even more magmatic input in this stage. Evolved meteoric waters are indicated by low to moderate salinity fluids (1.2-8.1 eq. wt. % NaCl) that had temperatures between 211-300 °C. Evolved meteoric waters were formed by extensive water-rock interaction and fluid mixing. Fractures in stage 2 quartz trapped low salinity (1.4-2.07 eq. wt. % NaCl) fluids, that are very similar to stage 3 fluids, at temperatures of 136-147 °C. Vapor-rich inclusions indicate boiling at high temperatures ranging from 332 to 411 °C and low salinities ranging 1.2 to 5.26 eq. wt. % NaCl.

Compositions of gases on ternary plots such as N_2-CH_4-CO_2, N_2-C_nH_n-CO_2, and CO_2-CH_4-H_2S can reveal boiling trends from least soluble to most soluble gases. This is verified by a model boiling which produced trends analogous to that in the particular ternary plot. The high amounts of total gas concentrations can also indicate fluid boiling.

Stage 3 fluids were primarily unevolved meteoric waters. These fluids had salinities of 1.2 to 1.7 eq. wt. % NaCl and homogenization temperatures between 103 and 174 °C. No evidence for boiling was seen for this stage.

Marcasite in main stage gold mineralization and clay minerals especially kaolinite indicate that gold mineralizing fluids were acidic.

The geochemical characteristics of ore fluids along with mineralogy have been utilized to develop a genetic model for the Lone Tree gold deposit. This model also relates to the genesis of other Carlin-type gold deposits. According to this model, gold is derived from magmatic processes and leached from sedimentary rocks by fluid-rock interaction. Gold is transported as both chloride and bisulfide complexes at varying conditions. Gold precipitation take place in response to change in pH towards alkaline conditions by reaction with calcite in host rocks, H_2S loss, and a decrease in temperature due to fluid boiling and fluid mixing. Hydrostatic pressure fluctuated from 173 to greater than 500 bars throughout the mineralization processes. Vapor pressures of gaseous phases indicate that fluid boiling occurred at pressure of 228 bars corresponding to a depth of 3180 meters. The timing of the main stage gold mineralization is inferred to be early Oligocene on the basis of known K-Ar ages of nearby granodiorite dike.

$^{40}Ar/^{39}Ar$ age dating of barite yielded ages generally with large uncertainties due to the low radiogenic argon yield and lack of sufficient potassium. However, in some cases potassium can be incorporated into barite and $^{40}Ar/^{39}Ar$ analyses can yield apparent ages with high enough precision to allow for geologic considerations of the age data.

TABLE OF CONTENTS

LIST OF FIGURES

LIST OF TABLES

ACKNOWLEDGEMENTS

I would like to express my thanks to Dr. David Norman, the advisor, not only for introducing me to Carlin-type gold deposits culminating with such a fruitful project, but also for his guidance throughout this research. I wish to express my thanks to members of the M. S. thesis committee Drs. Andrew Campbell, and William Chavez for their help and constructive comments. Appreciation is also expressed to Drs. Matthew Heizler and William McIntosh for their assistance in $^{40}Ar/^{39}Ar$ laboratory and for taking their valuable time to review the draft paper of $^{40}Ar/^{39}Ar$ section from which thesis greatly benefited. I also thank John Groff for numerous stimulating discussions on enigmas of the Carlin-type deposits.

My appreciation is also extended to Ibrahim Gundiler, George Austin, and Lynn Brandvold for fire assay, X-ray diffraction, and atomic absorption analyses at the New Mexico Bureau of Mines and Mineral Resources.

I would like to acknowledge Santa Fe Pacific Gold Corporation for funding this project. I also acknowledge a grant from Mustafa Kemal University in Turkiye which allowed me to pursue a master degree at New Mexico Institute of Mining and Technology.

Finally I wish to express my gratefulness to my family for their moral support, understanding, and patience through this study.

INTRODUCTION

The Lone Tree gold deposit is located ~35 miles (56 km) east-southeast of Winnemucca in Humboldt County, Nevada (Fig. 1). This deposit was discovered in 1989. Reserves as of 1994 were ~66.7 million tons of ore at an average grade of 0.06 oz/ton (2.1g/ton), which is equivalent to 4 million oz Au (B. Braginton, per. comm., 1994).

The purpose of this study was to develop a better understanding of the genesis of the Lone Tree gold deposit through a combination of mineralogical, geochemical, and geochronological investigations. This would in turn provide information to better the understanding of the formation of Carlin-type deposits. A genetic model for the occurrence of Carlin-type deposits is very important in mineral exploration if new discoveries are to be made. This work presents a model for the genesis of the Lone Tree deposit based on the results of ore microscopy, fluid inclusion microthermometry, fluid inclusion gas analyses, and experimental dating of barite via the $^{40}Ar/^{39}Ar$ method.

Carlin-type gold deposits (sediment-hosted disseminated deposits) have unique characteristics which distinguish them from the other types of gold deposits. This class of deposits is defined by the occurrence of very fine-grained gold in association with arsenic, antimony, mercury, thallium, and barium in silty carbonate rocks or calcareous sandstones, siltstones, and claystones. High gold/silver

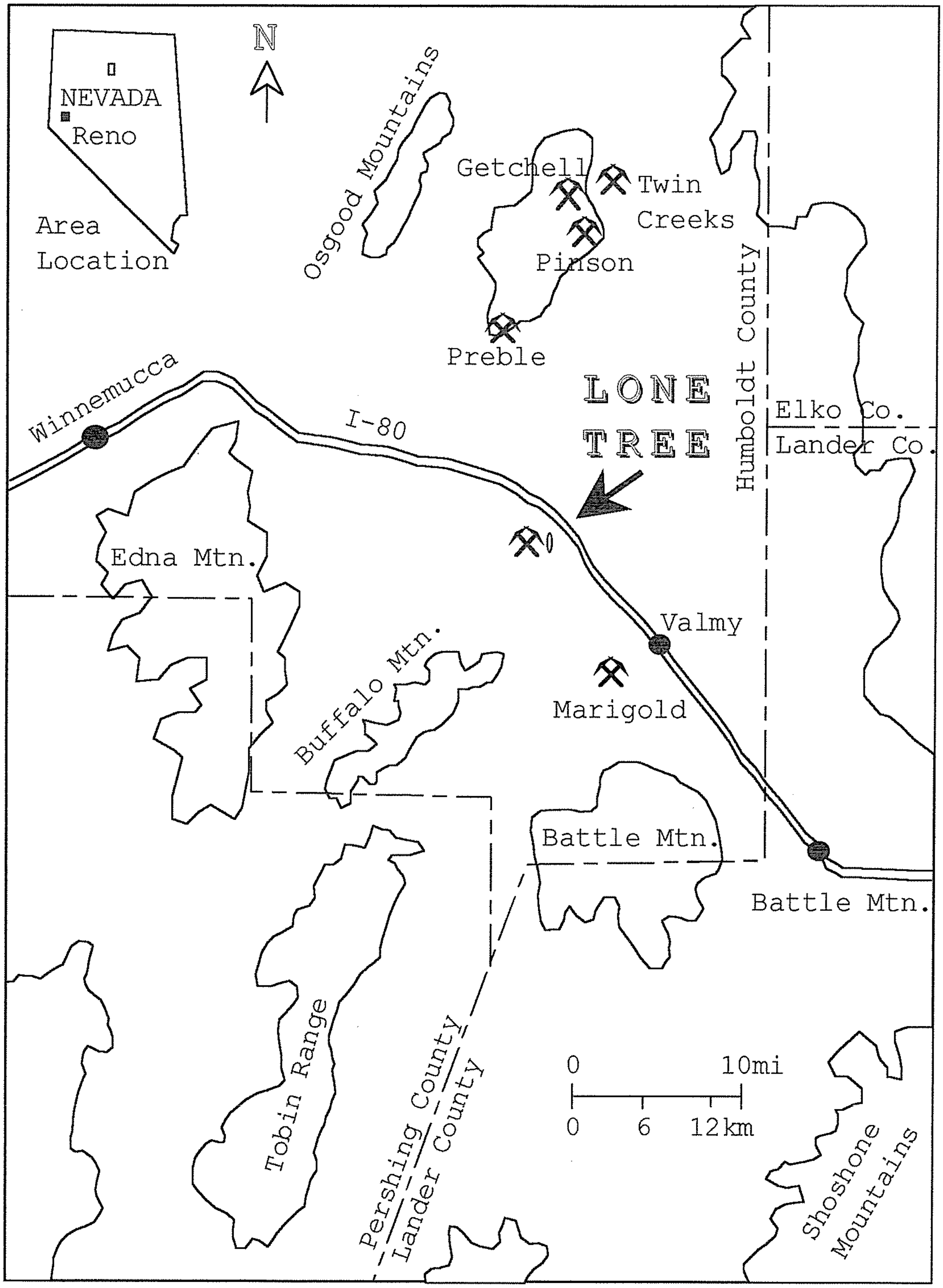

Figure 1. Map showing location of the Lone Tree Mine, Humboldt County, Nevada.

ratios and low concentrations of base metals such as copper, lead, and zinc are also typical. The alteration style typically comprises decarbonatization, silicification in the form of jasperoids or quartz veining, and argillization (Bagby and Berger, 1985; Tooker, 1985; Romberger, 1986; Kuehn and Rose, 1992; Ilchik, 1990; Arehart et al., 1993c; Percival and Radtke, 1994). Mineralization is dominantly controlled by fractures and comprises three distinctive forms as stratabound replacements, high-grade veins, and stockworks (Christensen, 1993).

The paragenesis of mineralization at most of the Carlin-type gold deposits is not well determined because of the very fine-grained nature of minerals and lack of clearly defined crosscutting relations. However, the Lone Tree deposit contains a relatively coarse-grained mineral assemblage that allowed us to establish a well constrained sequence of mineral precipitation. Integrating definitive paragenetic features from a variety of deposits may be useful in constructing a general paragenesis for this type of deposit.

Because of the very fine (micron size) nature of the gold, the location of gold in unoxidized samples from the Carlin-type deposits is controversial. However, electron microprobe analyses by Wells and Mullens (1973) show that gold is concentrated in small pyrite grains and in rims of larger pyrite grains. Less commonly arsenopyrite is also reported to contain gold. More recent, high resolution microscope studies by Bakken et al. (1989) on ores from the Carlin mine show that gold is encapsulated in pyrite, cinnabar, and quartz, but free gold also occurs in association with illite. Currently, the available geochemical data for some of these deposits are insufficient to establish the physico-chemical conditions during gold mineralization and to determine the source of ore forming fluids.

Fluid inclusion studies are limited due to the small size and poor optical characteristics of inclusions in mineralized jasperoids and quartz veins. The largest amount of fluid inclusion data was compiled by Kuehn (1989) and Radtke et al. (1980) for the Carlin deposit. Fluid inclusion measurements by Kuehn (1989) indicate ore-forming fluids were moderately saline, CO_2-rich, nonboiling, and had a temperature range of 185°-245 °C. In contrast, fluid inclusion work by Radtke et al. (1980) shows that moderately saline, CO_2-poor, nonboiling fluids at temperatures of 175°-200 °C were responsible for gold mineralization. Radtke et al. (1980) also pointed out that the temperature and salinity of fluids significantly increased in response to boiling during later stages of mineralization. Additionally, fluid inclusion data for the Jerrit Canyon mine shows that both CO_2-rich brines and dilute CO_2-poor, fluids were responsible for gold-stage mineralization at temperatures of

200°-300 °C (Hofstra et al., 1987; Hofstra et al., 1991). Mixing of these two distinctly different fluids rather than boiling is postulated to lead to the precipitation of minerals.

The debate concerning the origin of gold-mineralizing fluids in the Carlin-type gold deposits has yet to be resolved. Stable isotope geochemistry provides one of the analytical methods to determine the source of sulfur and origin of ore forming fluids. Since gold is closely associated with iron sulfides at Carlin-type deposits, determination of the origin of sulfur in sulfides might pinpoint the source of gold as well. Moreover, hydrogen and oxygen isotope data can help determine the source of mineralizing fluids. Three different sources could be possible for mineralizing fluids such as meteoric, magmatic, and metamorphic. Oxygen and sulfur isotope data for the Alligator Ridge deposit suggest that the ore fluid was dominantly evolved meteoric waters and sulfur was acquired from the sedimentary sulfides (Ilchik, 1990). Similarly, δD for fluids in both Carlin and Cortez deposits showed that the mineralizing fluids were highly evolved meteoric waters (Rye, 1985). Similar sulfur isotopic compositions of pyrite in ore and diagenetic pyrite in unaltered host rock provided evidence that carbonate host rock were the source of sulfur in ore fluids (Rye, 1985; Radtke, 1980). However, Rose and Kuehn (1987) infer that high concentrations of CO_2 in mineralizing fluids at the Carlin deposit were the result of metamorphism at depth. This inference brings up the possibility that metamorphic waters were also incorporated into mineralizing fluids. Sillitoe and Bonham (1990) propose a magmatic source for mineralizing fluids at some of Carlin-type gold deposits considering the depth of formation and spatial association with igneous rocks.

An alternative method to determine the source of hydrothermal fluids is the measurement of gas species such as N_2, Ar, He, CO_2, and CH_4 in fluid inclusions. It has been demonstrated that the relative abundances of gases such as N_2, Ar, and He can be used to determine if gas sources were meteoric, magmatic, or crustal, and if fluid boiling and mixing occurred (Norman et al., 1996; Norman and Musgrave, 1994; Landis and Hofstra, 1991).

Another question related to Carlin-type gold deposits is the timing of gold mineralization. It is unclear if there is a genetic tie between these deposits and periods of igneous activity from the Jurassic to Quaternary, or if ore forming processes were influenced by extensional tectonism in the Miocene. A documentation of the timing of gold mineralization in conjunction with the local and regional geology should help to determine if there is a relationship between the formation of these deposits and tectonic events or magmatism. However, radiometric dating of gold mineralization in Carlin-type deposits has been difficult due to the lack of potassium bearing minerals directly related to ore formation. Furthermore, it has been shown that alunite commonly occurring in these deposits is supergene in origin (Arehart et al., 1992). Therefore dating of alteration minerals such as alunite provides only a minimum age unless evidence for a hypogene origin can be determined. Dating barite from the Lone Tree deposit is attempted using $^{40}Ar/^{39}Ar$ technique in order to constrain the lower boundary of the mineralization. The prominent occurrence of barite at the other Carlin-type deposits and the similar ionic radii of Ba^{++} (1.34 A°) and K^{+} (1.33 A°) provided the basis for this attempt. Among the most common divalent positive ions, barium has the largest ionic radius after radium (Barbieri, 1989). Isomorphic substitutability of certain ions is a phenomenon occurring in many minerals (Rosler and Lange, 1972). There are two important mechanisms for the elements replacing one another that have different charges but similar radii. One is the admission process in which an element having a lower charge replaces a main element having a higher charge. The reverse is the capturing process. Besides similar ionic radii, electronegativity has influence in the isomorphic incorporation of elements. In the case where elements with approximately the same eloctronegativity, the cation having the smaller ionic radius is preferably incorporated. Electronegativity of Ba^{++} and K^{+} is 0.85 and 0.80 respectively. The crystal chemistry character of Ba leads us to believe that it may be replaced by (or replace) large ions such as Pb^{++}, Sr^{++}, and K^{+}. If a sufficient amount of potassium replaces the barium, there would exist a possibility of directly dating ore formation at Carlin-type deposits.

REGIONAL GEOLOGY

The stratigraphy in the vicinity of Lone Tree mine contains three separate Paleozic rock sequences; Valmy Formation, Antler sequence, and Havallah Sequence. The oldest rock unit encountered in the area is the Middle Ordovician Valmy Formation that consists of quartzite, chert, minor basalt, and argillite. This rock sequence corresponds to the undivided part of Roberts Mountain allochthon (Theodore, 1991). Movement along the Roberts mountain thrust fault emplaced the western silicious and volcanic rocks on to the eastern carbonate rocks during the late Devonian to early Mississippian Antler orogeny (Roberts, 1964; Speed and Sleep, 1982). The highly deformed Valmy Formation rocks strike generally north with a west dip of 30-70° at the Lone Tree hill.

The autochthonous rocks of the Pennsylvanian Antler sequence unconformably overlie deformed Ordovician rocks, and are commonly referred to as an overlap assemblage (Roberts, 1964). These sedimentary rocks were deposited within the Antler orogenic belt during the initial marine submergence that followed the Antler orogeny (Verville and Sanderson, 1988). The Antler overlap sequence of Roberts (1964) includes three units, in an ascending order, the Battle Formation, the Antler Peak Limestone, and the Edna Mountain Formation. The Battle Formation, containing cobble conglomerates, overlies the erosional surface of the Valmy quartzite in the Lone Tree hill. The Edna Mountain Formation, which contains sandstone and siltstone, has been exposed in the walls of pit and also widely cut with drill cores in subsurface. No Antler Peak Limestone has been recognized in the area.

The allochthonous Pennsylvanian-Permian rocks of the Havallah sequence overlie the Antler sequence. The Havallah sequence is a structurally complex association of bedded chert, argillite, greenstone, sandy-limestone, sandstone, and conglomerate (Murchey, 1990). Roberts (1964) divided this complex into an older chert-argillite-greenstone sequence (Pumpernickel Formation) and a younger siliciclastic and calcareous turbiditic sequence (Havallah Formation). The complicated nature of this sequence is largely due to the obduction on the Golconda thrust fault and to a lesser extent depositional processes (Brueckner and Sneyder, 1985). The Golconda allocthon, consisting of the Havallah sequence, overrode the Roberts mountain allochton and younger overlap assemblage during the Late Permian and/or Triassic Sonoma orogeny (Silberling, 1975). The emplacement of Golconda allochthon has been explained in various ways. Speed (1979) and Miller et al. (1982) believe that the allochthon represents an exotic accretionary wedge complex. However, Murchey (1990) propose that Havallah sediments were deposited in a basin close to Antler orogenic belt and progressively stacked from west to east.

Volcanic rocks comprising rhyolitic, dacitic, basaltic lava flows, and silicic tuffs, and minor lake sediments represent the Tertiary rock units. Quaternary units including gravels and alluvium occur as a surface cover along the mountain fronts and in valleys (Roberts, 1964).

A series of plutonic events and block-faulting resulted in the development of basin and range structure in the north-central Nevada (Roberts et al., 1971). Silberman and McKee (1971) grouped major plutonism into five periods ranging in age from late Jurassic to late Tertiary. K-Ar ages for these plutons are: late Jurassic (168 to 143 Ma), Cretaceous (105 to 87 and 71 to 68 Ma), early Tertiary (40 to 30 Ma), and late Tertiary (16 to 10 Ma).

MINE GEOLOGY

The Lone Tree mine is located in an area that experienced a complex structural history and repeated episodes of igneous activity. The Golconda thrust is exposed at Golconda summit and extends in a southeast direction to the Lone Tree and Marigold mines (Bloomstein et al., 1993).

Significant extension due to the block-faulting took place in the early to middle Miocene in the Lone Tree area (Seedorff, 1991). Lone Tree Hill is a conspicuous north-trending horst formed as result of normal fault movement (Bloomstein et al., 1993).

Ore is hosted in Paleozoic rocks of the Valmy Formation, Edna Mountain Formation, and Havallah Formation (Fig. 2). The Valmy Formation at the Lone Tree mine is composed predominantly of quartzite (Ov) with minor argillite. Quartzite is massive and light-grey in color. In some places, grey, thinly laminated argillite is interbedded with quartzite. The Edna Mountain Formation is made of sucrosic siltstone, sandstone and lithic sandstone. Sucrosic siltstone and sandstone are characterized by a sugary appearance and a light-grey to light-brown color. This unit is intensely fractured and oxidized. The oxidation is evident from the red-colored areas due to the development of hematite and jarosite. Lithic sandstones are comprised of rounded light-grey quartzite, dark-brown chert, and small argillite clasts. This unit appears to be very compact, massive, and is intensely cut by vertical fractures in the mine area.

The Havallah Formation is a series of different rock units that defines the Golconda allochthon. One of the units is composed of argillite, siltstone, chert, and greenstone. The other unit includes calcareous siltstone and sandstone.

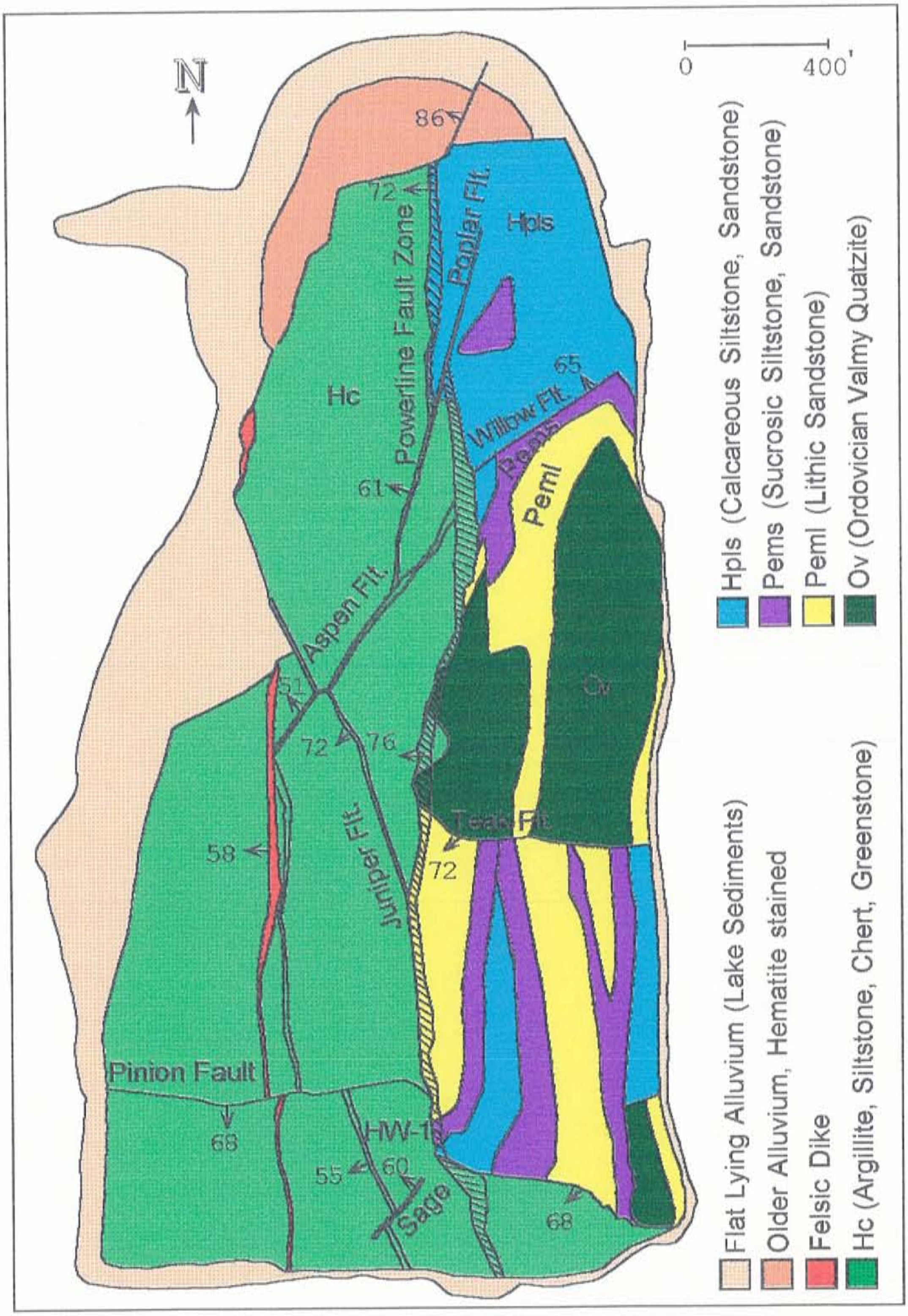

Figure 2. Geological map of the Lone Tree open pit mine

The former unit is dominated by dark green-colored chert. Small amounts of siltstone and argillite occur transitionally with chert. Greenstone has a porphyritic texture and forms lensoidal bodies in the chert. The latter unit is highly fractured and weathered at upper mine levels. Bedding planes are tilted and dip ~45° NW. Structure in the Havallah Formation is in general very complex. For instance, boudin-like features and small scale folds are common. These features formed during depositional processes and thrusting.

Felsic intrusive dikes are commonly rhyolites and dacites in the Lone Tree pit. Also, a granodiorite porphyry dike outcrops in the south end of the Lone Tree hill and it is also intersected by drilling in the west part of the pit. These dikes are altered and sparsely mineralized. K-Ar dating of biotite and hornblende indicates ages of 36 to 39 Ma (Bloomstein et al., 1993). Igneous rocks of similar ages also occur at the Edna mountain and Buffalo mountain west and southwest areas of Lone Tree respectively (Erickson et al., 1978).

Gold mineralization at the Lone Tree mine is primarily controlled by high-angle normal faults and fracture sets. The Powerline Fault Zone with a strike length of 2.5 km contains the bulk of gold ore (Fig. 2) and has a northerly strike with dips of 65° to 76° west. This fault zone has a vertical displacement of ~150m based on the offset of Paleozoic rock units. The northeast striking Poplar and

Willow faults as well as east striking Pinion fault crosscut the Powerline fault. Small scale faults like the HW-1 and the Sage contain high-grade gold. Dilational zones where the Juniper and Aspen faults meet the Powerline fault tend to host high-grade gold mineralization as well. Fracture sets are usually prominent at the footwall.

METHODS

The mineral paragenesis has been established through observations in the field, ore microscopy, neutron activation analyses (INAA), scanning electron microscopy (SEM), and X-ray diffraction analyses. Polished sections of 39 samples were examined under reflected light using a Nikon microscope equipped with Nikon objectives. Due to the very friable nature of the mineralized material, all of the samples were impregnated with epoxy under vacuum prior to cutting, grinding, and polishing. Impregnated samples were cut into smaller rectangular forms to ease polishing and sample handling. These samples were polished using successively finer abrasives including 220 grit, 600 grit, 1000 grit, and 10 micron silicon carbide (SiC). Polishing was finished with 0.05 micron gamma-aluminum oxide on microcloth.

Trace element analyses for selected samples were obtained from a commercial lab (Actlabs) by means of neutron activation (INAA), and inductively coupled plasma emission spectrometry (ICP). The ICP method was only used for analyses of silver, copper, lead, zinc, and thallium.

Fire assaying with atomic absorption finish was utilized to confirm gold grades in stage 3 mineralization. After reducing the size of pyrite crystals to 100 mesh-size or smaller, the sample was fire assayed to obtain a bead of gold. The bead is parted and then digested with aqua regia (1 unit HNO_3 acid + 3 unit HCl acid) and then mixed with five percent HCl acid. The gold concentration in solution was analyzed using the atomic absorption spectrophotometer housed in the chemistry laboratory of the New Mexico Bureau of Mines and Mineral Resources.

In order to determine arsenopyrite positively in the polished sections, dot mapping for arsenic was performed on five polished sections with Tracor Northern EDS (5400) model X-ray spectrometer, operated with Hitachi Hi-Scan (HHS-2R) model scanning electron microscope.

Clay minerals were identified from glycolated slides with a Rigaku D/Max I model X-ray deffractometer. The slides were prepared from the clay-size fraction of 4 hand samples. X-ray analyses were performed on these glycolated slides to differentiate smectite from the smectite-illite mixed layer by allowing smectite to swell.

Microthermometric measurements of fluid inclusions in quartz and barite were made using a Linkam Th 600 stage attached to a Leitz microscope with an 80 power Olympus objective. Quartz was first cut into 1 to 2 mm thick thin sections with a low-speed diamond saw. Doubly polished sections approximately 0.1 to 0.3 mm thick were prepared from these thin sections. After each polishing step, thin sections were ultrasonically cleaned to remove any rock fragments or abrasives in detergent added water. After polishing, sections were removed from slides using acetone. Barite crystals were simply cleaved along cleavage planes using a razor blade.

The accuracy of the fluid inclusion data was checked using standards with known melting and freezing points. Freezing calibrations were made using standards that contain artificial inclusions of pure H_2O and CO_2. Heating calibrations were made using substances with known melting points (e.g., K-dichromate). A calibration curve was then constructed to correct microthermometric data for samples from the Lone Tree mine. Homogenization temperatures and ice melting temperatures were cycled for three times. Reproducibility of homogenization temperatures was ±1.0 °C and ±2.0 °C for inclusions that homogenized below and above 300 °C, respectively. Repeated ice melting point temperatures were reproducible within ±0.1 °C.

Gas analyses of fluid inclusions in quartz, pyrite ± arsenopyrite ± marcasite, pyrite, and barite were performed on a quadrupole mass spectrometer. These minerals are representative of stages 1, 2, and 3 in the mineral paragenesis. Impurities on the surface of minerals were removed with 10% NaOH base, 10% HCl acid, and then cleaned in distilled-demineralized water. Then samples were dried in an oven at ~80 °C. Prepared samples were then loaded into three sample crushers connected to the quadrupole mass spectrometer, and baked overnight under vacuum to bring the pressure between $1\text{-}4 \times 10^{-7}$ mbar. Samples were mechanically crushed in a high vacuum extraction line, and released gases were directly analyzed with a quadrupole mass spectrometer, Balzers QMG 125 model. Each analysis is corrected for the background, which is taken as the average of the baseline values at the beginning of the peak and at the end of the peak tail. Among the measured peaks are 18, 17, 2, 28, 44, 15, 26, 40, 34, 4, 48 that correspond to H_2O, H_2O, H_2, N_2, CO_2, CH_4, C_nH_n, Ar, H_2S, He, and SO_2 respectively. An actual computer graphic display of the peaks for a typical crushing analysis is presented in figure 3. Calibration of the mass spectrometer was done by determining cracking outlines using commercial gas mixtures. The only problem encountered during the analyses was the poor detection of the He peak. This was partly due to the small amount of He and partly from the interfering tail on the H_2 peak.

Analytical techniques for the $^{40}Ar/^{39}Ar$ dating

Barite samples were obtained from different types of mineral deposits including Carlin-type gold, Mississippi

Valley Type (MVT) lead-zinc, synsedimentary bedded barite, Kuroko-type volcanogenic, and a replacement deposit. These deposits according to their type and geographic location are listed in Table 1.

Barite crystals were removed from hand samples and crushed to smaller sizes. The 14-20 mesh fraction was ultrasonically cleaned in dilute hydrochloric acid and rinsed in distilled water, and then dried in an oven at about 100 °C. The least altered crystal fragments free of metallic minerals were hand-picked under the binocular microscope. Barite crystals from the Lone Tree deposit that were used in the initial dating trial may have had some discoloration. Barite samples weighing 150-160 mg were placed in six hole irradiation trays with alternating flux monitors of Fish Canyon Tuff sanidine (27.84 Ma) (Samson and Alexander, 1987). The sample-filled trays were then irradiated for ten hours in the L67 position of the Ford Nuclear Reactor at the University of Michigan. Analyses were carried out at the New Mexico Geochronology Research Laboratory at New Mexico Tech in Socorro, New Mexico. This facility consists of an MAP 215-50 mass spectrometer connected to a computer-automated all-metal argon extraction line (McIntosh and Cather, 1994).

J-factors were determined to ~±0.5% from the pooled results of CO_2 laser fusion of three to four single crystals of each flux monitor. The irradiation parameter (J-factor) appropriate to the unknown barite samples were determined by interpolation of the flux monitor data. The chemically reactive gases were gettered from argon using a GP-50 getter operated at 2.2 A.

Barite samples weighing 4 to 6 mg were step heated with a CO_2 laser. Evolved gases were gettered for 5 minutes using the GP-50 getter. Due to the expected low K and radiogenic argon ($^{40}Ar^*$), relatively large (100-120 mg) samples were step heated in a resistance furnace. Copper wrapped barite crystals were dropped into a molybdenum crucible and incrementally heated in steps from 500 °C to 1700 °C. The gettering time varied for samples from 7 to 30 minutes.

Full system blanks are run before each sample analyses. The average ^{40}Ar blank for the laser system was $3x10^{-16}$ moles. The extraction line blank for furnace analyses ranged from $2x10^{-15}$ to $3x10^{-16}$ moles ^{40}Ar. System blank corrections are always included in age calculations. The ages in individual steps of age spectra have analytical uncertainties of two sigma (2σ) and the ages given in data tables are quoted at one sigma (1σ) error.

The barite separates were crushed into a fine powder and analyzed for their potassium content with atomic absorption flame photometry (AA) at the chemistry laboratory of New Mexico Bureau of Mines and Mineral Resources. In this analysis, barite powders were fused with Li_2O to increase their solubility, and then put into solution with HCl acid and finished with AA.

Table 1. Barite samples listed according to their deposit type and geographic location.

Deposit	Type	Location	Age const.
Lone Tree	Carlin-type	Nevada	Tertiary?
Getchell	Carlin-type	Nevada	Late Ter.?
Betze-Post	Carlin-type	Nevada	Creta.?
Rain	Carlin-type	Nevada	Unknown
Lakes	Synsed. bed. bar.	Nevada	Ordovic.
Buchans	Kuroko-type vol.	Newfoundland	Ordovic.
Hansonburg	MVT lead-zinc	New Mexico	Tertiary?
Bredehorn	Replacement	Greenland	Tertiary?

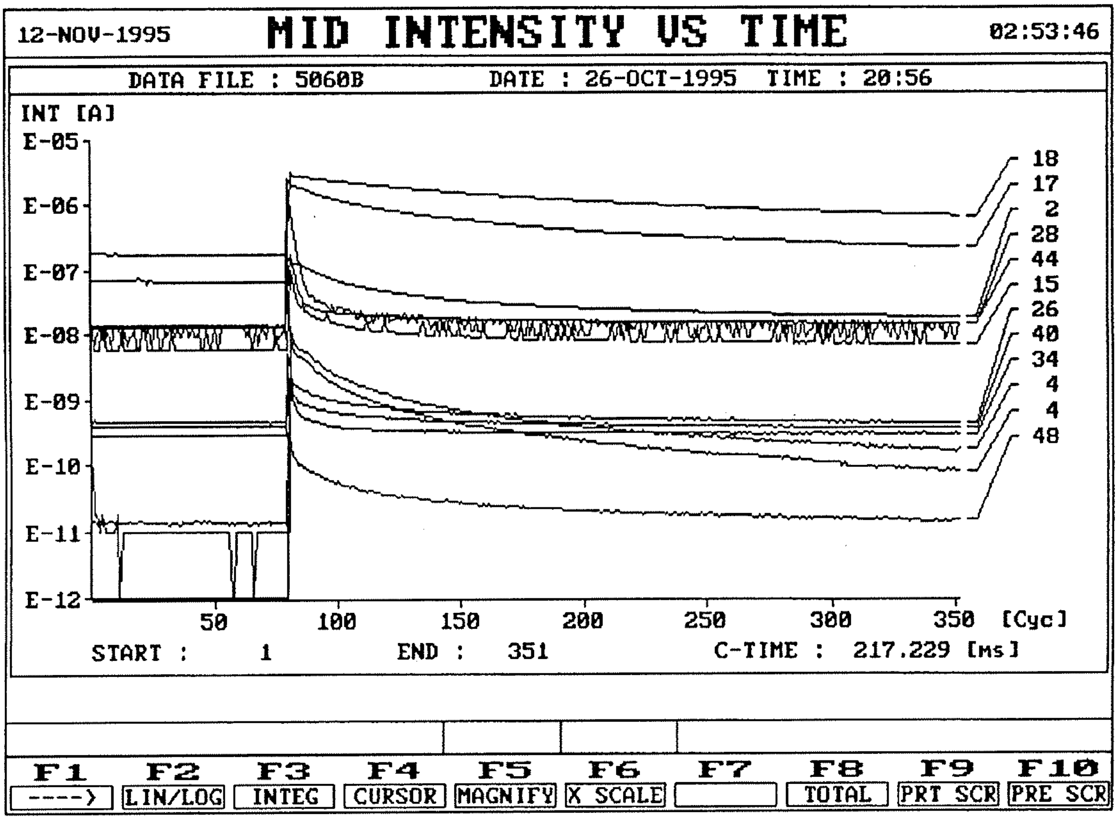

Figure 3. Computer graphic display of the peaks for a typical crushing analysis of fluid inclusion gases with quadrupole mass spectrometry. These peaks represent the gases released from quartz #12 for second time crushing. The y-axis is intensity on logarithmic scale and the x-axis is time for 350 measurement cycles.

RESULTS

HOST ROCK ALTERATION

Alteration of the host rocks at the Lone Tree deposit comprises decarbonatization, silicification, and argillization. Fluids that produced alteration, and mineralization were dominantly restricted to fault zones and fractures. The distribution of alteration to a small extent was also influenced by the lithology of the host rocks. This is evident where alteration is much more intense in calcareous sandstones within fault zones and decreases in footwall and hanging-wall rocks of different lithologies.

Decarbonatization was the first alteration type to develop and has affected the host rocks to varying degrees depending on lithology and location relative to structures. Decarbonatization reactions result in the dissolution of calcite from host rocks through interaction with acidic fluids. This process increases the porosity and permeability of the host rocks, which in turn creates suitable pathways for ore fluids. Unaltered rocks from drill cores contain as much as 50% calcite (i.e., MLT201-800) whereas altered rocks usually contain less than 1% calcite (see Table 3). Dissolution of calcite results in a significant decrease in a rock's density, strength, and volume (Kuehn and Rose 1992). The very friable nature of the ore as well as collapse breccias are the result of decarbonatization prior to mineralization.

Silicification following decarbonatization is represented by multiple generations of quartz veins that occur in fault zones, fractures, and permeable areas. The first generation of silicification is identified by angular quartz fragments and intensely silicified host-rock fragments as breccia clasts. The quartz fragments are milky in color and contain small amounts of pyrite. The second generation of silicification is represented by quartz veins, which range in thickness from 2 cm to 2 mm, that can be traced across fault zones. These veins are also mineralized and clear to white in color. No jasperoid was recognized at the Lone Tree deposit.

Argillic alteration is widespread in fault zones and occurs around broken pieces of quartz. The clay mineral assemblage includes kaolinite, illite, smectite, illite-smectite mixed layer (Table 2). Other clay-sized minerals in fault zones include alunite and quartz (Table 2). No chlorite has been identified in the clay-size fraction of ore material, however chlorite occurs as a pre-ore alteration phase of basalts in the Havallah Formation.

Supergene versus hypogene origin for kaolinite can be distinguished by X-ray diffraction analysis. The X-ray diffraction analysis of sample# 13 (lab# GA95048) gives a high intensity, distinct, and well-defined peak for kaolinite (Fig. 4). These types of peaks represent well-crystallized, coarse kaolinite formed from hypogene hydrothermal alteration rather than simple weathering processes (G. S. Austin, per. comm., 1995). The amount of kaolinite tends to be highest in center of the Powerline fault zone (Table 2).

Table 2. Quantitative mineralogy of clay-size fraction representative of argillic alteration.

Sample#	Kao	Ill	Chl	Sme	I/S	Others
13	5	3	-	-	2	Qtz, Alu
37	8	2	-	Tr	Tr	Qtz, Alu
50	1	5	-	-	4	(Qtz)
LA-1	Tr	4	-	2	4	Qtz

Note: Kao = kaolinite, Ill = illite, Chl = chlorite Sme = smectite, I/S = illite-smectite mixed layer, Qtz = quartz, (Qtz) = quartz (minor component) and Alu = alunite (major component). Clay minerals are given as parts in ten. Tr = trace or less than 0.5 parts in ten. Sample# 13 and sample# 37 are collected from the central part of Powerline fault zone.

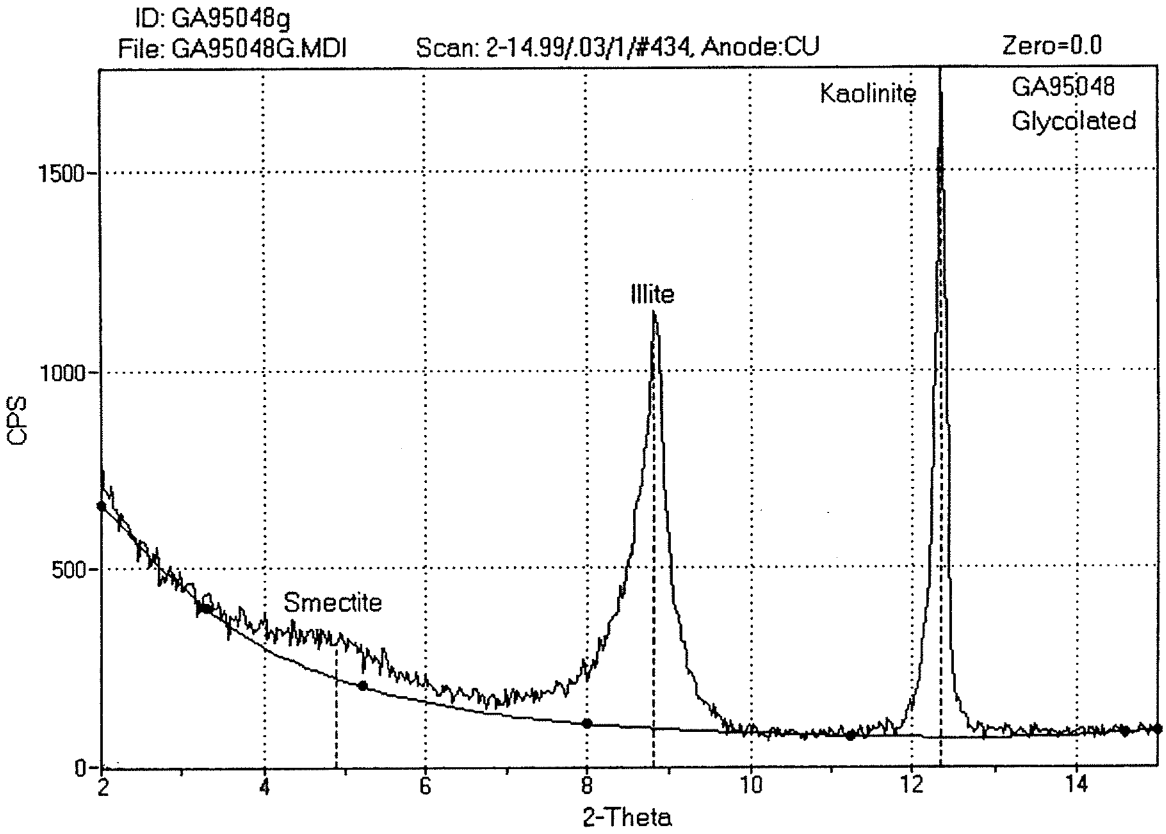

Figure 4. X-ray diffraction analysis of glycolated slide from sample# 13 (lab# GA95048) has yielded a sharp peak for the kaolinite indicating hypogene hydrothermal alteration.

MINERALIZATION AND MINERAL PARAGENESIS

Mineralization at the Lone Tree deposit occurs within fault zones and fracture sets. Fault zones are comprised of hydrothermal breccia clasts set in an argillically altered clay matrix. Breccia clasts comprise angular quartz fragments and intensely silicified host rocks. These clasts are locally cemented together by sulfide minerals that are primarily pyrite with lesser marcasite and arsenopyrite. Clusters of coarse pyrite cubes as well as fine-grained subhedral pyrite occur as disseminations in a clay matrix. Other sulfide minerals associated with disseminated pyrite are marcasite, arsenopyrite, sphalerite, and chalcopyrite. The above sulfide mineral suite is also present in the form of micro veins in a clay matrix. Gold mineralization in fracture sets within the footwall of the Powerline Fault is contained in a barite-pyrite matrix of breccias, and as open-space fillings veins. These veins containing barite, pyrite, and gold can also extend into the Powerline Fault zone and overprint the main gold sulfide mineralization.

Four stages of mineralization have been identified at the Lone Tree deposit (Fig. 5). Stage 1 contains brecciated quartz and small amounts of subhedral to anhedral pyrite (Fig. 6). Stage 2 is the main gold event and consists of quartz, kaolinite, pyrite, marcasite, arsenopyrite, gold, sphalerite, and chalcopyrite (Fig. 5).

Mineral Paragenesis at The Lone Tree Gold Deposit

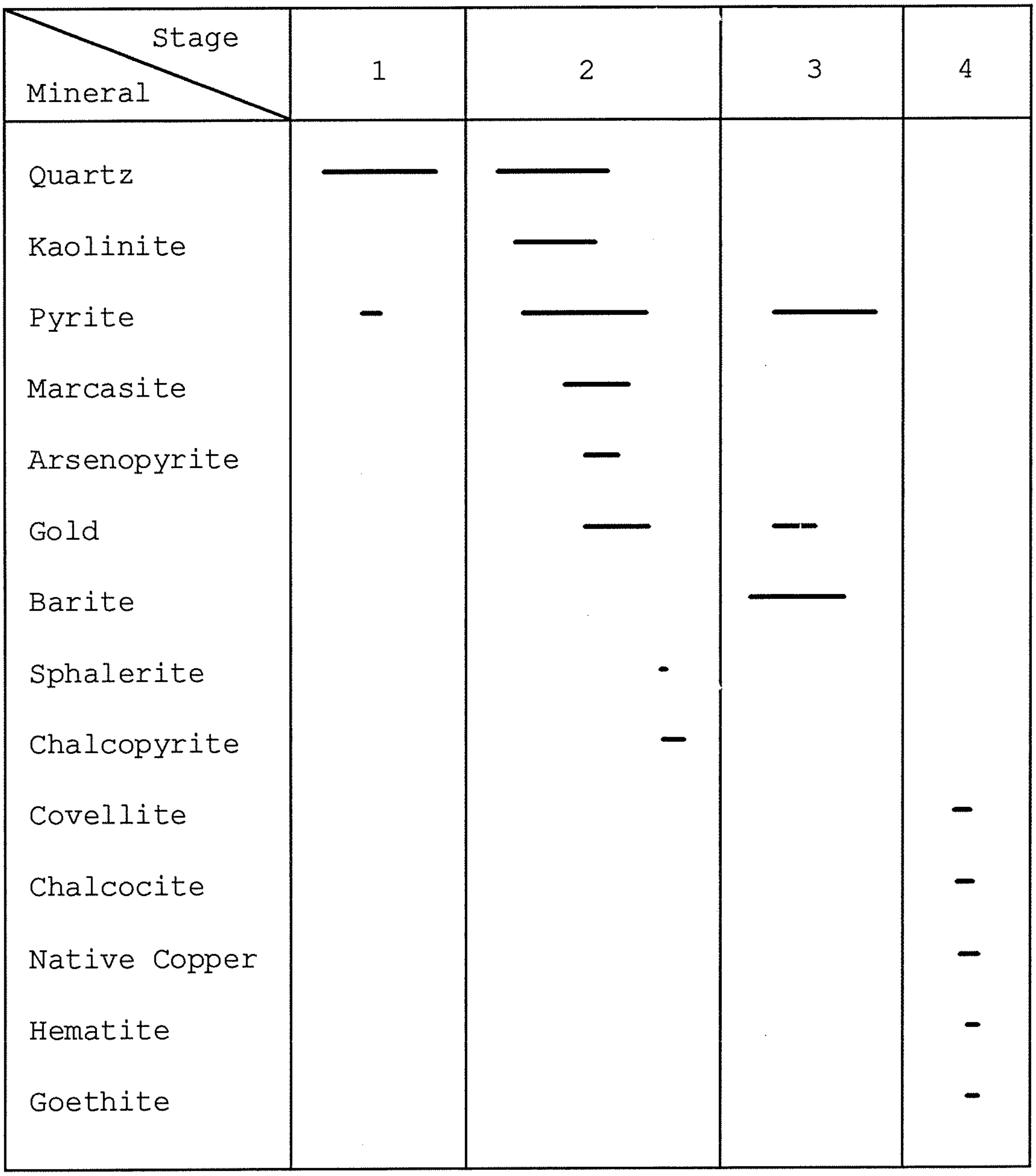

Figure 5. Four stages of mineral precipitation and relative abundance of each mineral at the Lone Tree gold deposit.

Stage 2 quartz is commonly fractured and occurs as veins within and at the margins of the Powerline fault zone. Although broken and slightly displacement, quartz veins can be traced across the Powerline fault zone. These quartz veins contain auriferous pyrite and some free gold. Gold mineralization within the Powerline fault zone is also associated with pyrite in argillized material. Three free gold grains in stage 2 mineralization were observed. One of the gold grains, which is anhedral and 200 micron in size, is contained in quartz (Fig. 7). The other two free gold grains have an elliptical form and are 10 micron in size. The latter grains are spatially associated with a pyrite cube and are located in clay mineral assemblage (Fig. 8).

Pyrite at the Lone Tree mine displays distinct morphologies. Stage 2 pyrite in hand samples and polished sections occurs in the form of disseminations, micro veins, and as the cement in breccias. Clusters of pyrite cubes as much as 0.5 cm in size are disseminated in clay-sized material. Coarse pyrite cubes contain lesser amounts of gold relative to finer-grained subhedral to anhedral pyrite (Table 3). In some cases, coarse pyrite cubes coexist with fine-grained pyrite. Euhedral to subhedral pyrite grains constitute micro veins in brittlely fractured rocks. The different forms of pyrite seem to reflect the way that different rock lithologies responded to deformation and alteration processes (i.e., fracturing, brecciation,

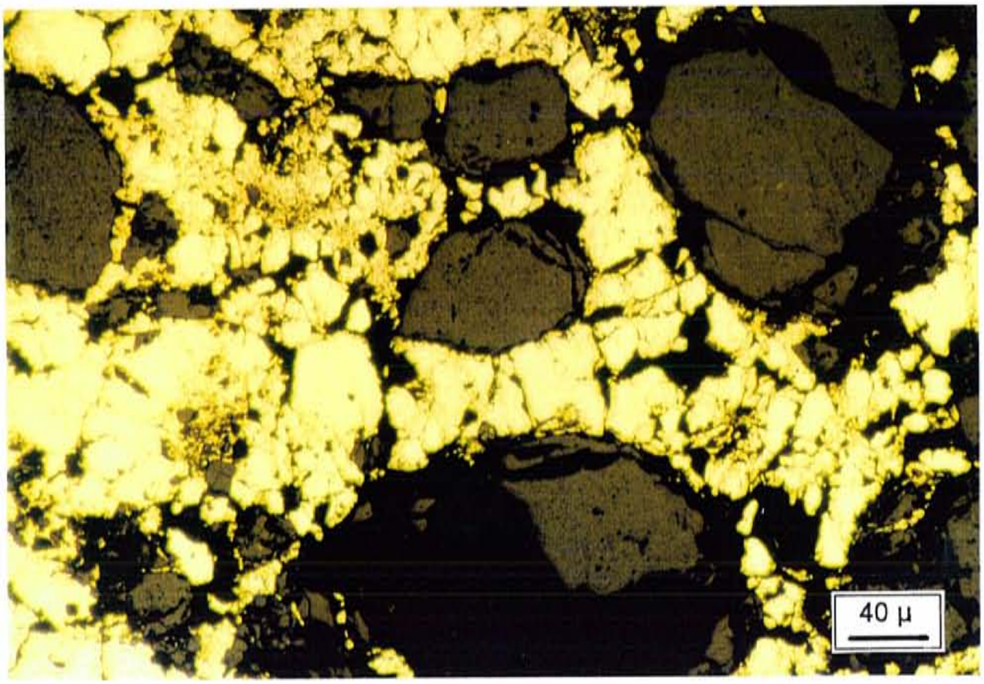

Figure 6. Photomicrograph of brecciated quartz in stage 1 mineralization.

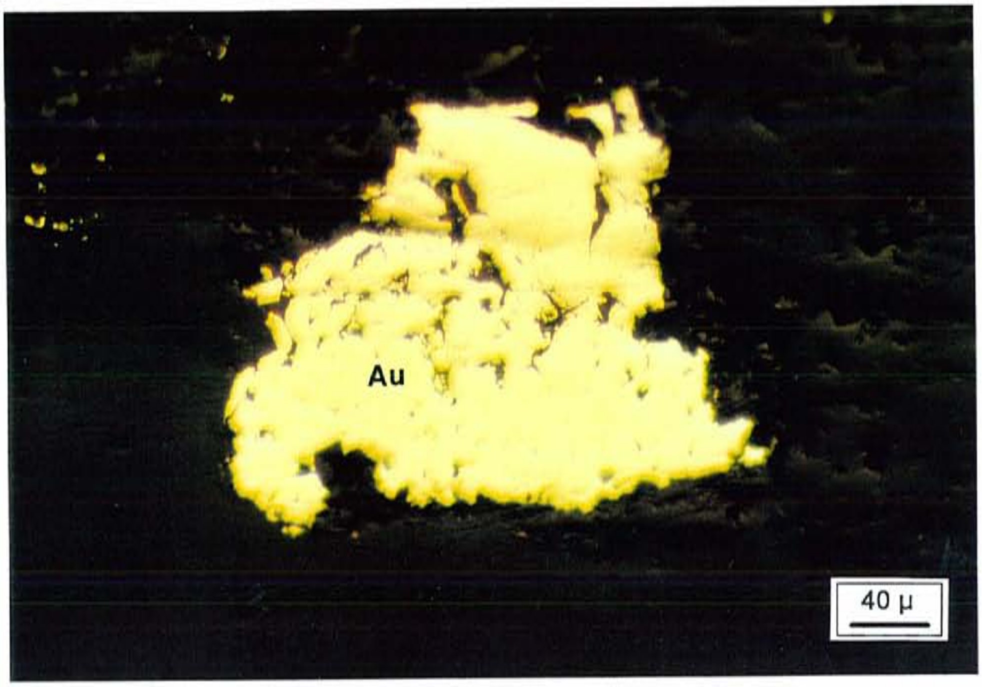

Figure 7. Photomicrograph of an anhedral free gold grain, 200 micron in size and is contained in quartz.

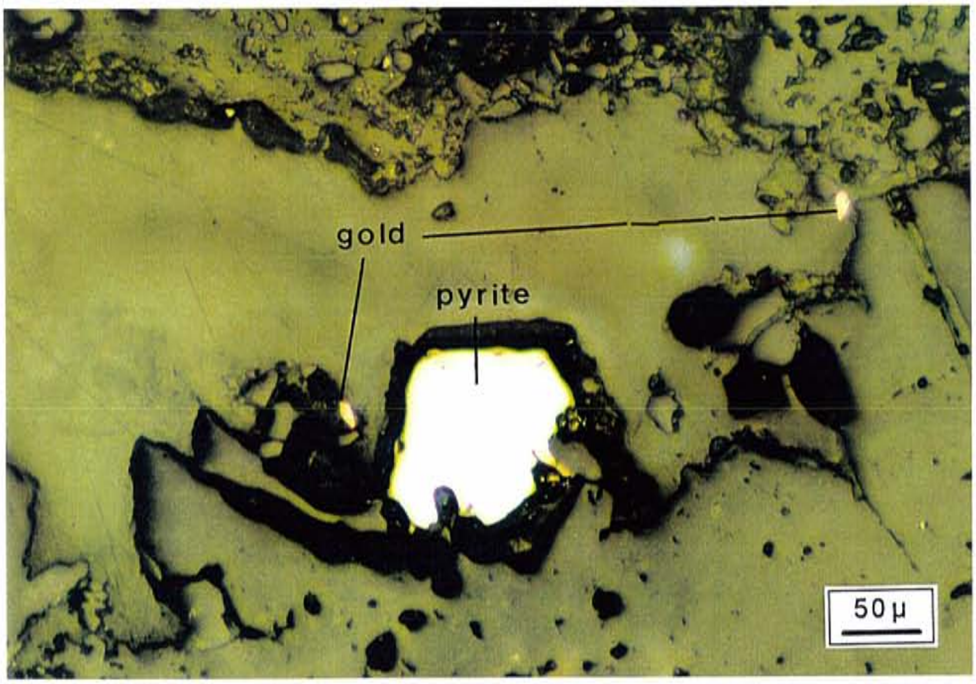

Figure 8. Photomicrograph of two 10 micron free gold grains located in clay assemblage and associated spatially with a pyrite cube.

decarbonization, argillization, silica replacement...).

Marcasite is the second most abundant sulfide mineral, after pyrite, in stage 2. Marcasite shows distinctive lamellar twinning, arrow head texture, and blade like textures (Fig. 9) and usually occurs with pyrite in veins. Marcasite grains mantle, and sometimes are intergrown with, euhedral and cubic pyrite (Fig. 10). Marcasite can also be rimmed and replaced by arsenopyrite (Fig. 11), based on SEM imagery and element mapping of As.

Sphalerite and chalcopyrite are present in both drill core and pit samples in small amounts. Chalcopyrite is more abundant than sphalerite. Both minerals are anhedral and accompany each other. Chalcopyrite occurs not only as small specks in sphalerite, but also rimming sphalerite (Fig. 12). Sphalerite and chalcopyrite surround pyrite and/or marcasite crystals (Fig. 12). Chalcopyrite is paragenetically the latest mineral to precipitate in stage 2.

Stage 3 is the late stage gold event and comprises barite, pyrite, and gold. Barite crystals are prominent in open-space fractures and as the cement to breccias in the footwall of the powerline fault. Additionally, barite veins in the footwall are commonly coated by botryoidal pyrite that exhibits growth banding (Fig. 13). In contrast, within the powerline fault zone barite crystals, ~0.5 mm to 1 cm in size, were deposited on other sulfide minerals. Pyrite in stage 3 shows growth banding texture in polished sections, that can indicate changing fluid conditions or multiple hydrothermal events which formed pyrite. The width of the growth bands in pyrite range from 10 to 250 microns (Fig. 13).

Stage 4 is supergene mineralization and includes covellite, chalcocite, native copper, hematite, and goethite. Covellite and chalcocite replace pyrite cubes along the surfaces and give pyrite a rounded shape (Fig. 14). Due to the replacement processes, some of the pyrite cubes have broken into smaller anhedral grains (Fig. 14). Native copper was observed in hand samples as well as in polished sections. It has a dendritic texture in hand samples, but an anhedral form in polished sections. Native copper is associated with goethite and hematite where it is surrounded by these iron hydroxide/oxide minerals (Fig. 15). Red stains resulting from the oxidation of pyrite is readily observable on the walls of the pit.

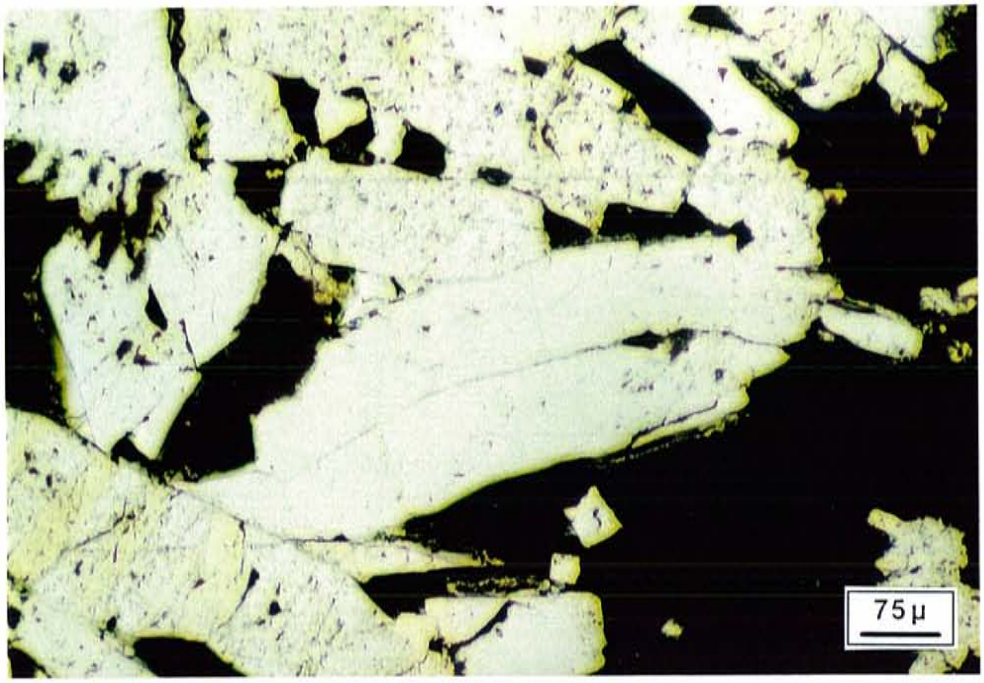

Figure 9. Photomicrograph of marcasite exhibiting typical arrow head and blade like texture.

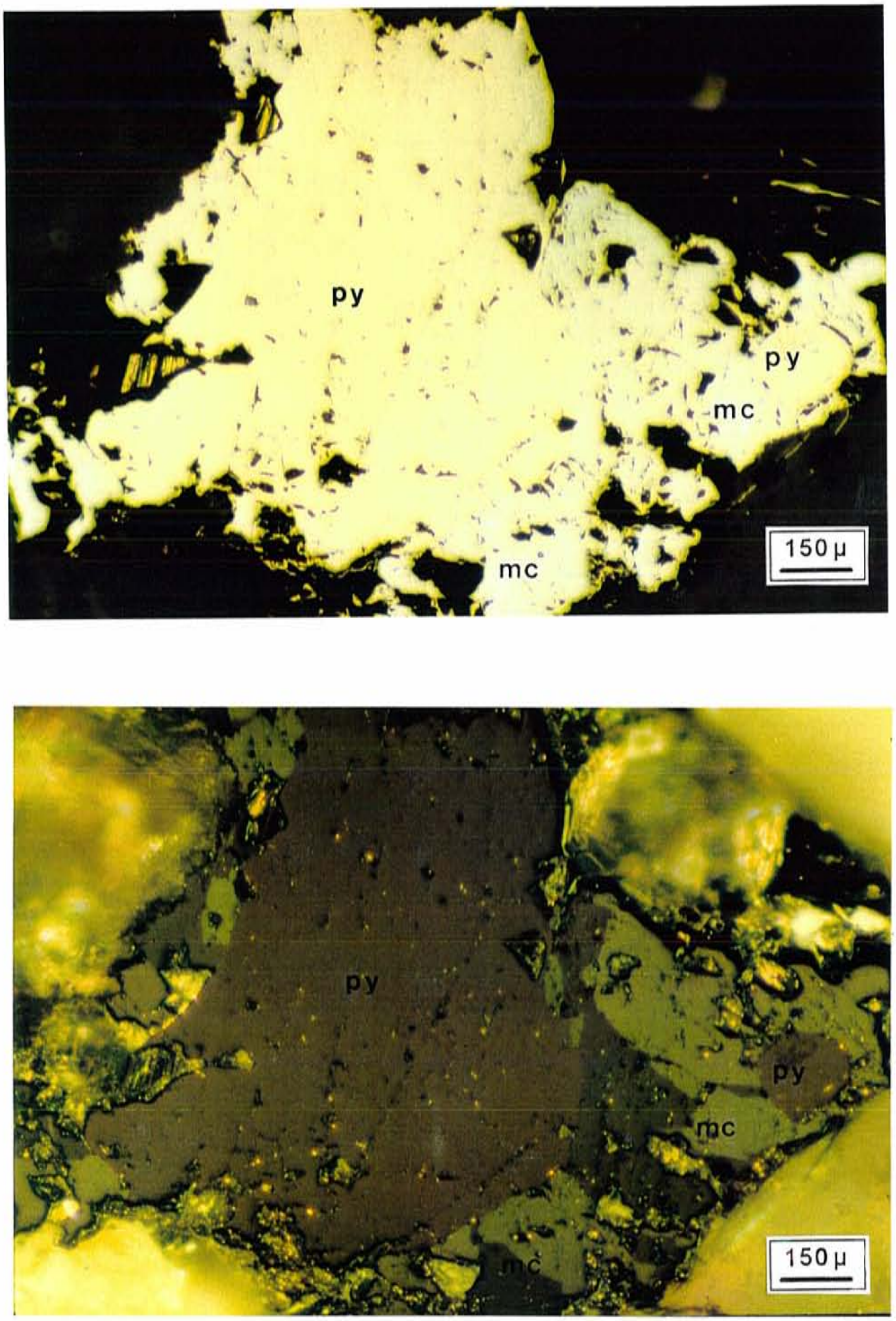

Figure 10. Photomicrograph of marcasite (mc) mantling euhedral pyrites (py). A: uncrossed nicols, B: partly crossed nicols; dark green anisotropic marcasite clearly surrounds the brown isotropic pyrite.

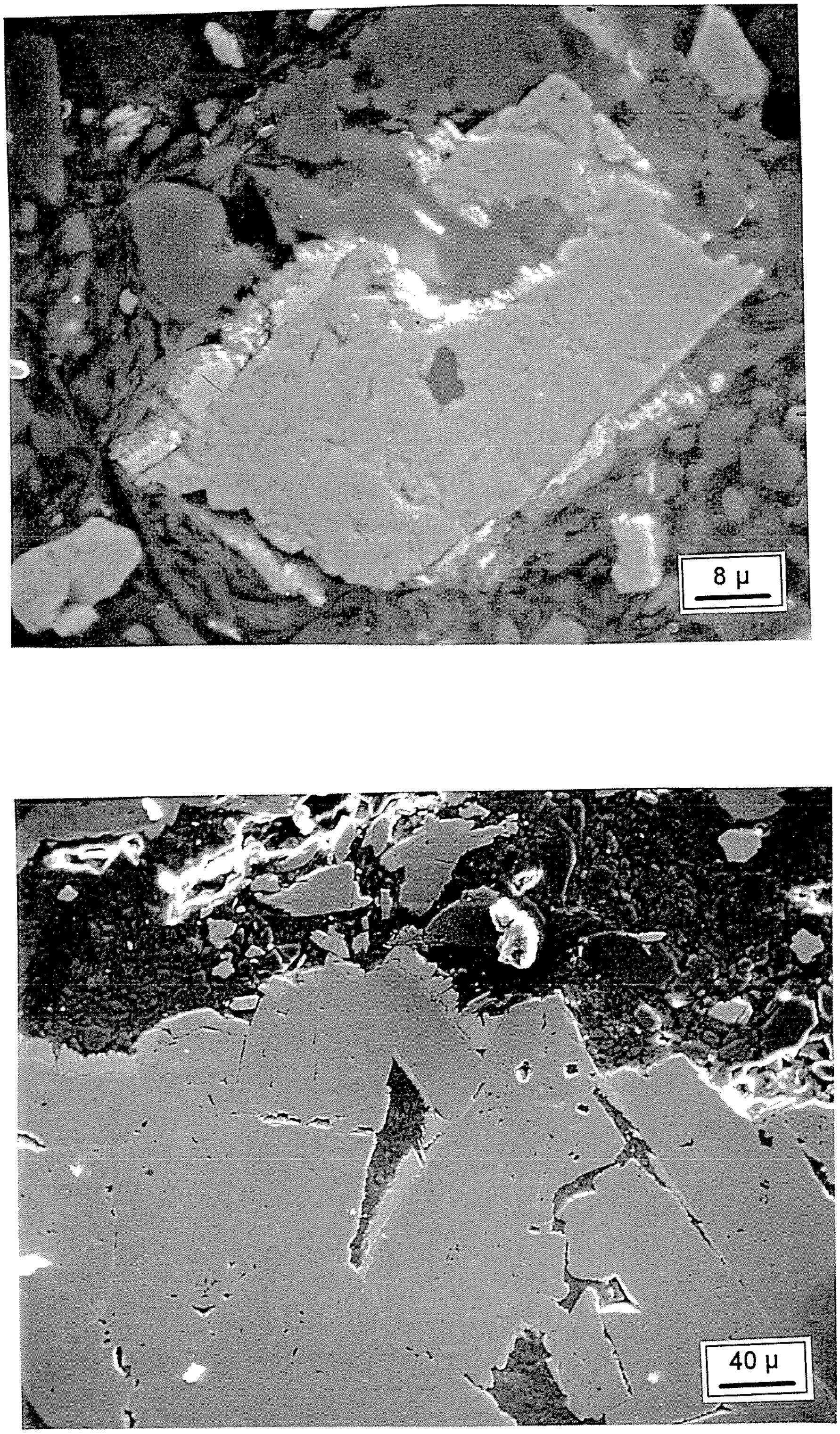

Figure 11. SEM imagery of arsenopyrite crystals rimming and/or replacing marcasite.

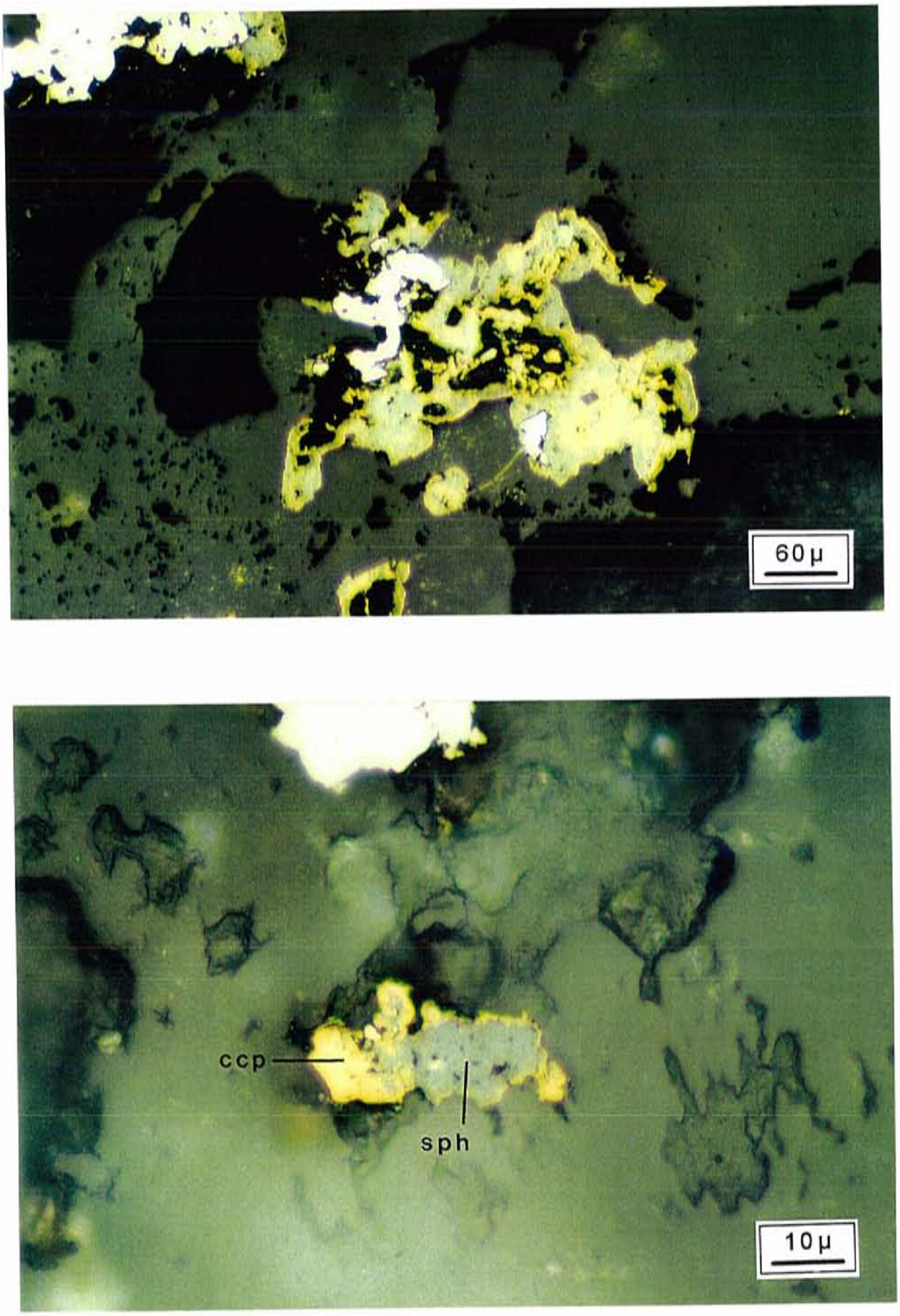

Figure 12. A: Photomicrograph of chalcopyrite (ccp) and sphalerite (sph) surrounding pyrite and/or marcasite, B: Chalcopyrite rimming sphalerite and also pyrite and/or marcasite.

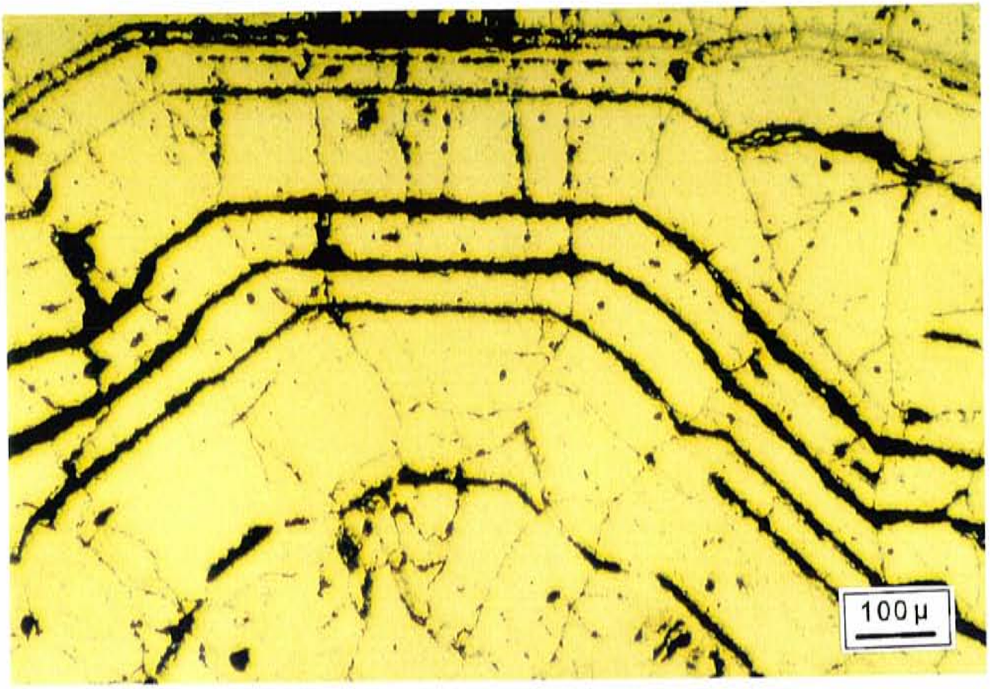

Figure 13. Photomicrograph of growth banding pyrite in stage 3 mineralization. The width of the growth band ranges from 10 to 250 microns.

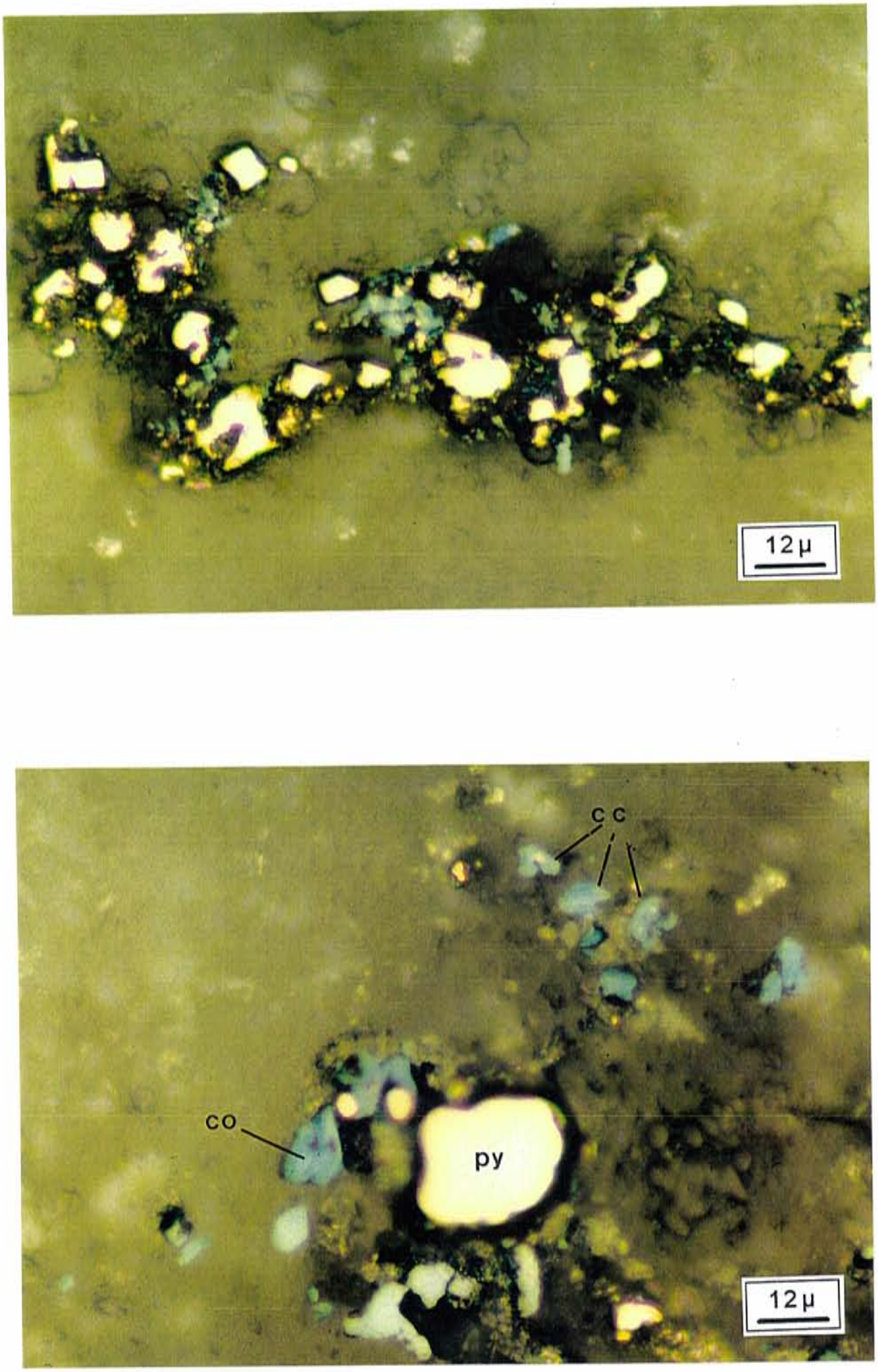

Figure 14. Photomicrographs of covellite (co) and chalcocite (cc) replacing pyrite.

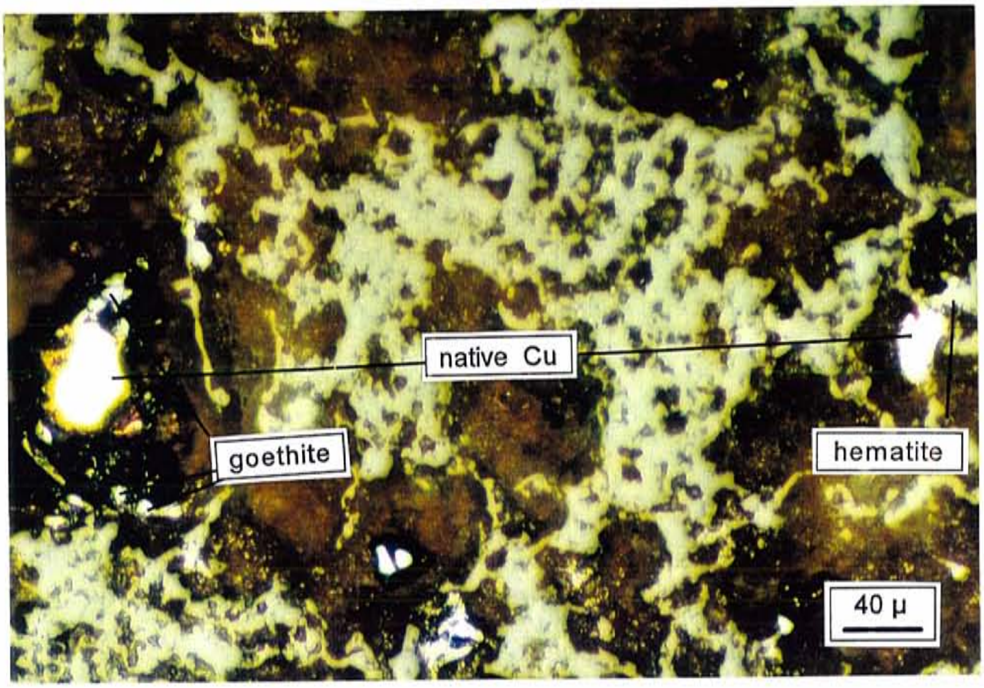

Figure 15. Photomicrograph of native copper associated with goethite and hematite.

Chemical analyses of sulfide minerals from stage 2 and stage 3 mineralization indicate that both stages contain economic gold mineralization (Table 3). Au/Ag ratios and the concentrations of Au, Ba, Cu, Pb, Zn, As, Sb, and Hg as ppm in stage 2 and stage 3 minerals are plotted in Figure 16. There is not a significant variation in Au/Ag ratio between stage 2 and stage 3 mineralization, although the ratio is slightly higher in stage 3 mineralization. Gold concentrations in stage 2 mineralization have a greater range and higher average value relative to stage 3 mineralization. Among base metals, Cu concentrations in both stages of mineralization are high especially in stage 2 mineralization. Ba, As, Sb, and Hg concentrations are anomalously high and their values are higher in stage 3 mineralization.

The gold in stage 3 mineralization was confirmed by fire assaying with atomic absorption (AA) finish (Table 6). Stage 3 pyrite separates (L3, 31, and L2) were ultrasonically cleaned and examined under a binocular microscope to ensure purity of the separate. Gold grades for these separates are 3.73, 5.25, and 3.6 ppm (Table 6).

Table 3. Chemical analyses of selected samples for gold and other elements by neutron activation (INAA) and inductively coupled plasma emission spectrometry (ICP)

Sample #	L2	L3	31	24	30	50	LA	28*	27	28pc	28pf
Au (ppm)	1.82	2.62	11.1	4.28	19.9	2.49	.315	.35	34.7	.17	1.44
Ag (ppm)	*2.5*	*.2*	*5.7*	*.7*	*4.2*	*.8*	*.4*	*1.5*	*29.1*	*-.2*	*6.7*
As (ppm)	3600	9600	2700	1400	2600	1100	2200	120	300	32	250
Ba (ppm)	<100	53000	20000	490	1100	300	1300	390	470	<100	<200
Br (ppm)	<1	<2	<1	<1	<1	<1	<1	<1	<1	<1	<2
Ca (%)	<2	<2	1	<1	<1	<1	4	<1	<2	<1	<8
Co (ppm)	<5	75	<5	<5	<5	11	<5	16	28	28	91
Cr (ppm)	300	140	250	200	210	180	390	120	140	18	<10
Cs (ppm)	<2	3	4	4	<2	9	7	<2	2	<2	<2
Cu (ppm)	*615*	*336*	*110*	*40*	*61*	*58*	*56*	*3020*	*1830*	*197*	*4430*
Fe (%)	18	22.8	10.8	3.04	12.6	10.6	5.63	13.5	13.1	41.9	57.8
Hf (ppm)	3	9	3	7	4	6	6	3	4	<1	6
Hg (ppm)	42	10	<1	<1	<1	6	<1	5	16	2	12
Ir (ppb)	<5	<5	<5	<5	<5	<5	<5	<5	<5	<5	<5
Mo (ppm)	<5	17	<5	10	<5	<5	<5	<5	<5	<5	<5
Na (%)	.06	<.05	.35	.3	.44	<.05	<.05	.09	<.05	<.05	.07
Ni (ppm)	<55	340	<52	<50	<50	<50	<50	<50	<50	<64	<490

Table 3. continued

Sample #	L2	L3	31	24	30	50	LA	28*	27	28pc	28pf
Pb (ppm)	*12*	*8*	*9*	*3*	*15*	*24*	*8*	*8*	*17*	*16*	*17*
Rb (ppm)	<30	<30	46	<30	<30	55	60	<30	<30	<30	<56
Sb (ppm)	470	1200	400	61	360	61	46	19	220	6.3	18
Sc (ppm)	3.6	.4	3.8	11	3.5	4.4	14	7.5	6.7	1.1	4.3
Se (ppm)	120	130	<5	<5	<5	<5	<5	77	40	160	540
Sn (%)	.08	.09	<.08	<.01	<.07	<.02	<.04	<.01	<.03	<.01	<.09
Sr (%)	.05	.05	<.05	<.05	<.05	<.05	<.05	<.05	<.05	<.05	<.05
Ta (ppm)	<1	<1	<1	<1	2	<1	<1	<1	<1	<1	<2
Th (ppm)	3.7	<.8	5.4	12	4.5	11	23	7.7	5.5	1.5	5.2
Tl (ppm)	*-10*	*-10*	*-10*	*-10*	*-10*	*-10*	*-10*	*-10*	*-10*	*-10*	*-50*
U (ppm)	<1.4	6.1	<1.4	2.4	<1.2	2.5	7.3	1.7	<.9	<.5	<1.4
W (ppm)	130	<4	24	23	17	6	60	32	38	7	43
Zn (ppm)	*29*	*778*	*25*	*2*	*23*	*93*	*23*	*12*	*32*	*7*	*17*
La (ppm)	29	6	21	35	20	25	190	30	19	4	10
Ce (ppm)	41	<10	29	78	38	51	330	64	37	5	24
Nd (ppm)	20	<20	15	30	15	19	88	21	15	<5	<12
Sm (ppm)	2.8	.3	2.7	5.7	2	3.2	7.9	3.9	2	.6	2
Eu (ppm)	1	<.2	<.2	1	<.2	.9	2.2	1.1	.7	.7	<.3

Table 3. continued

Sample #	L2	L3	31	24	30	50	LA	28*	27	28pc	28pf
Tb (ppm)	<.5	<.5	<.5	<.5	<.5	<.5	<.5	<.5	<.5	<.5	<.7
Yb (ppm)	1.7	<.5	<.3	2.1	<.2	1.5	2.3	.7	1.4	<.2	<.3
Lu (ppm)	.21	<.09	<.06	.36	<.06	.23	.4	.14	.2	<.05	<.07

Note: Samples #L2, L3, and 31 are from the third stage of mineralization along the fracture sets and veins at the footwall of powerline fault zone. 28* is whole sample containing coarse pyrite cubes. The other samples are from the second stage of mineralization along the powerline fault zone. 28pc is coarse pyrite cubes and 28pf is fine grained pyrite. ICP analyses are shown with italics. The errors related to the INAA and ICP analyses for each element are dependent on the detection limits. The error at the detection limit is 100%, 10 times the detection limit is 10-15%, and 100 times the detection limit is <5%. Detection limits of elements for INAA and ICP are provided in tables 4 and 5 respectively. Negative values indicates less than the detection limit. Higher detection limit for Tl in sample 28pf is due to small sample size.

Table 4. Detection limits for INAA

Element	Det. limit	Element	Det. limit	Element	Det. limit	Element	Det. limit
Au	5 (ppb)	Hf	1 (ppm)	Se	5 (ppm)	Nd	5 (ppm)
As	2 (ppm)	Hg	1 (ppm)	Sn	.01 (%)	Sm	.1 (ppm)
Ba	100 (ppm)	Ir	5 (ppb)	Sr	.05 (%)	Eu	.2 (ppm)
Br	1 (ppm)	Mo	5 (ppm)	Ta	1 (ppm)	Tb	.5 (ppm)
Ca	1 (%)	Na	500 (ppm)	Th	.5 (ppm)	Yb	.05 (ppm)
Co	5 (ppm)	Ni	50 (ppm)	U	.5 (ppm)	Lu	.05 (ppm)
Cr	10 (ppm)	Rb	30 (ppm)	W	4 (ppm)		
Cs	2 (ppm)	Sb	.2 (ppm)	La	1 (ppm)		
Fe	.02 (%)	Sc	.1 (ppm)	Ce	3 (ppm)		

Table 5. Detection limits for ICP

Element	Detection limit	Element	Detection limit
Ag	.2 (ppm)	Zn	1 (ppm)
Cu	1 (ppm)	Tl	.1 (ppm)
Pb	2 (ppm)		

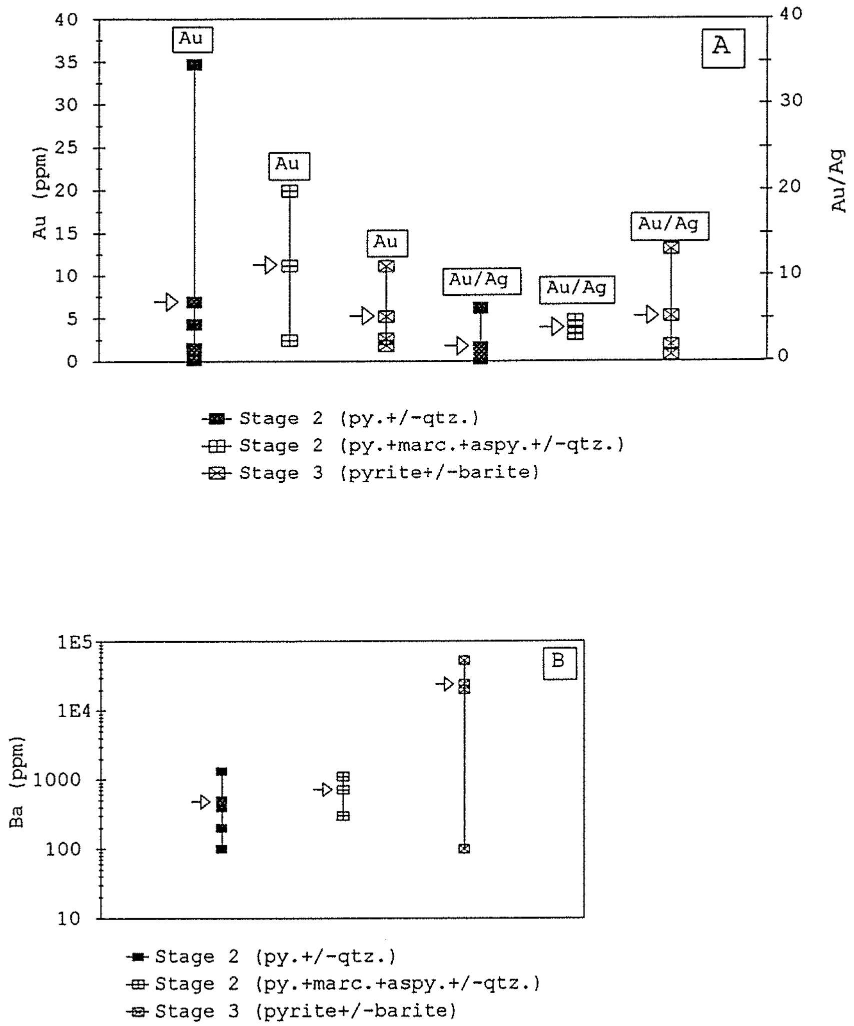

Figure 16. Au/Ag ratios and the concentrations of elements (Au, Ba, Cu, Pb, Zn, As, Sb, and Hg) in stage 2 and stage 3 mineralization. Arrows show average Au/Ag ratio and concentrations.

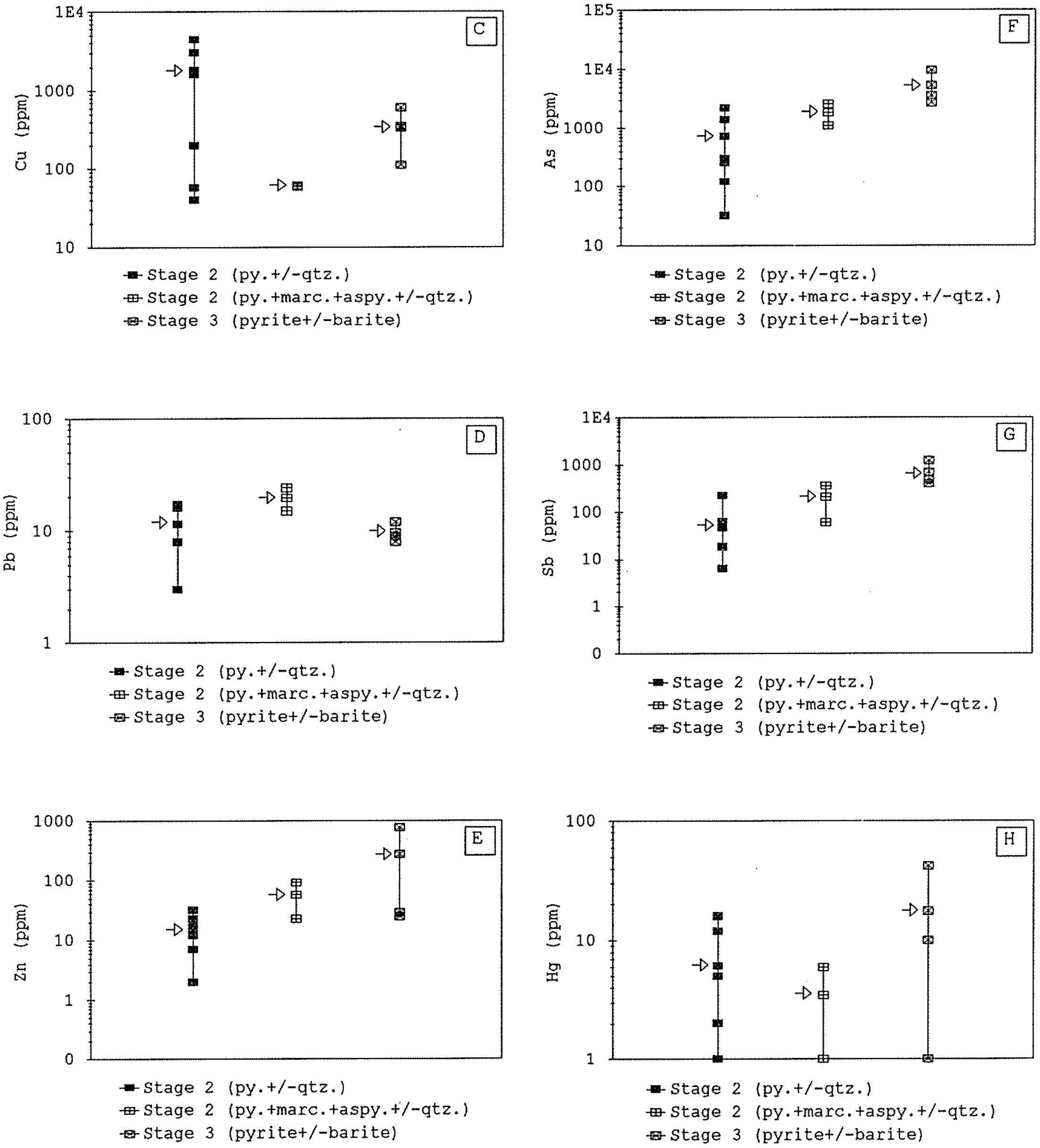
C
Cu (ppm)
1E4
1000
100
10
F
As (ppm)
1E5
1E4
1000
100
10
D
Pb (ppm)
100
10
1
G
Sb (ppm)
1E4
1000
100
10
1
0
E
Zn (ppm)
1000
100
10
1
0
H
Hg (ppm)
100
10
1
Stage 2 (py.+/-qtz.)
Stage 2 (py.+marc.+aspy.+/-qtz.)
Stage 3 (pyrite+/-barite)

Table 6. Fire assays of stage 3 pyrite

Sample #	Lab. #	weight(g)	Au by AA (ppm)	Au in sample (ppm)
L3	862	8.3	31	3.73
31	863	5.14	27	5.25
L2	864	3	11	3.6

Note: The analytical errors are believed to be ± 5% or less assuming that the errors are the same as previously analyzed duplicates of standard samples. The limited amount of pyrite sample prohibited making duplicate analyses.

FLUID INCLUSION STUDIES

Inclusions in quartz

Fluid inclusions in stage 2 quartz and stage 1 quartz were studied. Brecciated quartz from stage 1 mineralization were only studied under ordinary petrographic microscope using immersion oil. Eight types of fluid inclusions were identified in quartz varieties from the Lone Tree mine (Fig. 17). These fluid inclusions include: 1) Type a, one-phase liquid inclusions, 2) Type b, one-phase vapor inclusions, 3) Types c and d, two phase (vapor + liquid) vapor-rich and liquid-rich inclusions, respectively, 4) Type e, two phase (CO_2 vapor + liquid) liquid-rich inclusions, 5) Type f, three phase (CO_2 vapor + CO_2 liquid + liquid) inclusions at room temperature, 6) Type g, three phase (vapor + liquid + solid) halite-bearing inclusions, and 7) Type h, multiphase (vapor + liquid + solid1 + solid2) inclusions. Type h

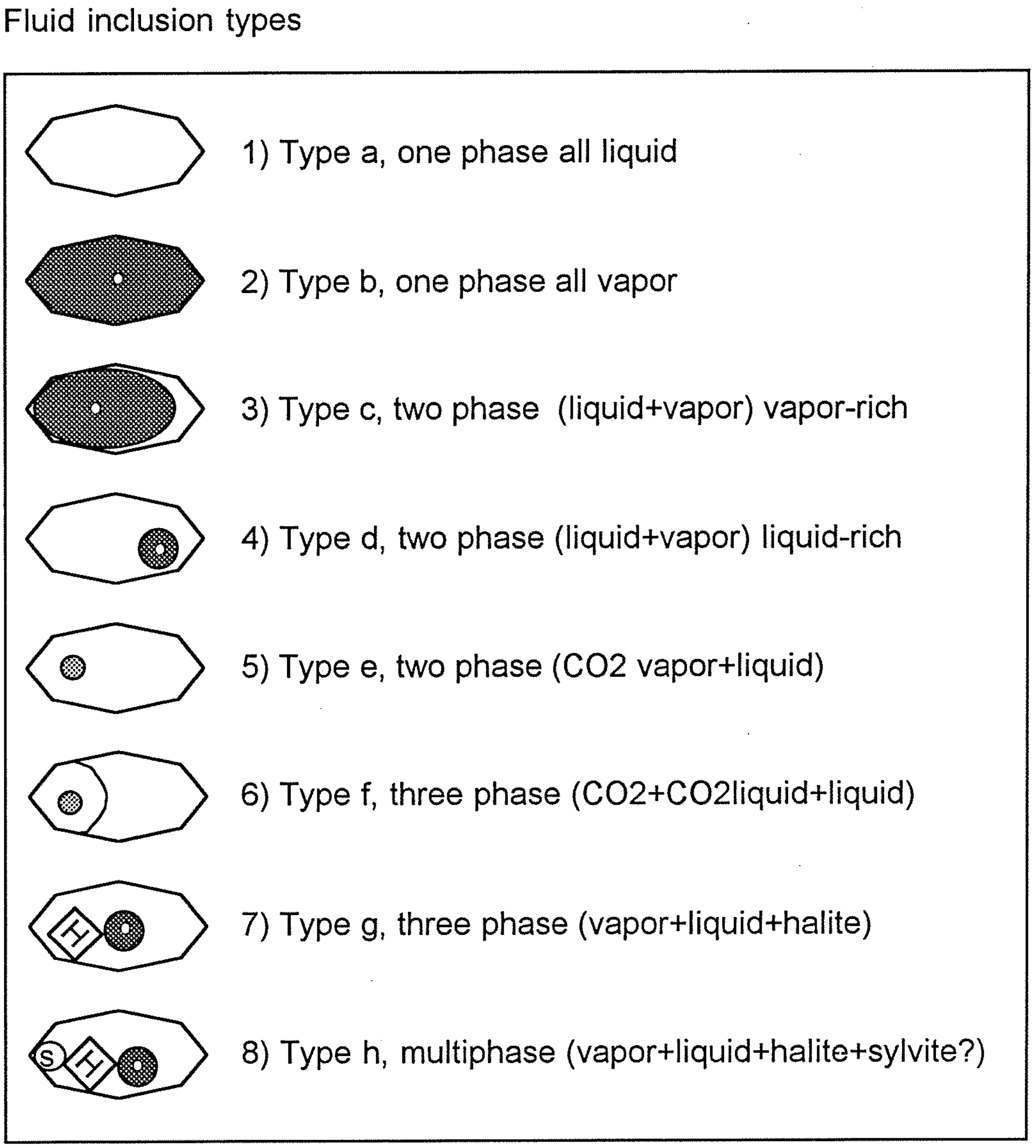

Figure 17. Eight types of fluid inclusions observed in stage 1 quartz, stage 2 quartz, and barite in stage 3.

inclusions were only identified in one sample and are represented by a halite crystal with an attached small rounded crystal with high relief. Carbondioxide bearing inclusions (type e and f) as well as some type a, b, c, and d inclusions are aligned along the traces of fracture planes suggesting that they are secondary inclusions. The CO_2 bubble in type e inclusions is faintly visible and is rapidly moving. Primary inclusions are distributed randomly as single inclusions, as groups of inclusions where their orientation mimics the crystal face, and as oriented inclusions along growth planes. The primary inclusions are oval, oblate, circular, and rarely irregular in shape. The size of the inclusions ranges from 3 µm to 50 µm and most are between 12 µm and 20 µm. Secondary inclusions were identified as trails along healed fractures that crosscut quartz grains or growth bands. The secondary inclusions are rodlike, flat, or negative crystal shapes. Their size is generally smaller than that of primary inclusions and average ~10 µm.

Type b, c, d, and g inclusions were observed in Stage 2 quartz (Fig. 18, 21A and B). Four of six quartz samples (qtz #1, 9, 10, and clt 626) studied contain type g inclusions along with small numbers of other three types. There are no coexisting halite-bearing and liquid-rich inclusions. Only at one location, a vapor-rich inclusion and a halite-bearing inclusion were observed close to each other. In one

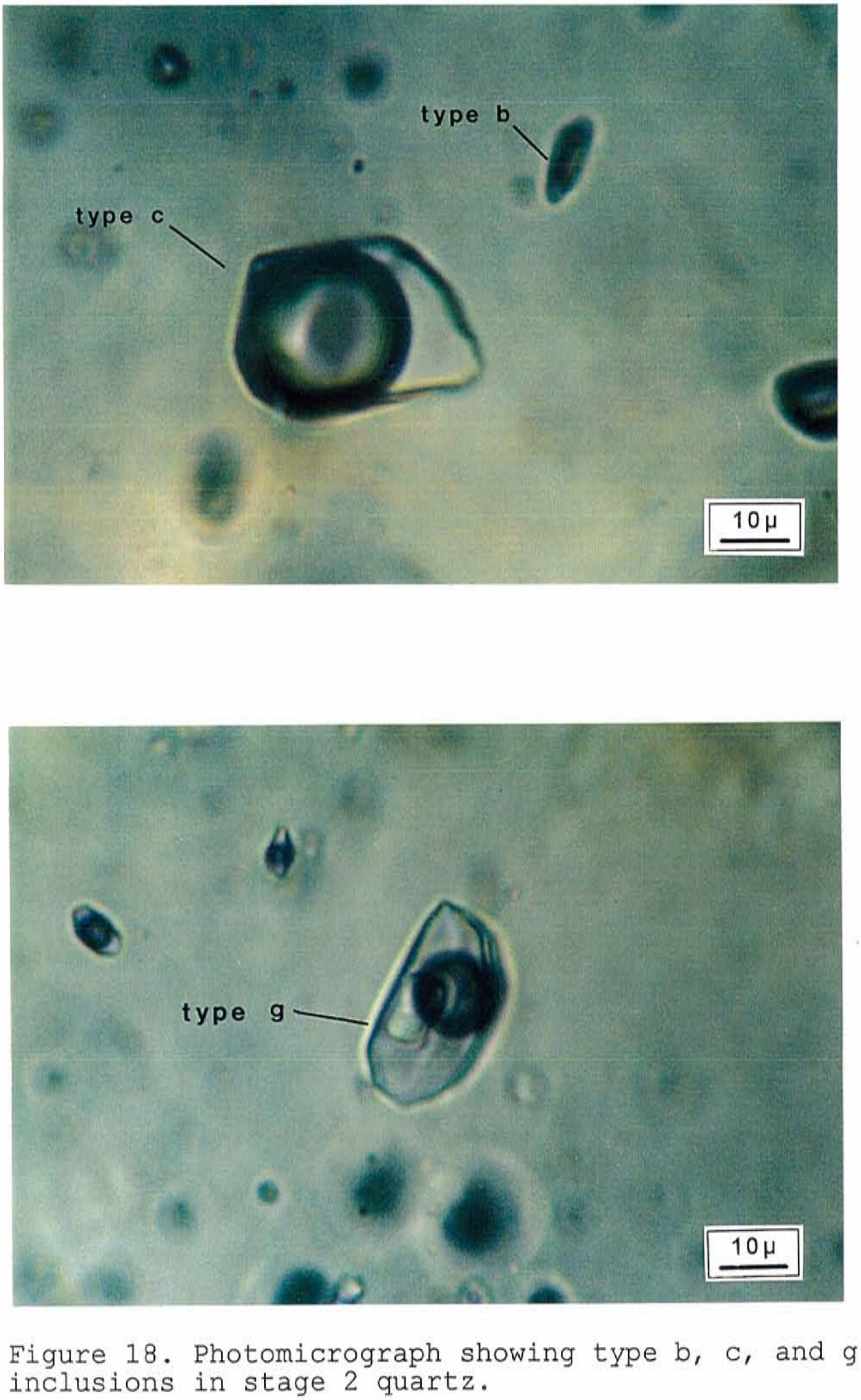

Figure 18. Photomicrograph showing type b, c, and g inclusions in stage 2 quartz.

inclusion, two cubic solid phases were noted together with liquid and gas phases. These are most likely sylvite accompanied by a halite crystal. The other two quartz chips (qtz # 12, and 20) hosted mainly inclusions of type b, c, and d. No separate CO_2 liquid phase was observed in the inclusions hosted in stage 2 quartz.

Inclusions in barite

Fluid inclusions were studied in barite crystals from six different samples. Barite chips contain type a and d inclusions, with type a dominant. Some of the chips with a clear appearance did not contain any fluid inclusions. Primary inclusions occur as single isolated inclusions, and as group of inclusions. Secondary inclusions are more abundant than primary inclusions and they are oriented parallel to the traces of fractures. The secondary inclusions comprise type a and d inclusions, but type d inclusions are occasionally seen. A few inclusions have small dark tails extending from the narrow side of the inclusion, which indicates necking down. The size of the inclusions ranges from 5 µm to 65 µm in length.

Microthermometry

Heating and freezing measurements were made on a total of 238 fluid inclusions in Stage 2 quartz and Stage 3 barite. The microthermometric data is provided in appendix A. The homogenization temperatures (Th) for the inclusions in Stage 2 quartz fall between 185 °C and 411 °C; and the dominant population records a temperature of ~270 °C (Fig. 19). Among the measured 201 inclusions in quartz, 48 are type g inclusion. Fourteen of halite-bearing inclusions homogenized by halite dissolution, whereas the other 34 inclusions homogenized by vapor bubble disappearance. The temperatures of halite dissolution (Ts) range from 121 °C to 346 °C (Fig. 20). At room temperature some of the saline inclusions did not have halite crystals but upon cooling halite crystals were precipitated. This can be explained by metastability of the fluid (Roedder, 1984). Halite dissolution generally occurred at temperatures between 230 and 260 °C. The Th of halite-bearing inclusions corresponds to the temperatures of vapor bubble disappearance or the complete dissolution of halite, whichever is higher.

Vapor-rich inclusions homogenized mostly into the vapor phase during which vapor bubble expanded and filled the whole inclusion. The Th of vapor-rich inclusions ranges from 270 to 411 °C. In some rare cases vapor-rich appearing inclusions homogenized into the liquid phase by disappearance of vapor bubble. The Th for this mode of homogenization is in the range of 332-403 °C.

The liquid-rich inclusions homogenized into liquid phase by disappearance of vapor bubble. The Th of liquid-rich inclusions is lower than for vapor-rich inclusions. In one sample vapor-rich and liquid-rich inclusions are very close to each other. The type c inclusion homogenizes into

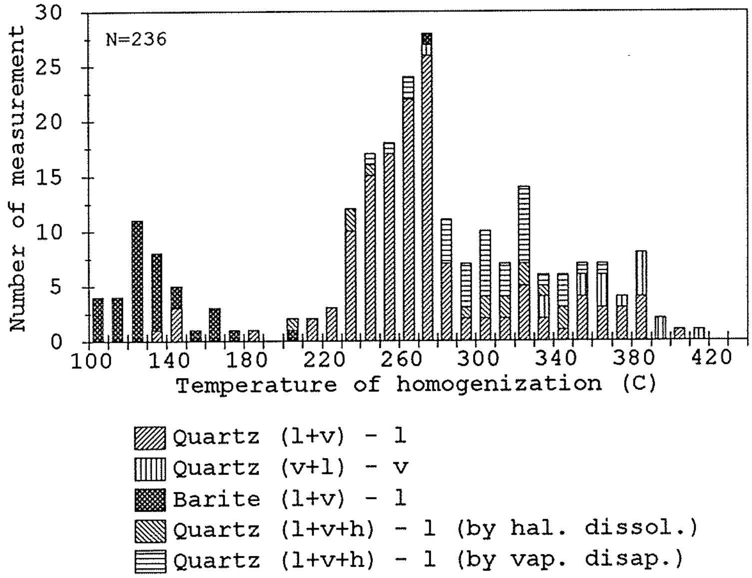

Figure 19. Histogram for temperature of homogenization of all primary and secondary inclusions.

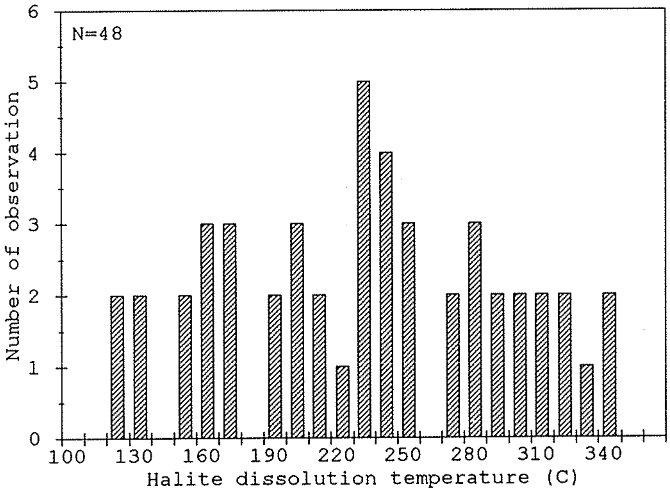

Figure 20. Histogram for halite dissolution temperatures.

vapor phase at 379 °C, and the type d inclusion homogenizes into liquid phase at 322 °C. Fig. 21A shows the photomicrograph of coexisting vapor-rich and liquid-rich inclusions. At another location, a vapor-rich inclusion is close to a halite-bearing inclusion. The vapor-rich inclusion homogenized into the vapor phase at 408 °C, and halite-bearing inclusion homogenized by halite dissolution at 330 °C. Fig. 21B is a photomicrograph of coexisting vapor-rich inclusion and halite-bearing inclusion. The coexistence of vapor-rich and liquid-rich inclusion may be indicative of boiling of mineralizing fluids. There was not a decrepitation problem during heating measurements. The secondary inclusions in quartz have lower Th ranging from 136 to 227 °C and Tm between -0.8 and -1.2 °C.

Fluid inclusions in barite have Th in the range of 103 and 174 °C, and primarily between 120-130 °C (Fig. 19). A few inclusions have high homogenization temperatures. Similar ice melting points suggest this may be due to the necking down.

Due to the evidence for the boiling of fluids as mentioned earlier, homogenization temperatures obtained from the inclusions in second stage quartz represent true trapping temperatures (Tt). However, inclusions in barite did not have any indication for the evidence of boiling, therefore the Th from these inclusions are only minimum values of Tt.

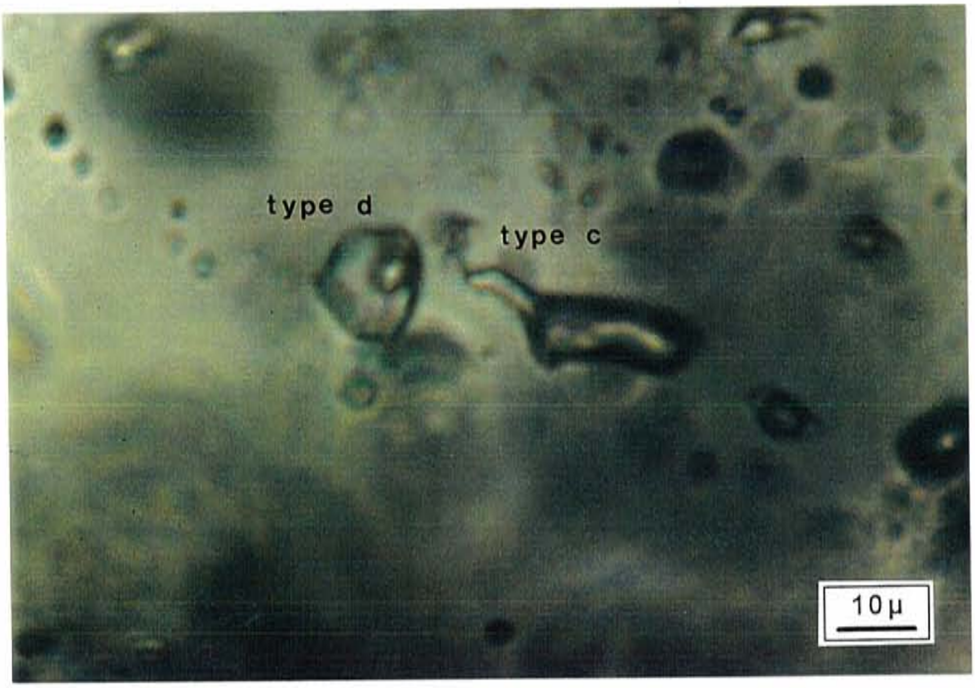

Figure 21A. Photomicrograph of coexisting vapor-rich and liquid-rich fluid inclusions.

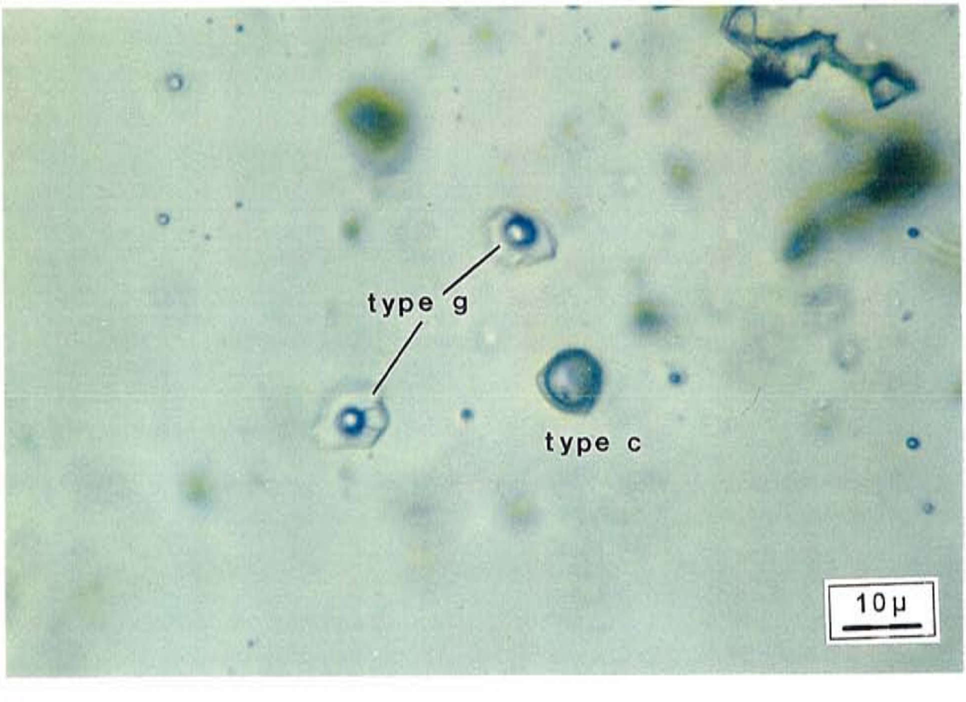

Figure 21B. Photomicrograph of coexisting vapor-rich and halite-bearing fluid inclusions.

Fluid salinities were calculated from halite dissolution temperatures (Potter et al., 1977), and the freezing point depression of water (Bodnar, 1993). The salinities of the inclusions in quartz range from 1.2 to 41.4 eq. wt. % NaCl and are plotted with respect to total Th in figure 22A and B. Also plotted in figure 22A is standard halite saturation curve from the data of Potter et al., 1977. It is apparent from the figure 22A that there are four different groups of data points. One group of data clusters at 211-300 °C and 1.23-8.14 eq. wt. % NaCl, other group of data assembles at 201-362 °C and 28.6-41.4 eq. wt. % NaCl, the third group of data gathers at 332-411 °C and 1.23-5.26 eq. wt. % NaCl, and a few data points plots at 140-145 °C and 1.4-1.74 eq. wt. % NaCl as a fourth group. In addition to that several data points plot between second and third groups of data in a transitional pattern. For clarity reasons, salinity versus Th plot for liquid-rich inclusions in two quartz samples (qtz # 12, and 20), that apparently lack halite-bearing inclusions, is given in figure 22B. These liquid-rich inclusions plot as three different groups and are generally similar to the liquid-rich inclusions in other four quartz samples containing halite-bearing inclusions (Fig. 22A and B). One group of data plot at 136-147 °C and 1.74-2.07 eq. wt. % NaCl, the other group of data points cluster tightly at 226-295 °C and 2.07-7.31 eq. wt. % NaCl, and the third group of data plot at 373-403 °C and

3.87-14.46 eq. wt. % NaCl (Fig. 22B).

Inclusions in barite have low salinities that range from 1.23 to 1.74 eq. wt. % NaCl (Fig. 22A). Two-phase liquid dominated (type d) and one-phase liquid (type a) inclusions have similar salinities. During cooling of type a inclusions, only two of them nucleated a vague vapor bubble which later disappeared slightly after ice melting occurred during heating period.

Neither hydrohalite nor clatharate formation are observed in quartz and barite inclusions. In a few type d inclusions in quartz, the boundary between liquid and vapor phase became blurry and subangular after freezing at around -95 °C. This irregular boundary vanished at -56.6 degrees upon heating the inclusion. This may indicate small amounts of CO_2 occurring in liquid phase.

Fluid inclusion microthermometry for stage 2 quartz and stage 3 barite

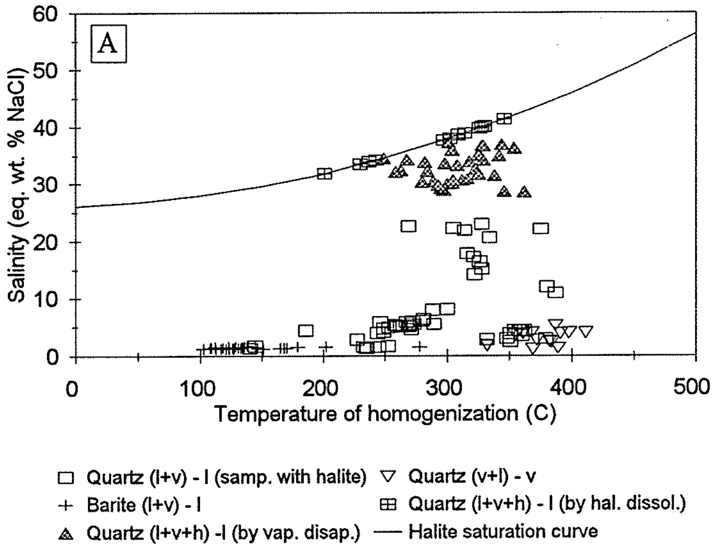

Figure 22A. Plot of salinity versus temperature of homogenization for fluid inclusions in quartz and barite excluding type d inclusions in quartz # 12 and 20 that lack halite-bearing inclusions. Total homogenization temperatures are used for halite-bearing inclusions.

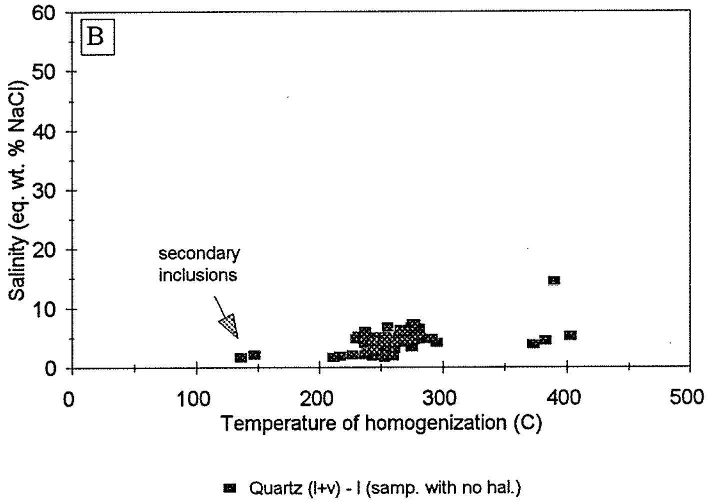

Figure 22B. Plot of salinity versus temperature of homogenization for type d inclusions in quartz # 12 and 20.

FLUID INCLUSION GAS ANALYSES

A total of twenty mineral separates including quartz, pyrite, pyrite ± marcasite ± arsenopyrite, and barite representative of different mineral paragenetic sequences were analyzed for their gas compositions in fluid inclusions. The analyses involved a total of 88 crushing processes in which each sample was crushed several times ranging from 3 to 9. The raw data is provided in Appendix B. The average values (mole%) for the gas species released from these multiple crushes for each mineral are given in Table 7. The CH_4/Ar, N_2/Ar, H_2S/Ar, CO_2/Ar, and C_nH_n/Ar ratios are given in Table 8. Even though there was no clear microthermometric evidence for CO_2 liquid phase in fluid inclusions, it is the most common gas specie in all quartz types and in stage 2 pyrite ranging from 2.0-4.67 mole%. The highest N_2 occurs in stage 1 quartz (0.71 mole%) that is followed by stage 2 pyrite (0.69 mole%), stage 3 pyrite (0.67 mole%), barite (0.59 mole%), and stage 2 quartz (0.23-0.20 mole%). The highest CH_4 (2.52 mole%) occurs in stage 2 pyrite, and it ranges from 0.22 to 0.27 mole% in quartz varieties and 0.07-0.33 mole% in stage 3 barite and pyrite. The H_2S content of the stage 2 quartz (0.005-0.008 mole%) is higher than those of the other minerals (0.0001-0.002 mole%). Hydrocarbon (C_nH_n) concentrations range between 0.006 and 0.02 mole% in barite and in stage 2 pyrite corresponding to lower and higher extremes respectively. The

small amounts of He (0.00083 mole%) is present only in stage 3 pyrite (Table 7). In all analyses, while Ar concentrations range from 0.002 to 0.009 mole%, the SO_2 concentrations range between 0.0002 and 0.0008 mole%. The average CH_4/Ar ratio ranges from 80 to 136 in all quartz types and it rises to a maximum of 574 in second stage pyrite and decreases substantially to lower values (32-36) in third stage minerals. The N_2/Ar ratio in first stage quartz is second highest (259) after that in barite (262). This ratio in other minerals fall between 72 and 157. The H_2S/Ar ratio varies from 0.01 in stage 3 pyrite to 3.2 in stage 2 quartz with halite-bearing inclusions. The CO_2/Ar ratio is extremely high in first and second stage minerals with a range of 1009-1241, whereas it drops to lower values in third stage minerals with a range of 54-69.
The hydrocarbon-argon ratio for all minerals varies from 1.3 to 6.2 with low and high extremes occurring in stage 3 and 2 pyrite respectively.

The CO_2/H_2S, N_2/Ar, and H_2S/Ar ratios are plotted for individual crushes of quartz samples (Fig. 23). The CO_2/H_2S ratio is highest in stage 1 quartz with a maximum value of 6362, and the ratio decreases in stage 2 quartz samples with a high value of 1351. In a similar way, the range and average values of N_2/Ar ratio in stage 1 quartz is as twice great as those in stage 2 quartz. In contrast, H_2S/Ar ratio increases gradually from stage 1 quartz with a high value

1.5 to stage 2 quartz with a high value of 7.0 (Fig. 23).

Table 7. The average mole% values for gas species in minerals from different stages of mineralization.

Gas mole%	Quartz1	Quartz2 +halite	Quartz2 no hal.	Pyrite2 ±Mc±As	Barite3	Pyrite3
He	>0.0001	>0.0001	>0.0001	>0.0001	>0.0001	0.00083
H2O	95.6194	96.6617	97.4959	92.0592	99.1764	98.3245
CH4	0.22159	0.27434	0.27152	2.52691	0.07491	0.33671
N2	0.712	0.23869	0.20099	0.69166	0.59711	0.67037
H2S	0.002348	0.008011	0.005475	0.001113	0.001389	0.00013
Ar	0.002741	0.002437	0.001983	0.004397	0.002272	0.00923
CO2	3.404056	2.784991	2.001069	4.677173	0.124362	0.64204
CnHn	0.014517	0.009742	0.009003	0.027349	0.006124	0.01207
SO2	0.000808	0.000657	0.000541	0.000661	0.000209	0.00039

Table 8. Gas ratios in minerals from different stages of mineralization.

Gas ratios	quartz1	quartz2 +halite	quartz2 no hal.	pyrite2 ±Mc±As	barite3	pyrite3
CH4/Ar	80.8442	112.5737	136.9228	574.6457	32.9698	36.4587
N2/Ar	259.759	97.9458	101.3575	157.2915	262.7966	72.5862
H2S/Ar	0.85662	3.28724	2.76096	0.25303	0.61144	0.01417
CO2/Ar	1241.903	1142.795	1009.112	1063.639	54.733	69.518
CnHn/Ar	5.29624	3.99754	4.54009	6.21953	2.69506	1.30770

Note: The numbers 1, 2, and 3 stand for the stages of mineralization. Second stage quartz is divided into two groups according to their fluid inclusion contents as ones containing halite crystals and ones with no halite crystals in them.

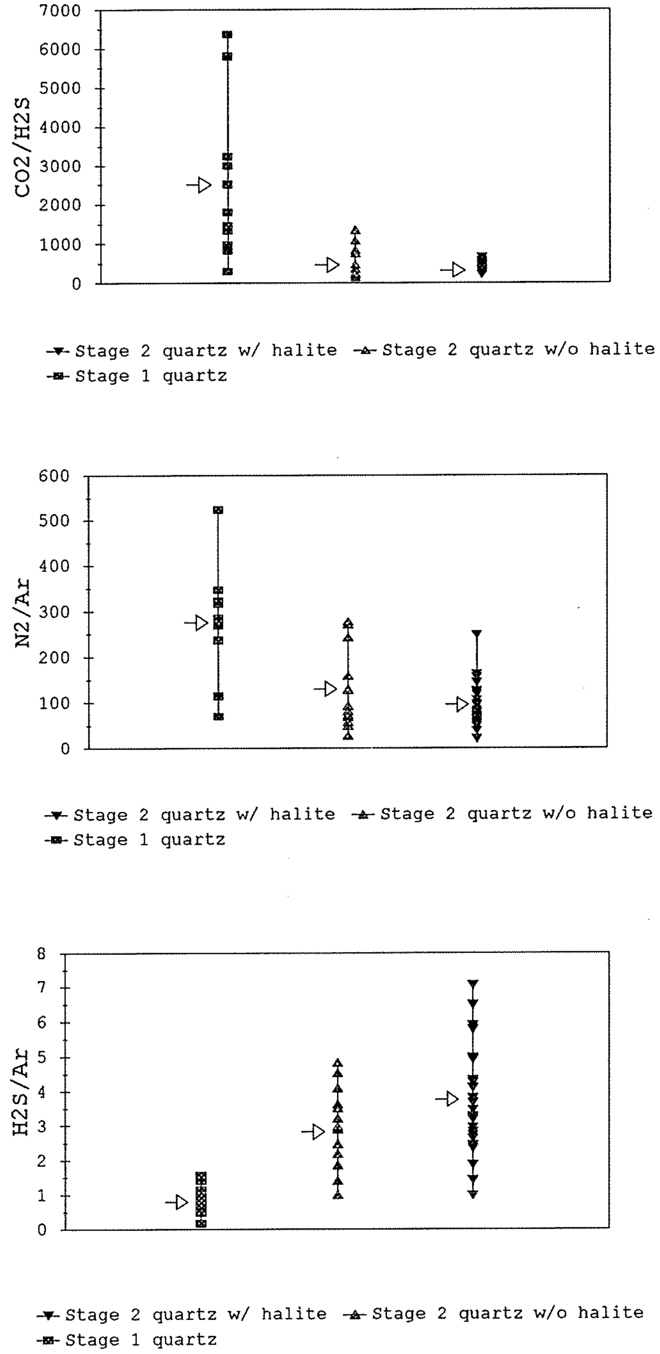

Figure 23. Plots of gas ratios (CO_2/H_2S, N_2/Ar, and H_2S/Ar) for individual crushes of quartz samples from stage 1 and 2 mineralization. Arrows indicate average values for ratios.

The amount of total gas is highest in second stage pyrite ranging from 1.8 to 17.0 mole%, which is followed by that in stage 2 quartz (1.1-6.2 mole%), stage 1 quartz (1.7-5.9 mole%), stage 3 pyrite (0.5-4.4 mole%), and lastly barite (0.28-1.6) (Fig. 24).

Pressure and depth estimates

The fluid pressure at the time of fluid inclusion entrapment is equal to the sum of partial pressures of the gaseous species dissolved in the fluid phase (Norman et al., 1985). The pressure is directly related to the amount of dissolved gaseous species and the Henry's Law constant which varies with temperature and salinity. The pressure can be calculated from the combination of fluid inclusion and gas analyses data. While fluid inclusion data provides salinity and trapping temperature, gas data gives the gaseous compositions required for this objective. The calculations performed for type c inclusions in the second stage quartz #12 assuming a multicomponent vapor separation indicate a pressure of 228 bars corresponding to 3180 meters depth of boiling. This calculated pressure is for the inclusion fluids that has a salinity of ~4.5 eq. wt. % NaCl and temperature of ~358 °C, and contains the least amount of gaseous species, ~1.18 mole% (crush # 5060 a). This fluid inclusion represents approximately average Th and salinity values for type c inclusions. The minimum pressure of the liquid phase in these type c inclusions can be determined by

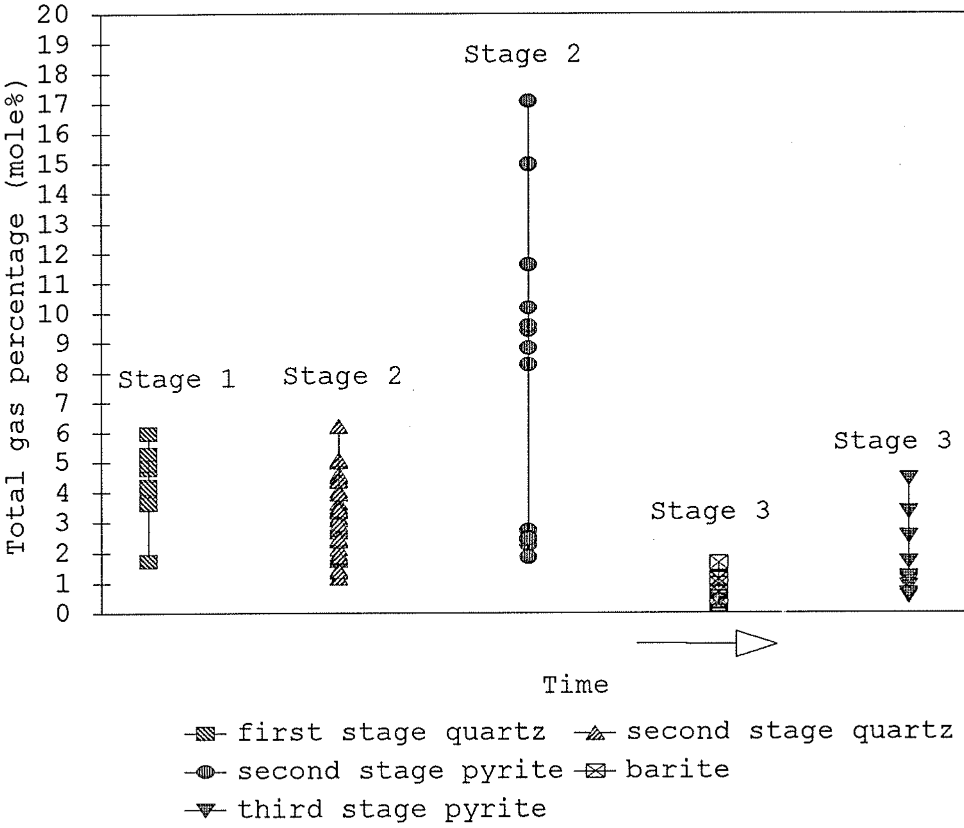

Figure 24. Plot of total gases (mole%) in minerals from stage 1, stage 2, and stage 3 mineralization. The relatively high amounts of total gases in stage 2 minerals indicate fluid boiling during stage 2 mineralization.

the intersection of liquid-vapor curve and isochore for fluids with salinities ~4.5 eq. wt. % NaCl (Fig. 25). The intersection point indicates a minimum pressure of 173 bars (Fig. 25). Therefore, maximum pressure at the time of fluid inclusion entrapment is equal to 401 bars (Fig.25). Thus pressure was probably fluctuating between these minimum and maximum values.

The high temperature, high gas content of the inclusions, and evidence of boiling as well as repeated sealing of fractures by multiple generations of silica indicate that the pressures to be hydrostatic or transitional between hydrostatic and lithostatic. However, the pressure and depth numbers may have been slightly overestimated than the actual values due to the release of excess gas from even only one vapor-rich inclusion.

Alternatively the conventional pressure and temperature space diagram is constructed for halite-bearing fluid inclusions (Fig. 26) in an attempt for better understanding of physical environments of mineralizing fluids at the Lone Tree mine. The positions of isochores and liquidus lines are located using Ts and temperature of vapor bubble disappearance Th(v). The liquidus line separates the stability field of liquid from that of halite + liquid. Previously, the determination of pressure and temperature conditions at the time of fluid entrapment was difficult from heating data of halite-bearing fluid inclusions due to

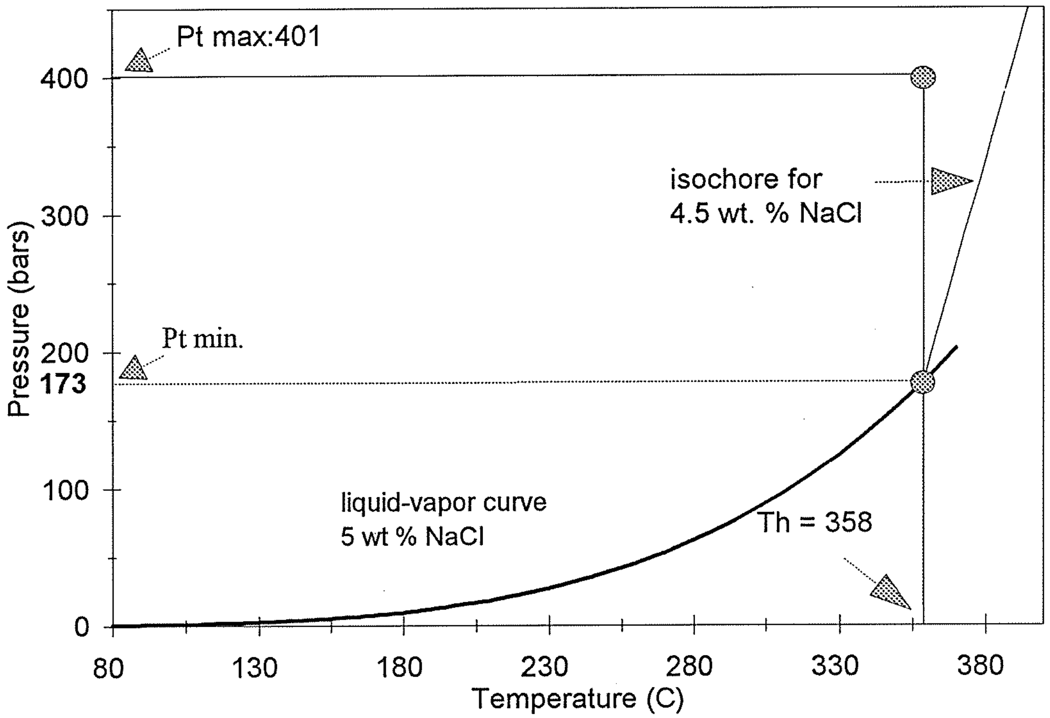

Figure 25. Pressure versus temperature plot for type c inclusions. The intersection of liquid-vapor curve with isochore for fluids with ~4.5 eq. wt. % NaCl indicates a minimum pressure of 173 bars. The summation of the total vapor pressure of the gas phases to this minimum pressure gives a maximum pressure of 401 bars at hydrostatic conditions. The vapor-liquid curve is plotted using data from Haas (1976).

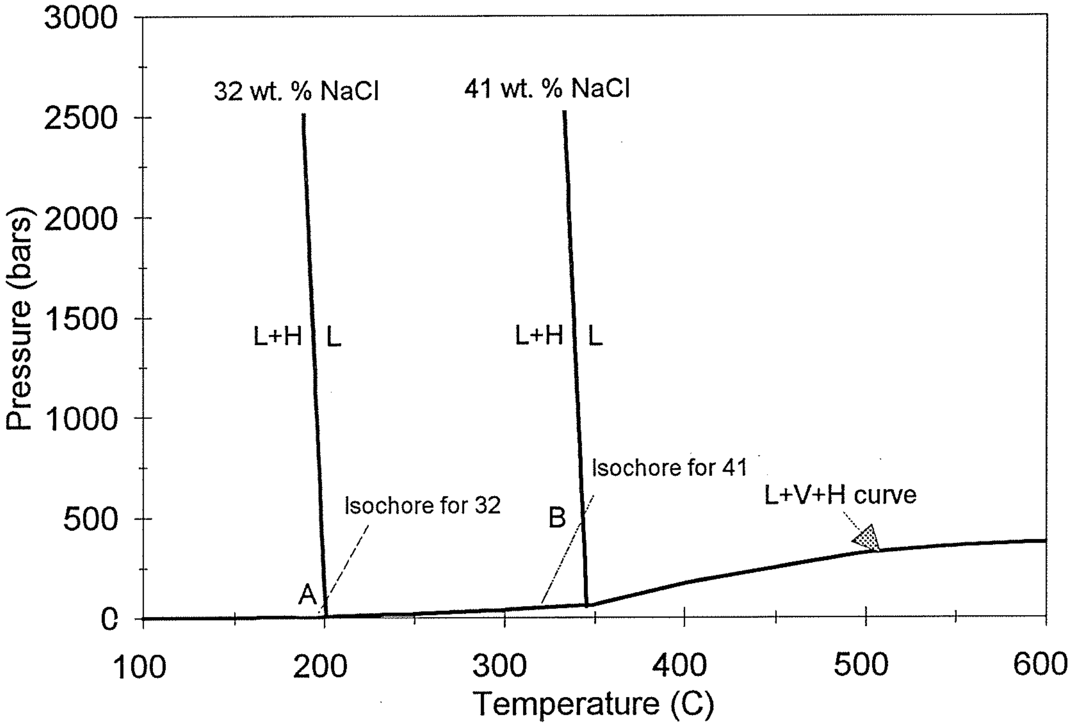

Figure 26. Pressure versus temperature space diagram for two representative halite-bearing fluid inclusions. Isochores for these fluid inclusions indicate a minimum pressures of 100 bars (point A) and 500 bars (point B). In general, 500 bars can be considered as the minimum pressure.

the lack of necessary experimental data to determine slope of liquidus line. A recent study (Bodnar, 1994) provided this data for a fluid with a salinity of 40 eq. wt. % NaCl. The liquidus for this fluid has a negative slope of -5.5 °C/kbar. This study also shows that the slope of the isochores changes at intersection point with liquidus line and are steeper on left side of the liquidus line than the same isochore on the right of liquidus line.

The liquidus lines for fluids with a salinity of ~32 and ~41 eq. wt. % NaCl are drawn on Figure 26 using the equation of Bodnar (1994). The isochores for two inclusion fluids representative of above salinities are plotted across the liquidus as straight dashed lines using the FLINCOR microcomputer program developed by Brown (1989). No attempt has been done to estimate the change in the slope of isochore on the left side of the liquidus line. The isochore for one fluid inclusion with a Ts of 201 °C originates from Th(v) of 196 °C, and for the other inclusion with Ts of 346 °C starts from Th(v) of 323 °C (Fig. 26). The points where the isochores for fluids with a salinity of 32 and 41 eq. wt. % NaCl intersect the liquidus line for the same fluids define a minimum pressure of ~100 (point A) and ~500 bars (point B), respectively (Fig. 26).

$^{40}Ar/^{39}Ar$ DATING OF BARITE

Absolute abundance determinations

The absolute abundance of K, Ca, and Cl can be inferred from the argon isotopic results. Irradiation in the nuclear reactor produces argon isotopes from potassium, calcium, and chlorine (Faure, 1986). Namely, ^{39}Ar is produced from ^{39}K, ^{37}Ar is from ^{40}Ca, and ^{38}Ar from ^{37}Cl. The amount of ^{39}Ar, and ^{37}Ar are calculated as moles per milligram and given with other relevant data in Table 9 for laser analyses and in Table 10 for furnace analyses. The ^{39}Ar concentrations determined from the laser data are in close agreement with those from the furnace data for samples from the Lone Tree, Lakes, and Rain deposits (Table 9 and 10). However, The ^{39}Ar concentrations from the laser analyses are two orders of magnitude greater for the Buchans deposit, one order of magnitude higher for the Hansonburg and Betze-Post deposits, and one order of magnitude less for the sample from the Bredehorn deposit (Table 9 and 10). As will be discussed, the difference in concentrations may be a result of contamination by reactive gases, rather than a heterogenous potassium distribution in barite.

Potassium concentration from ^{39}Ar signal

The concentration of potassium (Table 11) can be estimated from the ^{39}Ar signal using the equations below

$$^{40}K = \lambda \; ^{39}Ar/J \; \lambda e \tag{1}$$

$$\Sigma K(ppm) = \frac{K(g/mole) * 10^{3} mg/g * 10^{6} * \Sigma K(moles)}{weight\ (mg)} \tag{2}$$

The amount of ^{40}K (moles) can be calculated by inserting the measured ^{39}Ar signal, J-factor, and decay constants (λ and λe). Since the $^{40}K/K$ is known, the total K can be obtained. Potassium can be expressed as parts per million (ppm) using (2) and substituting 39.098304 (g/mole) for K. The concentration of potassium calculated from the laser and furnace analyses for the Lone Tree and Lakes barite seems to be in good agreement (Table 11). However, it is not the case for the other samples, especially for the Buchans barite with a 2000% difference between the two values.
K concentrations calculated from the furnace data are lower than those from the laser data, except for Bredehorn sample (Table 11).

Results of these calculations indicate that barite contains low amounts of potassium (Table C-3 and Table 11) and is confirmed by the AA analyses.

The amount of ^{37}Ar (moles/mg) ranges from 5.1e-19 to 2.3e-16 for laser analyses and 2.6e-18 to 7.2e-17 for furnace analyses (Table 9 and 10). These values except for 2.3e-16 (Getchell 2920-02) reveal a low calcium content.

Table 9. The amount of ^{39}Ar/mg and ^{37}Ar/mg with other relevant data for laser analyses.

Material (Barite)	Weight (mg)	^{39}Ar (mol./mg)	Total ^{40}Ar (mol./mg)	^{40}Ar/^{36}Ar	^{37}Ar (mol./mg)
Lakes	6.16	5e-17	2.0e-14	377	4.2e-17
Rain	4.1	4e-17	3.4e-14	392	1.5e-17
Buchans	4.99	2e-16	4.5e-14	325	8.1e-17
Hansonburg	2.15	2e-17	2.1e-14	366	6.8e-18
Betze-post	4	2e-17	2.2e-15	275	5.2e-17
Bredehorn	2	1e-17	1.3e-13	311	7.2e-18
Lone Tree 2919-01	11	3e-18	6.1e-15	295	2.4e-18
Lone Tree 2919-02	5	9e-18	5.5e-15	309	3.3e-18
Lone Tree 2919-03	5.4	7e-18	2.6e-15	320	3e-18
Lone Tree 2919-04	8.3	7e-18	8.4e-15	303	1.2e-18
Lone Tree 2919-05	5.6	7e-18	4.5e-15	321	5.1e-19
Getchell 2920-01	8.1	5e-18	1.4e-14	310	6.7e-18
Getchell 2920-02	4.2	2e-17	1.3e-14	338	2.3e-16

Table 10. The amount of ^{39}Ar/mg and ^{37}Ar/mg with other relevant data for resistance furnace analyses.

Material (Barite)	Weight (mg)	^{39}Ar (mol./mg)	Total ^{40}Ar (mol./mg)	^{40}Ar/^{36}Ar	^{37}Ar (mol./mg)
Lakes	97.6	5e-17	9.3e-15	297	7.2e-17
Rain	122.7	3e-17	1.3e-14	388	2.7e-17
Buchans	88	8e-18	1.8e-14	316	2.7e-17
Hansonburg	69	4e-18	9.3e-15	338	3.8e-18
Betze-post	65.3	3e-18	2.2e-15	298	6.6e-18
Bredehorn	159.3	3e-17	4.7e-14	330	2.5e-17
Lone Tree	87.1	5e-18	2.7e-15	306	2.6e-18

Table 11. The results of atomic absorption analyses for potassium in barite samples along with K calculated from ^{39}Ar signal.

Sample Id.	Lab no.	AA K (ppm)	^{39}Ar K (ppm)
Buchans	640	56	340,**16**
Rain	641	129,132	83,**55**
Lakes	642	66	106,**95**
Getchell	643	<30,<30	9,38
Bredehorn	644	56	19,**58**
Betze-post	645	<30	32,**6**
Lone Tree	646	<30,<30	7,18,14,15,14,**11**
Hansonburg	647	46,<30	34,**7**

Note: Bold numbers represent values for furnace analyses.

^{40}Ar/^{39}Ar

Argon isotopic data for the laser and furnace step heating analyses are given in Table C-1 and Table C-2, respectively. Age spectra, percent radiogenic argon, K/Ca ratio, and K/Cl ratio are plotted for laser data from Lone Tree, Lakes, Rain, Buchans, and Hansonburg barite samples (Fig. C-1). Age spectra for furnace data from the above samples, plus the Betze-Post barite sample are plotted in the same fashion (Fig. C-2). The reactive gases, proved difficult to remove from the measured gas. This uncleanliness of the gas was evident from the peak-height versus time regressions. For example, nonlinear behavior for ^{40}Ar indicates that gas is not properly purified. In addition, if the ^{40}Ar signal is $> 1\text{x}10^{-14}$ moles and the intercept error is > 0.1%, it suggests poorly cleaned sample gas.

Laser step heating analyses

Five barite aliquots from the Lone Tree deposit were incrementally heated in three steps using the CO_2 laser. The total gas ages obtained from these runs (run # 2919-01, 02, 03, 04 ,and 05) had uncertainties larger than 100%. None of the heating steps give reliable age information because there was essentially no detectable ^{39}Ar or radiogenic signal (Fig. 27 and Table C-1). The first heating step evolved nearly all of the ^{40}Ar and no steps indicate the

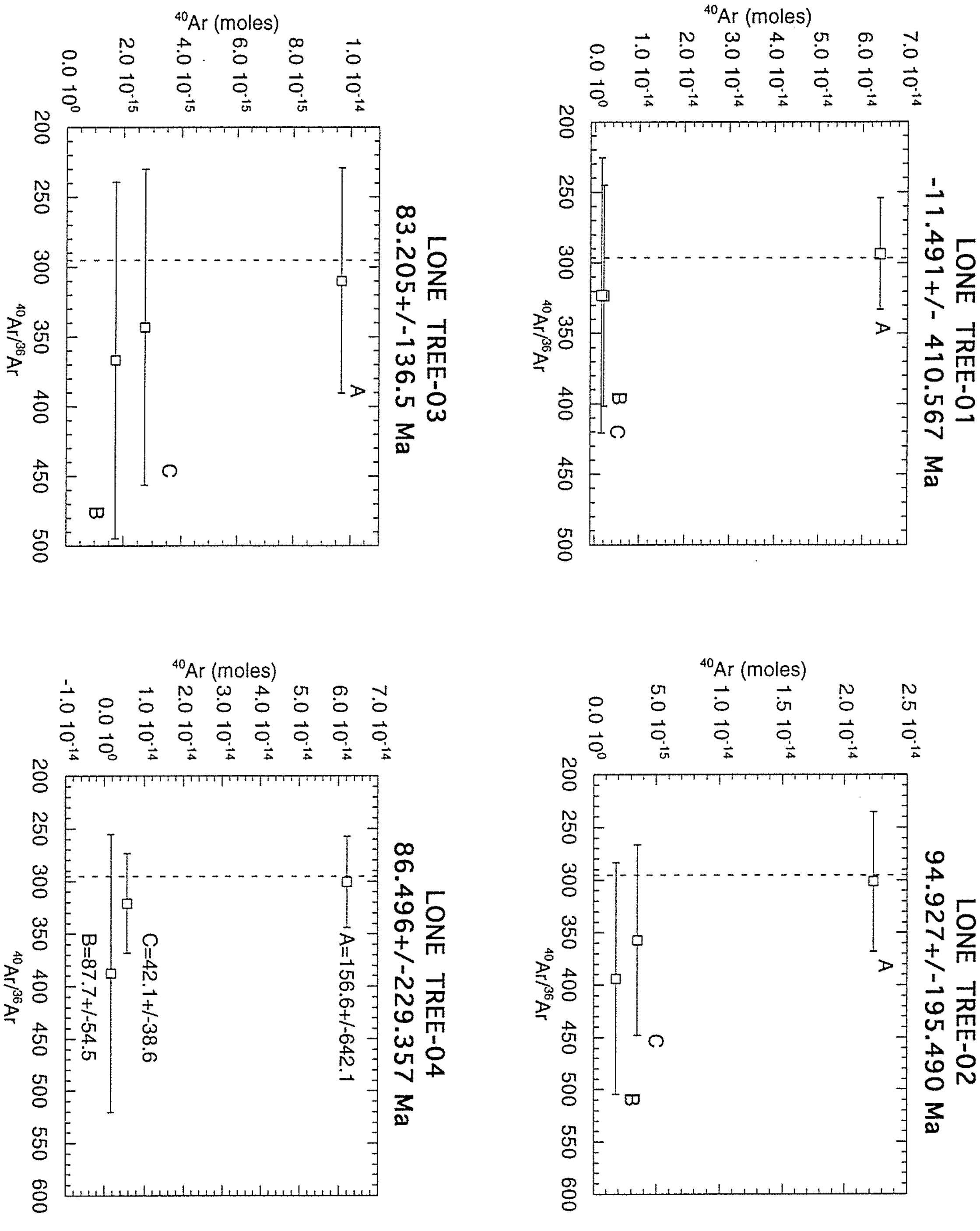

Figure 27. The plot of total ^{40}Ar versus ^{40}Ar/^{36}Ar ratio for laser analyses of Lone Tree and Getchell samples. Atmospheric ^{40}Ar can be burned off at low temperature steps, and if barite had K, we could probably date it.

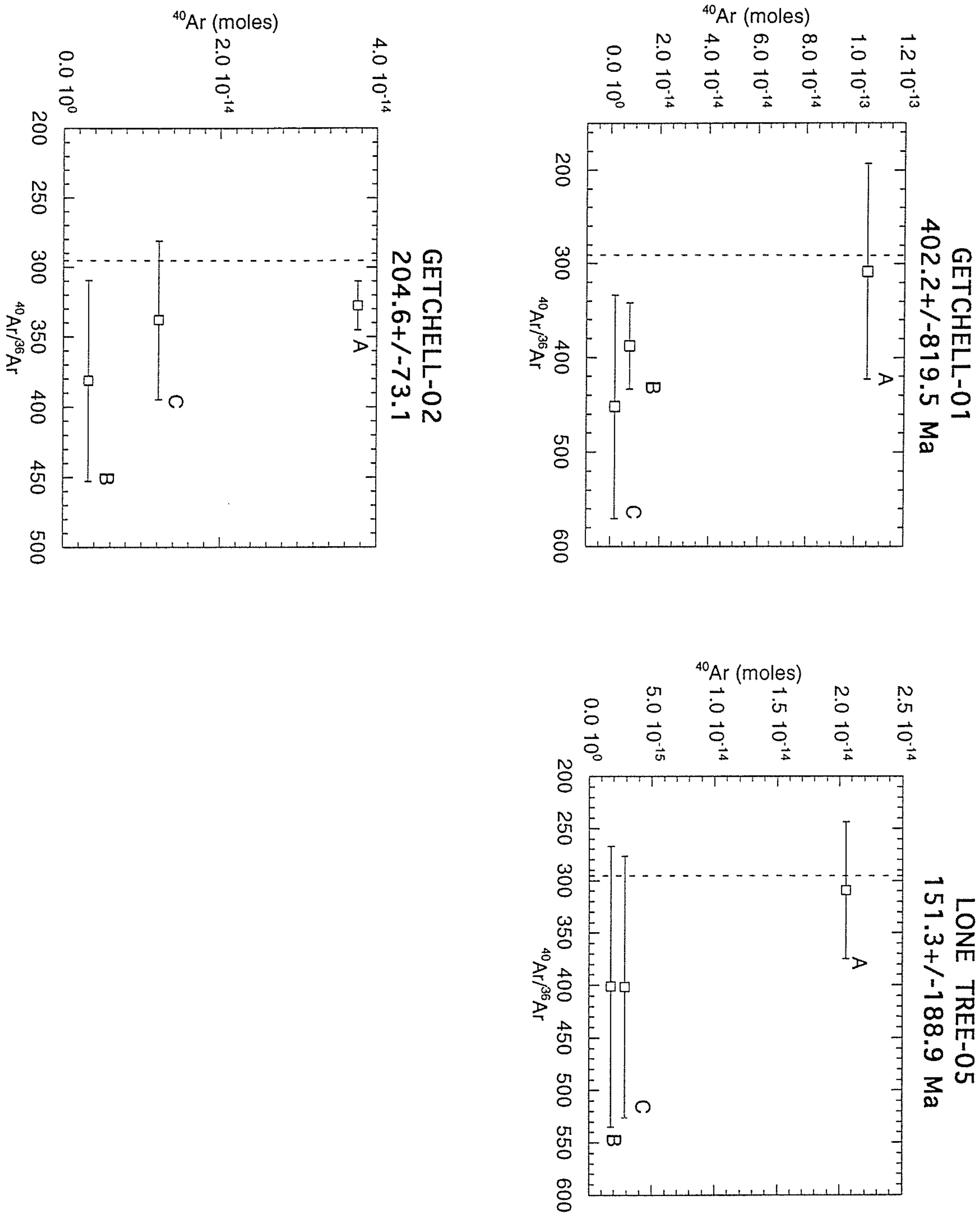

Figure 27 continued

presence of excess argon (Fig. 27). Additionally, only trace amounts of Ca and Cl are suggested by minute signals of ^{37}Ar and ^{38}Ar.

Two samples from the Getchell and one sample from each of Lakes, Rain, Buchans, Hansonburg, Betze-Post, and Bredehorn deposits were heated in three steps similar to the Lone Tree samples. The ^{40}Ar signal sizes for these samples range from 7.6e-16 to 1.7e-13 moles and commonly range between 1e-14 and 7e-14 moles (Table C-1). Like the Lone Tree sample, the Getchell barite had essentially no detectable ^{39}Ar, but considerably more total ^{40}Ar (Table 9). Also, most of the total ^{40}Ar was degassed with the first heating-step and the second and third steps appear to yield ^{40}Ar/^{36}Ar ratios measurably above atmosphere (Fig. 27). The apparent Ca concentration for each sample varied significantly as run 2920-01 give 7×10^{-18} moles/mg of ^{37}Ar while 2920-02 gave $2.3x^{-16}$ moles/mg (Table 9).

The Hansonburg, Betze-Post, and Bredehorn barites have barely detectable ^{39}Ar and ^{37}Ar signals indicating essentially no K or Ca. The Bredehorn barite had the highest total ^{40}Ar of all the samples, and was essentially atmospheric (Table 9).

The Lakes, Rain, and Buchans barites appear to have the highest K concentrations based on their ^{39}Ar (Table 9 and 11). These samples also gave measurable radiogenic yields and measurable apparent ages (Table 1 and C-1). The age spectra for Lakes and Buchans are similar in that the first step is significantly older than the last two (Fig. C-1). The final two steps of the Lakes barite yields concordant ages of ~180 Ma while the final step of Buchans yields a precise apparent age of 23.6±1.8 Ma. The Rain barite provided only one step with measurable ^{39}Ar. This step yields an apparent age of 414±27 Ma. These three samples also had measurable ^{37}Ar signals (Table 9) and variable K/Ca ratios (Fig. C-1). Most of the heating steps for the Lakes, Rain, and Buchans barite gave K/Cl values ranging from 0.1 to 1.0 (Fig. C-1).

Furnace step heating analyses

Lakes barite

The lakes barite sample weighing 97.6 mg was incrementally heated in nine steps. The second stage gettering time was 7 minutes for each step. The age spectrum has an age gradient starting from negative ages in first 5 steps, and climbing successively to about 130±12 Ma, and then 255±15 Ma (Fig. C-2). Inspection of peak-height regression plots for ^{40}Ar indicates that steps A-E were not sufficiently cleaned of reactive gas. However, argon released from the later steps was satisfactorily clean and these steps are shown in black.

Rain barite

The rain barite sample weighing 122.7 mg was incrementally heated in nine steps. Second stage gettering time was 7 minutes per step. The age spectrum displays a saddle-shaped pattern with old initial ages that decline to a negative age for the 800 °C step, and then gradually rise to old ages at high temperatures. Review of the peak-height regression plot for ^{40}Ar indicates that none of the steps were clean, thus all of the data from this analysis is rejected from further considerations.

Buchans barite

The buchans barite sample weighing 88 mg was step heated in ten steps. Second stage gettering time was 7 minutes during the first step, 15 minutes for the each next two steps, and 20 minutes for the following steps (D-J). After increasing the gettering time to 20 minutes, argon was apparently being adequately cleaned. This sample yielded a very irregular age spectrum owing to large errors at certain steps. The most radiogenic argon came out in the first step corresponding approximately to 345±95 Ma. Some of the low and high temperature steps had high Cl/K ratio along with low radiogenic yield. The uncertainties in ages were typically high in these steps (Fig. C-2). The highest amount of ^{39}Ar was released at 800 °C heating step which yielded a very young age inconsistent with that of Ordovician deposit. Peak-height regression plot indicates that gas was unclean in this step. Thus part of the data is unreliable and it is discarded from further considerations.

Hansonburg barite

The Hansonburg barite sample weighing 69 mg was step heated in eight steps. The second stage gettering time was 30 minutes for each steps. Low temperature steps had high Cl/K ratio and they did not provide any age information even though the radiogenic yield was ~15%. The only reason for not getting any age information appears to be very small ^{39}Ar signal. These steps are not included in age spectrum. Medium and high temperature steps gave an integrated age of 250±170 Ma.

Betze-Post barite

The Betze-Post barite sample weighing 65.3 mg was step heated in five steps. Second stage gettering time was 30 minutes for each steps. Only the last step gave measurable ^{39}Ar, and due to its low radiogenic yield the apparent age is very imprecise. Most of the ^{39}Ar came out in this high temperature step in which radiogenic yield was 6.1%.

Bredehorn barite

The Bredehorn barite sample weighing 159.3 mg was step heated in eight steps. Second stage gettering time was 30 minutes for each step but was still not sufficient to adequately clean the argon of reactive gases, therefore, the data is rejected from further discussions.

Lone Tree barite

The Lone Tree barite sample weighing 87.1 mg was step heated in nine steps. Second stage gettering was for 30 minutes and peak-height regressions suggest adequate gas clean-up. First two steps had a negative radiogenic yield mainly due to low amounts of total ^{40}Ar and the imprecision in ^{36}Ar measurement. Therefore these steps are excluded from the age spectrum. Steps G and H yielded measurable ^{39}Ar, but the apparent ages are still imprecise due to low radiogenic yield (Table C-2).

DISCUSSIONS

Characterization and sources of mineralizing fluids

Fluid inclusion data from the second stage quartz indicates four fluids, distinguishable by contrasting salinities and temperatures. The first fluid was of low to moderate salinity varying from 1.23-8.14 eq. wt.% NaCl and temperatures of 211-300 °C. The second fluid was characterized by high salinity, ranging from 28.6-41.4 eq. wt.% NaCl and temperatures of 201-362 °C. The third fluid type was distinguishable by its low density, low salinity (1.23-5.2 eq. wt. % NaCl) and relatively higher temperature (332-411 °C) nature. The fourth fluid was represented in a few secondary fluid inclusions and identified by its low salinity ranging from 1.4-2.07 eq. wt. % NaCl and lower temperatures between 136-147 °C. The very similar nature of the last fluid type to inclusion fluids in barite suggests that secondary inclusions in quartz entrapped fluids from third stage of mineralization. The first and second types of fluids were associated with a vapor-rich phase indicating fluid boiling. The coexisting type c and d inclusions have Th of 379 and 322 °C, homogenization occurring into vapor-phase and liquid-phase, respectively. The other coexisting type c and g inclusions homogenized by liquid evaporation and halite dissolution at 408 and 330 °C, respectively. Taking into account that the similar Th for type d and g inclusions in these pairs of inclusions, the slightly higher Th for type c inclusions may indicate trapping of two phases (liquid+vapor) or type g were trapped during periods of high pressure, and hence Th are minimum temperatures. The third fluid type also appears to be resulted from trapping of two phases, mostly vapor and minor liquid at high temperatures. The high amounts of total gases (mole%) from inclusions in stage 1 quartz, stage 2 quartz, and specifically stage 2 pyrite supports boiling of mineralizing fluids (Fig. 24) (Norman et al., 1996). Boiling is also evident from the ternary plots such as N_2-CH_4-CO_2, N_2-C_nH_n-CO_2, and CO_2-CH_4-H_2S, (Fig. 28A, B, and E) since gases partition into vapor phase from a boiling fluid at different rates (Henley, 1984). Therefore, ternary plots should reveal trends from gases that are highly soluble in the liquid phase (e.g., CO_2 and H_2S) to gases that strongly partition to the vapor phase

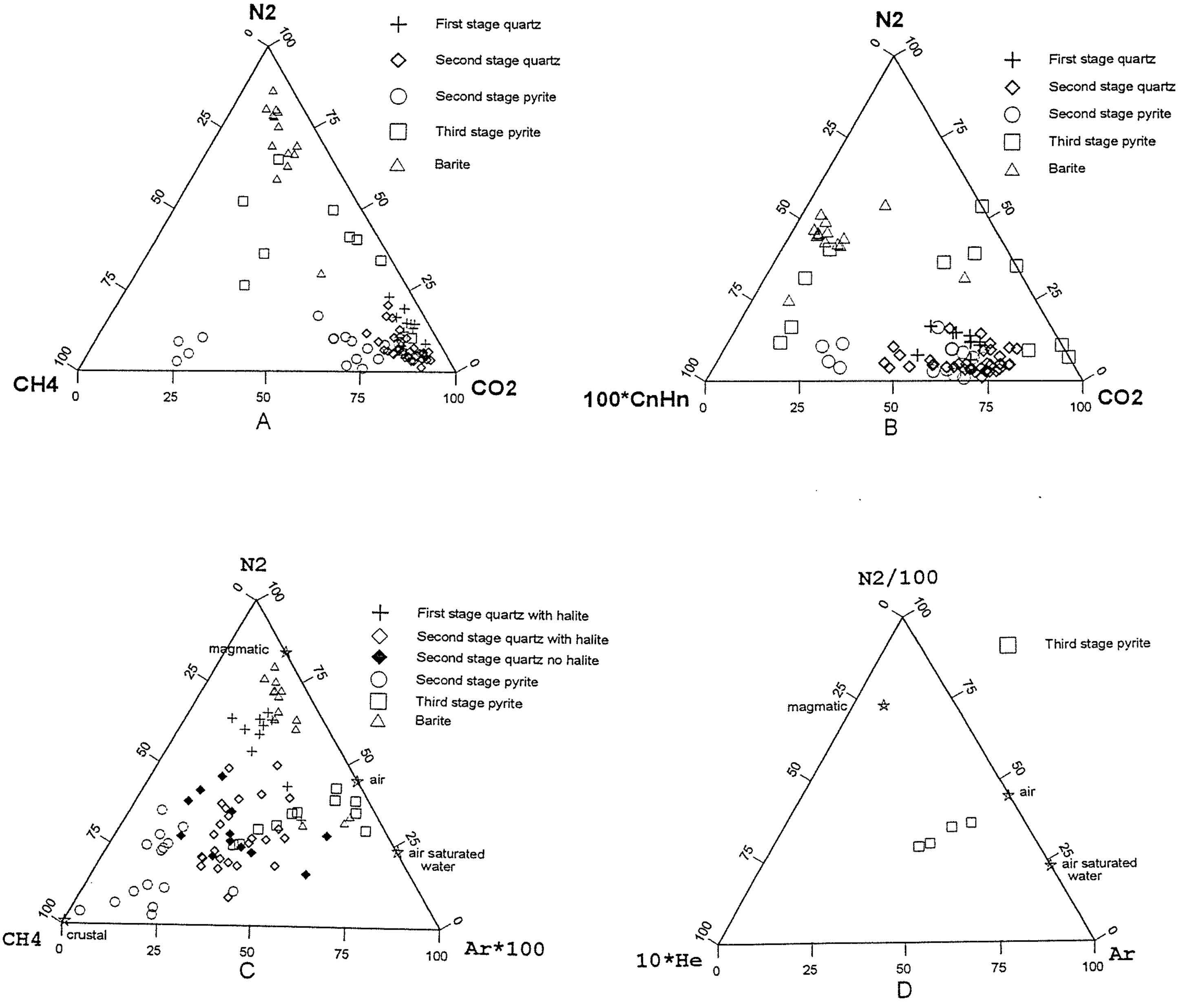

Figure 28. Ternary plots of A: (N_2-CH_4-CO_2), B: (N_2-100*CnHn-CO_2), C: (N_2-CH_4-Ar*100), D: (N_2/100-10*He-Ar), E: (CO_2/10-CH_4-100*H_2S), and F: (CO_2/10-CH_4-100*H_2S) in boiling model.

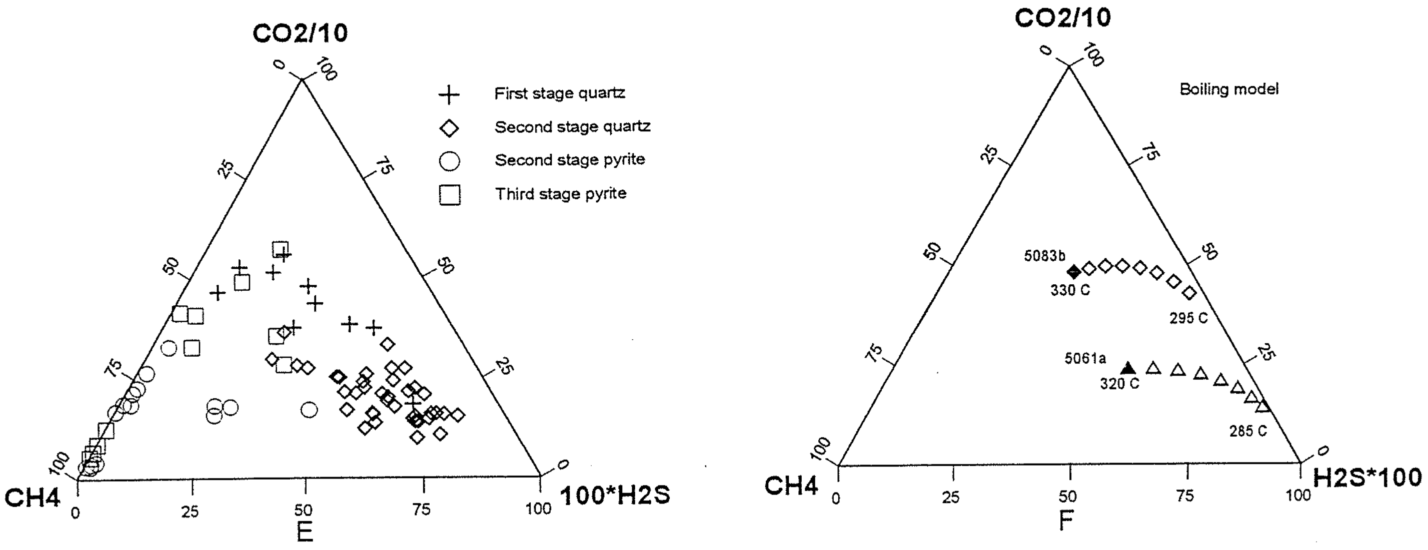

Figure 28 continued

(e.g., N_2 and CH_4). The calculations for the partition of gaseous species into vapor phase in a boiling model for stage 1 and 2 fluids indicate that boiling can produce a trend very similar to that observed in figure 28E (Fig. 28F). These calculations involve determination of the amount of gaseous species remaining in the liquid phase (CL) after a multistep vapor separation starting from 330 °C for stage 1 and 320 °C for stage 2 fluids and continuing for seven steps with a 5 °C decrease at every step. In this endeavor, the composition of the data point approximately at the middle of data cluster in figure 28E (e.g. crush # 5083b and 5061a) is chosen as a starting gas composition in the liquid phase. The gas distribution coefficient (B), the ratio of gas composition in vapor phase to gas composition in liquid phase, is determined from the equations of Giggenbach (1980). Vapor fraction (y) separating at each successive step is taken as 0.01. The details of the calculations for boiling model are given in Appendix B.

Magmatic input

High temperature and high salinity condensate suggest a magmatic contribution to the mineralizing fluids. Even though no microthermometric data is available from the brecciated quartz in stage 1, the observation of type e, f, and g inclusions suggest a magmatic water for the earliest stage of hydrothermal fluids as well. N_2-CH_4-Ar*100 ternary plot also shows that gas composition of the stage 1 fluids is very close to that of magmatic fluids (Fig. 28C). The N_2/Ar ratios > 100 as suggested by Norman and Musgrave (1994) as well as significant amounts of CO_2 concentrations in inclusion fluids from stage 1 and 2 minerals favor at least a partial magmatic input (Fig. 23), (Table 7 and 8). The role of magmatic water in the formation of porphyry copper deposits are very well known, especially for the potassic alteration zone in the core. Ahmad and Rose (1980) documented high salinity (32->60 eq. wt.% NaCl) as well as moderate salinity fluids (1-20 eq. wt.% NaCl) in both early and late stage quartz veins at the Santa Rita porphyry copper deposit. The high salinity fluids were attributed to a condensate coming from the underlying magma, whereas moderate salinity fluids were formed from heated meteoric waters. Similarly, Reynolds and Beane (1985) observed high-salinity high-temperature inclusions in early stage quartz and low-salinity and relatively low-temperature fluids in late-stage quartz from the Santa Rita deposit. They concluded that magmatic fluids were responsible for the potassic alteration and meteoric waters were responsible for the hypogene copper mineralization associated with phyllic alteration. The occurrence of even small amounts of base metals at the Lone Tree deposit, especially chalcopyrite with the gold-sulfide suit minerals also support a magmatic water contribution to the main gold stage mineralizing fluids. Fortitude gold-skarn deposit in the Copper Canyon area at the Battle Mountain-Eureka gold trend (Cortez trend) was formed by 38.5 Ma granodiorite intruding paleozoic carbonate and clastic rocks (Wotruba et al., 1988; Myers and Meinert 1991; Maher et al., 1993). Similarly, McCoy-Cove deposit is a gold-skarn deposit developed at the contact zone between silici-clastic rocks and 39.7 Ma monzonite-granodiorite stock (Kuyper, 1988). Kuyper (1988) reports a 39.7 Ma age for adularia from the gold-bearing quartz pyrite material from the McCoy-Cove deposit, supporting the genetic tie between mineralization and the magmatic intrusion. Betze-Post deposit, the largest sediment-hosted gold deposit is postulated to be related to an igneous stock on the basis of similarity between the ages of mineralization (117 Ma) and the nearby plutons (Arehart et al., 1993c). The intrusive igneous rocks delineated by the high magnetic intensity are closely associated spatially with the Carlin-type gold deposits in Nevada (Shawe, 1991).

Meteoric and crustal fluids

The occurrence of distinct fluids in the same sample may be explained by the mixing of high salinity waters with dilute to evolved ground waters that are heated to boiling. The evidence of boiling for the low to moderate salinity fluids (1.23-8.14 eq. wt. % NaCl) comes from the coexisting type c and d inclusions (Fig. 21A) and high gas content of fluid inclusions in stage 2 quartz that does not contain halite-bearing fluid inclusions (Fig. 24). A progressively decreasing trend in N_2 composition from high values in stage 1 quartz to relatively lesser values in stage 2 quartz as revealed in ternary plot may be a mixing trend from two end members (magmatic and meteoric)(Fig. 28C). Mixing of CO_2-rich brines and dilute CO_2-poor fluids were postulated to lead to gold precipitation at the Jerrit Canyon deposit (Hofstra et al., 1987; Hofstra et al., 1991).

Ternary plot for stage 2 pyrite indicates that mostly crustal fluids were responsible for pyrite and possibly for some gold mineralization as pyrite carries some gold (Fig. 28C). The crustal fluids may have been acquired by migrating magmatic fluids through the areas of crustal weaknesses to the area of mineralization. Deep crustal structures also controlled the alignment of Carlin-type deposits and the emplacement of associated igneous rocks (Shawe, 1991).

Fluid inclusions in barite from the third stage of mineralization have a salinity range of 1.23-1.74 eq. wt. % NaCl at temperatures of 103-174 °C. The low salinity and temperature nature of the fluids suggest primarily a meteoric water origin for this stage of mineralizing fluids and that appears to be distinctly different from the stage 2 fluids (Fig. 22A). This is also supported by the gas compositions of stage 3 barite and pyrite, which are distinctly different from those of stage 2 quartz or pyrite

(Fig. 28A, B, and C). There are only a few data points for gas compositions from stage 3 minerals similar to those from stage 2 minerals (Fig. 28B and C). It is also possible that these fluids may represent hydrothermal fluids highly modified by influx of unexchanged meteoric waters during the waning period of stage 2 fluids. There was no evidence for fluid boiling in inclusions. The total gas percentage in stage 3 minerals is less in comparison to that in stage 2 minerals (Fig. 24). The gas ratios except for N_2/Ar are much lesser than those in stage 2 minerals (Table 8). Taking into account the fluid composition and the temperature, the high N_2/Ar ratio can be explained in two ways. One way is that the third stage of mineralization could be a younger and shallower version of stage 1 and 2 mineralization. Accordingly, gas composition of meteoric waters may be highly modified by mixing with high N_2 fluids. The other way of explanation is that the fluids may acquire excess N_2 by water-rock interaction. One mechanism for the enrichment of N_2 is the oxidation of $NH4^+$ substituting for K^+ in the phyllosilicates and release of N_2 during the migration of ore fluids (Shepherd et al., 1991). As described by Madrid (1987) allocthonous rocks in the Roberts Mountain thrust contain thick sequences of black shales that could act as a source of N_2. However, the gas analyses of clay minerals from the altered areas at the Lone Tree mine indicates essentially no NH_3 component in clays, and thus ruling out this possibility. The other most likely mechanism is that the dilute meteoric waters can leach N_2 adsorbed by sedimentary rocks from the earlier magmatic fluids. The gas composition of inclusions in stage 3 pyrite plots very close to the air values in N_2-He-Ar ternary diagram suggesting an unevolved meteoric water origin as well (Fig. 28D). The growth banding texture in pyrite coating the barite also indicates the change in physico-chemical environment of mineralization (Craig and Vaughan, 1981).

Acidic fluids

Alteration minerals and some of the ore minerals can also provide information on fluid characteristics and environments of ore formation. The occurrence of marcasite with gold sulfide minerals indicates that the mineralizing fluids were acidic ($pH < 5$) and mineral precipitation took place at temperatures ~240 °C (Murowchick and Barnes, 1986; Murowchick, 1992). Marcasite is also commonly documented to occur at other Carlin-type deposits such as Carlin (Kuehn and Rose, 1992), Betze-Post (Arehart et al., 1993b; Bettles and Lauha, 1989), and Getchell (Cline et al., 1993). Furthermore, Alunite and kaolinite in argillic alteration assemblage are produced by acidic to slightly acidic oxidizing fluids as well. The oxidation of H_2S vapor by boiling and/or mixing with oxygenated groundwaters would produce sulfuric acid (H_2SO_4) causing the formation of these acid alteration minerals (Romberger, 1985). At the Lone Tree deposit, the higher K_2O content at the hydrothermally altered areas than those at unaltered host rocks reflect the formation of acid alteration minerals (Bloomstein et al., 1993). Similarly, according to Radtke (1980) the most notable change in altered host rocks at the Carlin mine is the increase in K_2O components over to that in unaltered original rocks. The acid fluids would account for the extensive carbonate removal from the calcareous rock units at the Lone Tree deposit, an important process in the preparation of the host rocks for subsequent gold mineralization.

Mineralization processes and genetic model

In the development of genetic models for the formation of Carlin-type, as well as other various types of gold deposits, it is crucial to understand the transport and deposition of gold. Transportation of gold in hydrothermal systems requires oxidation of gold to an ionic species (Au^+) to allow complexing with other ions (e.g., Cl^- and HS^-) (Rytuba, 1985). The dominant complex in near neutral to slightly alkaline conditions is $Au(HS)^-_2$, while in acidic conditions (pH=~5.5) with reduced sulfur HS^- or H_2S, $HAu(HS)^\circ_2$ is the dominant complex (Seward, 1973; Hayasi and Ohmoto, 1991; Shenberger and Barnes, 1988). The complex $AuCl^-_2$ is important under acidic (low pH), oxidizing (high

fO_2), and high-temperature conditions in the presence of high concentrations of Cl^- (Romberger 1985; Henley, 1973; Rytuba, 1985). Another possibility suggested by Seward (1973) is that arsenothio complexes, $Au(AsS_2)^\circ$ and $Au(AsS_3)^-_2$, may be important in gold transport considering the close geochemical association of arsenic with gold. However, mutual solubility studies of orpiment and gold by Rytuba (1977) showed that arsenothio complexes are not important in gold transport.

Any changes in the above fluid chemistry and temperature would result in the precipitation of gold from the solution. If gold is transported as a chloride complex, deposition of gold would occur in response to a decrease in temperature, increase in pH, and change in oxidation state. In contrast, if gold is transported as a bisulfide complex, then gold deposition would occur in response to a decrease in temperature, decrease in H_2S, increase in oxidation potential, or change in pH.

In light of fluid compositions for stage 2 mineralization, determined from fluid inclusions and gas compositions, the three most likely fluid sources are magmatic, crustal, and evolved meteoric waters. The gold may be derived partly from magmatic processes and partly leached from sedimentary rocks as a result of fluid-rock interaction. High fluid temperatures, salinities, and high levels of CO_2 suggest that gold may have been carried as a chloride complex during the earlier stages of hydrothermal activity. As suggested by Henley (1973) bisulfide complex $Au(HS)^-_2$ may have been predominant at lower temperatures. The high H_2S/Ar ratio for fluid inclusions with and without halite crystals in stage 2 quartz (Fig. 23) supports that some gold may be transported as bisulfide complex. The low H_2S/Ar ratio in stage 1 quartz containing halite crystals suggest that sulfur in stage 2 quartz is obtained from sedimentary rocks during the migration of magmatic waters. In addition, high CH_4 content of pyrite in stage 2 mineralization supports sedimentary source for H_2S (Fig. 28C). CO_2 loss from the boiling magmatic water (Fig. 23) and the removal of carbonate from the host rocks shift pH towards slightly alkaline conditions leading to the precipitation of some free gold with quartz. The remaining fluids had enough H_2S concentrations to keep some gold in solution as bisulfide complex. The solubility calculations for gold in fluids with salinities of ~35 and ~5 eq. wt. % NaCl, containing 0.02 mole% H_2S (crush # 5058 b), indicate that these fluids can transport 14 ppb and 3.1 ppb gold, respectively, as a bisulfide complex at 270 °C (Table 12). The rising CO_2 condensate heated ground waters to boiling and initiated convection. After complete partition of H_2S to vapor phase, H_2S is oxidized to H_2SO_4 condensate by oxidation upon encountering the circulating groundwaters. The acid fluids (H_2SO_4) reacted with host rock and produced argillic alteration minerals. Gold is precipitated with pyrite-marcasite-and arsenopyrite at acidic oxidizing conditions at temperatures from 270-240 °C as indicated by fluid inclusions and the stability of hypogene marcasite. The mechanisms for gold precipitation were destabilization of bisulfide complex due to the H_2S loss by boiling and to sulfide minerals precipitation, and the rapid decrease in temperature as a result of fluid boiling and mixing. The depletion of H_2S concentrations in fluids as a result of pyrite-marcasite-arsenopyrite precipitation is very clearly illustrated in figure 28E. On the other hand, sulfidization of iron in the host rocks may have been a partial cause for the destabilization of bisulfide complex leading to gold precipitation as suggested for Jerrit Canyon deposit (Hofstra et al., 1991). The precipitation of base metal minerals (e.g. sphalerite and chalcopyrite) were latest due to their low concentrations in solution.

Block faulting and erosion enabled unevolved oxidizing ground waters to circulate through the upper parts of the ore body causing supergene oxidation. The supergene oxidation produced minerals such as hematite, goethite, covellite, and chalcocite from acidic waters generated by disintegration of pyrite. A simplified schematic diagram is illustrated to account for the formation of the Lone Tree gold deposit (Fig. 29). This genetic model could equally serve for the other Carlin-type gold deposits as well.

Because these deposits are commonly associated spatially with intrusive rocks in the form of dike or stock that can contribute partial magmatic fluids and/or heat required for the convection of meteoric ground waters. Extensive interaction of ground waters with sedimentary rocks can produce geochemically evolved meteoric waters which are indicated to be responsible for the mineralization at the Carlin (Radtke, 1980), Cortez (Rye, 1985), Alligator ridge (Ilchik, 1990), and Jerrit Canyon (Hofstra et al., 1987; Hofstra et al., 1991). As it is shown in this study, evolved meteoric waters are also one of the ore fluids present at the time of gold mineralization at the Lone Tree deposit.

Table 12. The solubility of gold in high and low salinity fluids containing 0.02 mole % H_2S at temperatures from 270 to 240 °C.

	Salinity: 35 eq. wt. % NaCl			**Salinity: 5 eq. wt. % NaCl**		
Temp. (C)	AuCl$^-$2 (ppb)	Au(HS)$^-$2 (ppb)	Total (ppb)	AuCl$^-$2 (ppb)	Au(HS)$^-$2 (ppb)	Total (ppb)
270	0.1	14.0	14.1	0.0	3.1	3.1
265	0.1	5.0	5.2	0.0	1.1	1.1
260	0.1	3.2	3.3	0.0	0.7	0.7
255	0.1	2.1	2.2	0.0	0.5	0.5
250	0.1	1.5	1.6	0.0	0.4	0.4
245	0.0	1.1	1.1	0.0	0.3	0.3
240	0.0	0.9	0.9	0.0	0.2	0.2

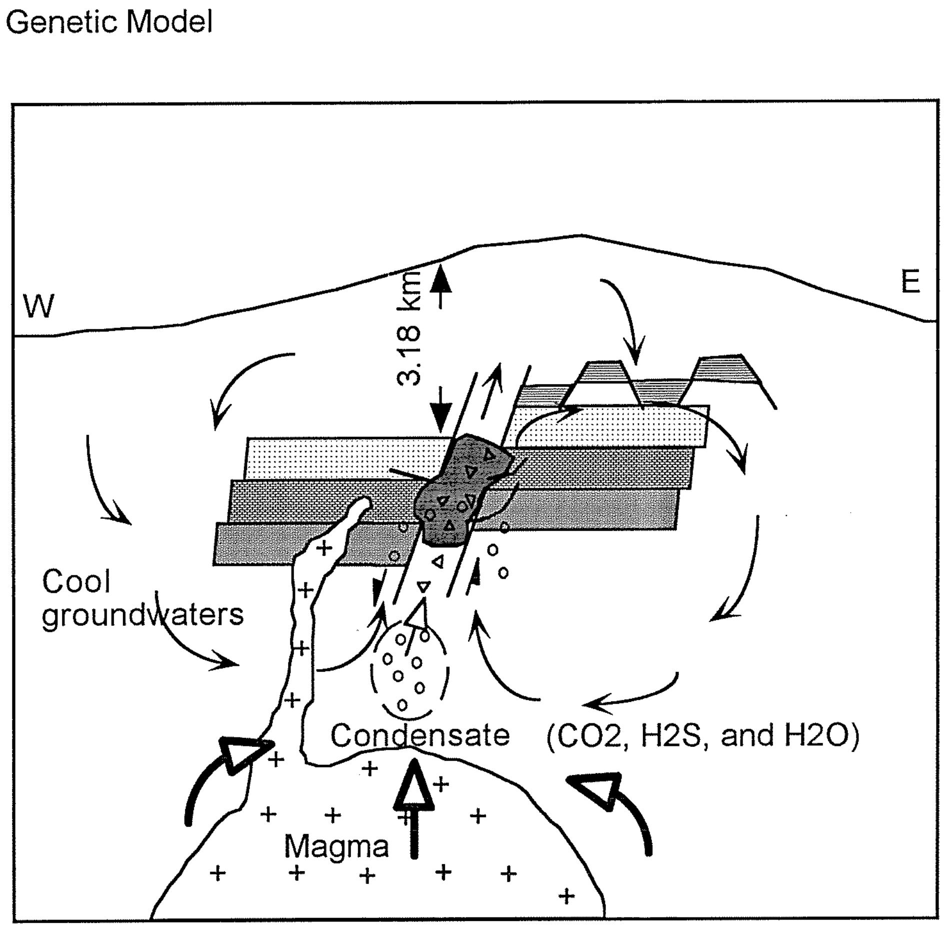

Figure 29. A simplified genetic model for the formation of the Lone Tree gold deposit.

Pressure and temperature changes

The wide range of temperature (185-411 °C) and salinities (1.23-41.4 eq. wt. % NaCl) recorded by fluid inclusions in stage 2 quartz can be explained by fluid boiling and fluid mixing from multiple sources. Gas compositions of fluid inclusions reveal that multiple fluids (meteoric, magmatic, and crustal) were present at the time of mineralization (Fig. 28C). Mixing of fluids from different sources should produce a fluid with salinity and temperature characteristics between those of the original fluids. The increasing trend of salinity with temperature displayed by the first group of fluid inclusions, that are described earlier, can result from mixing of magmatic and meteoric waters (Fig. 22A). The variations in temperature can also be explained by fluid boiling as the evidence of boiling is indicated in type d and g inclusions. Because intermittent boiling results in a decrease in temperature.

The variations in salinity and temperature suggest that pressure was probably fluctuating during the time of mineralization. The mode of homogenization displayed by halite-bearing fluid inclusions can reflect P-T conditions. The homogenization of halite-bearing fluid inclusions can occur as one of the following three modes: halite dissolution; vapor bubble disappearance; simultaneous disappearance of halite and vapor. Fluid inclusions displaying two or all three modes of homogenization indicate that either pressure at relatively constant temperature or temperature at relatively stable pressure were changing (Bodnar, 1994). Cline and Bodnar (1993) propose pressure change model to account for the different modes of homogenization of inclusions in Questa, porphyry molybdenum deposit. The homogenization of halite-bearing fluid inclusions in stage 2 quartz in two modes as halite dissolution and vapor bubble disappearance suggests that pressure and temperature were changing during the ore formation at the Lone Tree deposit. A common explanation for the origin of halite-bearing fluid inclusions that homogenize by halite dissolution is trapment of halite-saturated solutions at elevated temperatures and pressures. Fluid inclusions trapping halite undersaturated fluids between liquidus and the isochore defining simultaneous disappearance of halite and vapor homogenize by halite dissolution as well (Bodnar, 1994).

Microthermometric and gas analyses data enable the estimate of various pressure figures to constrain the pressure during gold mineralization. The maximum pressure is determined to be 401 bars for boiling low salinity fluids. The minimum pressure is calculated as 500 bars for halite-bearing fluid inclusions. Total vapor pressure of gas phases in boiling low-salinity fluids is 228 bars. The total vapor pressure obtained from boiling fluids indicate that boiling took place at depths of 3180 meters. Altogether pressure figures constrain a pressure range from 173 to 401 bars for low salinity fluids and a minimum pressure of 500 bars for high salinity fluids. The highest reasonable pressure may have been upper 500 bars. Therefore it is suggested that pressure fluctuated between 173 and upper 500 bars. This range of pressure in general agrees with those at different type of gold deposit with similar fluid characteristics and at other Carlin-type gold deposits. Richards and Kerrich (1993) determines a pressure of ~450 bars for halite saturated fluids at temperatures of 200-210 °C in the Porgera gold mine, Papua New Guinea. Kuehn and Rose (1995) calculates a pressure range of 400-1200 bars for deep CO_2-rich fluids in the Carlin mine.

Timing of gold mineralization

Fluid inclusion microthermometry and gas analyses results suggest a partial magmatic input to second stage mineralizing fluids and a meteoric origin for the third stage mineralizing fluids. A porphyritic granodiorite dike outcrops at the south end of the Lone Tree hill. K-Ar age dating on biotite and hornblende from the dike indicates 36 to 39 Ma (Bloomstein et al., 1993). The geochemical data along with the spatial association of the intrusive dike suggest that mineralization may be genetically related to the dike. If that is the case then the age of the second stage mineralization is most likely early Oligocene. Igneous rocks of this age spatially associated with other Carlin-type gold and gold-skarn deposits are widespread in the Battle Mountain-Eureka mineral belt (Cortez trend) (Maher et al., 1993). The timing of the mineralization at the Cortez deposit is not directly determined but it is inferred to be 34 Ma on the basis of K-Ar date obtained from the closely associated quartz porphyry dike (Wells et al., 1971). Furthermore, mineral deposits in the Tuscarora district such as Jerrit Canyon are related to the 38 Ma volcanic rocks (Cox et al., 1991). Fortitute gold-skarn deposit in the Copper Canyon mining area near Battle Mountain is related to the 38.5 Ma granodiorite porphyry stock (Myers and Meinert, 1991). Similarly, McCoy and Cove deposits are genetically associated with 39.7 Ma quartz monzonite-granodiorite porphyry (Kuyper,1988).

^{40}Ar/^{39}Ar

Analytical implications

In order to obtain a precise apparent age for any sample there must be sufficient K and radiogenic argon. The attempt of dating barite with the ^{40}Ar/^{39}Ar method met with limited success due to the general lack of both of these components. In many cases, the large error in ages was directly related to the analytical measurement error of ^{39}Ar which was high due to very small signal sizes (Table 9 and 10). The relationship between the error in age and the radiogenic yield error is two-fold. For instance, when a sample is highly radiogenic, the $^{40}Ar/^{36}Ar$ ratio may have a very high error due to very low concentrations of ^{36}Ar, but this high measurement error does not propagate into a large error in the age because the correction for atmospheric argon is negligible. On the other hand, when a sample has low a radiogenic yield, the ^{36}Ar measurement error is generally quite small due to high concentrations of ^{36}Ar, but since the atmospheric correction is large, even small errors in the measured $^{40}Ar/^{36}Ar$ ratio propagate into large errors in the age. The most detrimental case towards dating a sample is when the $^{40}Ar/^{36}Ar$ argon ratio is low and the signal sizes for both isotopes are small.

For many of the barites dated in this study, it is the combination of low radiogenic yield and lack of sufficient ^{39}Ar which inhibits precise age determinations. The analytical error associated with small ^{39}Ar signal could be decreased by increasing the irradiation times, and larger samples. Increasing the sample size may not be as effective as increasing the irradiation time towards producing more ^{39}Ar signal. This is born out by the poor gas clean-up associated with the ~100 mg furnace runs, as even with extended gettering times (~30 minutes) the sample gas was not always pure. Increased irradiation (J-factors to about 0.008) for samples such as Lakes, Rain, Buchans, and Hansonburg would significantly reduce (by about 1/2) the overall age uncertainty. For samples like Lone Tree and Getchell, an increased ^{39}Ar signal would not help because there is essentially no detectable ^{40}Ar*.

A measured ^{40}Ar/^{36}Ar ratio greater than 295.5 (^{40}Ar/^{36}Ar ratio for the atmospheric argon) indicates either in situ produced radiogenic argon or excess argon. For laser analyses from the Lone Tree, Getchell, Hansonburg, and Bredehorn barites there is essentially no ^{40}Ar/^{36}Ar greater than air. This is shown in Figure 27 where total ^{40}Ar is plotted versus ^{40}Ar/^{36}Ar ratio for each step with 2σ error bars. Figure 27 shows that most of the total atmospheric ^{40}Ar can be removed during the first low temperature step. This behavior would be advantageous for dating barite which contain K as potentially the atmospheric argon could be separated from any radiogenic argon.

These analyses revealed that barite does not contain an excessive concentration of total ^{40}Ar (Table 9) relative to other commonly dated minerals. McDougall and Harrison (1988) show that micas and hornblendes contain on the order of 2-8x10^{-14} moles/mg of atmospheric argon which is very similar to the barites analyzed in this study. The Bredehorn barite does however contain relatively high concentrations of atmospheric ^{40}Ar (~1-2x10^{-13} moles/mg) thus making it not suitable for dating, even if it contained some K.

The analyses also show that excess argon is not a common occurrence in barite. For all of the samples with very low K, the $^{40}Ar/^{36}Ar$ values were essentially atmospheric (Table 9). The combination of relatively low concentrations of atmospheric argon and no evidence for excess argon would make barite suitable for dating in the cases where some K was present.

Another positive aspect of barite is their low Ca concentrations. This makes the interference from Ca produced argon isotopes negligible. The relatively high ^{37}Ar signal ($2.3x10^{-16}$) for only one barite sample from the Getchell is most probably a result of minute calcite inclusions.

The laser analyses of the Lakes, Rain, and Buchans barite yielded measurable radiogenic argon and ^{39}Ar. The ^{39}Ar signals are still small and could be improved by increased irradiation durations, but the signals that are greater than $1x10^{-16}$ moles are measurable to about 0.5 to 1%. These samples also had radiogenic yields ranging from about 10 to 30% and overall relatively low uncertainties. These results indicate that in some instances, K can be incorporated into barite and $^{40}Ar/^{39}Ar$ analyses can yield apparent ages with high enough precision to allow for geologic considerations of the age data.

The extreme difference in K concentrations between laser and furnace analyses coupled with the low furnace concentrations (Table 11) may indicate that the ^{39}Ar signal in furnace analyses is depressed by the partial pressures of accompanying reactive gases.

Geologic implications

Synsedimentary Lakes barite deposit is hosted in Ordovician Vinini Formation (LaPointe et al., 1991). The barite occurs as beds conformable to the bedding of enclosing sedimentary rocks, indicating a contemporaneous deposition of barite and sedimentary units (LaPointe et al., 1991). The barite yields an age of ~180 Ma (Fig. C-1) which is considerably younger than its stratigraphic age. Young ages may be explained by a partial argon loss caused by a thermal event. Tertiary volcanic rocks as described by LaPointe et al. (1991), that overlie the deposit, did not cause any argon loss. Hence, the reason for the young ages may only be the low radiogenic argon concentrations generated from the limited amounts of potassium. Therefore, the age obtained from barite does not have any geologic implication.

Even though radiometric age of the Rain deposit has not been determined yet, Knutsen and West (1984) infer a genetic tie with a spatially associated Tertiary intrusive stock. One step of the age spectrum from the barite yields an age of 414±27 Ma (Fig. C-1) which is highly inconsistent with the known intrusive activities in the north central Nevada. The oldest intrusive metallogenic episode took place in the Jurassic period (Roberts et al., 1971). Such an old date from barite could be a result of either ^{39}Ar recoil loss or sample contamination (i.e. xenocryst). The barite hand sample from the Rain deposit was very fine grained and massive. ^{39}Ar loss due to recoil during the irradiation is very well known phenomenon for fine grained minerals (Smith et al., 1993). Since there is no information on argon systematics of barite, recoil may or may not be a problem for barite. Then, barite contaminated by other minerals in the form of a xenocryst from the Paleozoic host rocks would account best for the old age.

The Buchans deposit is a Kuroko type volcanogenic massive sulfide deposit, which is hosted in Ordovician felsic volcanic sequences and formed by interactions between volcanic hydrothermal fluids, wall rocks, and sea water on the sea floor (Clarke and Poole, 1989; Thurlow et al., 1975). A precise apparent age 23.6±1.8 Ma obtained from the final step of age spectrum from this barite (Fig. C-1) is significantly younger than the age of its genetically related host rocks. The reason for this young age is insufficient radiogenic argon. Two possible explanations for radiogenic argon loss could be: 1) a thermal disturbance approximately 24 Ma years ago, and 2) barite is not retentive for argon. Since there is no reported intrusive rocks of Tertiary age in the vicinity of deposit as a possible source of heat to reset age, unretentivity of barite for argon would account best for argon loss and thus for a considerably young age.

CONCLUSIONS

A genetic model has been developed for the Lone Tree gold deposit through studies of mineral paragenesis, fluid inclusion microthermometry, fluid inclusion gas analyses, and $^{40}Ar/^{39}Ar$ geochronology. This model could equally serve for the other Carlin-type gold deposits as well. The following conclusions are reached from this research in accomplishing the above objective.

1) Gold mineralization at the Lone Tree deposit is primarily confined to fault zones and fracture sets, where sedimentary host rocks experienced decarbonatization, silicification (by repeated introduction of hydrothermal silica), and argillization (by development of clay minerals especially hypogene kaolinite).

2) Four stages of mineralization have been identified at the Lone Tree deposit. The first stage of mineralization is represented by brecciated quartz and minor pyrite. The second stage, main gold sulfide mineralization containing quartz veins, kaolinite, pyrite, marcasite, arsenopyrite, gold, sphalerite, and chalcopyrite is overprinted by a third stage of mineralization comprising barite, pyrite, and gold. Free gold grains occur in quartz and clay mineral assemblage in association with pyrite in stage 2 mineralization. The

fourth stage is supergene mineralization and includes covellite, chalcocite, native copper, hematite, and goethite.

3) Fluid inclusion and gas composition data indicate multiple sources for the main gold stage mineralizing fluids as magmatic, crustal, and evolved meteoric waters. Fluid inclusion data indicates fluids had temperatures of 185 to 411 °C and salinity of 1.23 to 41.4 eq. wt. % NaCl. High salinity fluids (28.6-41.4 eq. wt. % NaCl) along with high N_2/Ar ratios and high CO_2 concentrations demonstrate a magmatic input. The occurrence of similar fluid type with much higher N_2 composition in stage 1 brecciated quartz indicates a magmatic input for this stage of mineralization as well. Low to moderate salinity fluids (1.23-8.14 eq. wt. % NaCl) indicate an evolved meteoric water formed by water-rock interaction and/or fluid mixing. The evolved meteoric fluids appear to be partially and/or completely responsible for the gold mineralization at Carlin-type deposits. N_2-CH_4-Ar*100 ternary plot indicates mostly crustal fluid origin for pyrite and perhaps for some gold in stage 2 mineralization.

4) Fluid inclusions in barite from stage 3 mineralization have a salinity of 1.23 to 1.74 eq. wt. % NaCl and

temperatures of 103 to 174 °C. The low salinity and temperature nature of fluids suggest unevolved meteoric water origin. Gas composition of pyrite coating barite also shows unevolved meteoric water origin on N_2-He-Ar ternary plot.

5) Fluids responsible for main stage gold mineralization were boiling as evident from coexisting vapor-rich and liquid-rich inclusions. Ternary plots for gases N_2-CH_4-CO_2, N_2-C_nH_n-CO_2, and CO_2-CH_4-H_2S can reveal boiling trends. The calculations for partition of gases such as CO_2, CH_4, and H_2S in a model boiling produced similar trends to those in ternaries. High gas concentrations can also verify if fluids were boiling. On the other hand, fluids in stage 3 mineralization were not boiling.

6) Marcasite in main gold sulfide mineralization and the clay minerals produced by the argillic alteration such as hypogene kaolinite indicate that mineralizing fluids were acidic.

7) Halite-bearing fluid inclusions were trapped under minimum pressures of 500 bars. Vapor pressures of gaseous phases indicate that fluid boiling leading to mineralization took place at pressures of 228 bars

corresponding to a depth of 3180 meters.

8) Gold may have been transported by both chloride and bisulfide complexes. The gold precipitation occurred as a result of H_2S loss, a decrease in temperature due to fluid boiling and mixing, pyrite precipitation, and sulfidization of wall rocks.

9) Age dating of barite with $^{40}Ar/^{39}Ar$ method was of a limited success due to the low radiogenic argon yield and lack of sufficient potassium. However, in some cases potassium can be incorporated into barite and $^{40}Ar/^{39}Ar$ analyses can produce apparent ages with high enough precision to allow for geologic considerations of the age results.

REFERENCES

Ahmad, S. N., and Rose, A. W., 1980, Fluid inclusions in porphyry and skarn ore at Santa Rita, New Mexico: Economic Geology, v. 75, p. 229-250.

Arehart, G. B., Kesler, S. E., O'Neil, J.R., and Foland, K. A., 1992, Evidence for the supergene origin of alunite in sediment-hosted micron gold deposits, Nevada: Economic Geology, v. 87, p. 263-270.

Arehart, G. B., Eldrige, C. S., Chryssoulis, S. L., and Kesler, S. E., 1993b, Ion microprobe determination of sulfur isotope variation in iron sulfides from the Post/Betze sediment-hosted disseminated gold deposit, Nevada, USA: Geochimica et Cosmochimica Acta, v. 57, p. 1505-1519.

Arehart, G. B., Foland, K. A., Naeser, C. W., and Kesler, S. E., 1993c, $^{40}Ar/^{39}Ar$, K/Ar and fission track geochronology of sediment-hosted disseminated gold deposits at Post-Betze, Carlin trend, north eastern Nevada: Economic Geology, v. 88, p. 622-646.

Bagby, W. C., and Berger, B. R., 1985, Geologic characteristics of sediment-hosted disseminated precious-metal deposits in the western United States: Reviews in Economic Geology, v. 2, p. 160-202.

Bakken, B. M., Hochella, M. F., Jr., Marshall, A. F., and Turner, A. M., 1989, High-resolution microscopy of gold in unoxidized ore from the Carlin mine, Nevada: Economic Geology, v. 84, p. 171-180.

Barbieri, M., 1989, Geochemistry of barium, in Brodtkorb, M. K., ed., Nonmetalliferous stratabound ore fields: Van Nostrand Reinhold, New York, p. 9-17.

Bettles, K. H., and Lauha, E. A., 1991, Gold deposits of the Goldstrike mine, Carlin trend, Nevada: World Gold' 91, p. 251-257.

Bloomstein, E., Braginton, B., Owen, R., Parratt, R., Raabe, K., and Thompson, W., 1993, Geology and Geochemistry of the Lone Tree gold deposit, Humboldt County, Nevada: Preeprint no: 93-205, Society of Mining, Metallurgy, and Exploration, Littleton, Co., 23p.

Bodnar, R. J., 1993, Revised equation and table for determining the freezing point depression of H2O-NaCl solutions: Geochimica et Cosmochimica Acta, v., 57, p. 683-684.

Bodnar, R. J., 1994, Synthetic fluid inclusions: XII. The system H2O-NaCl. Experimental determination of the halite liquidus and isochores for a 40 wt % NaCl solution: Geochimica et Cosmochimica Acta, v. 58, p. 1053-1063.

Brown, P. E., 1989, FLINCOR: A microcomputer program for the reduction and investigation of fluid-inclusion data: American Mineralogist, v. 74, p. 1390-1393.

Brueckner, H. K., and Snyder, W. S., 1985, Structure of the Havallah sequence, Golconda allochthon, Nevada; Evidence for prolonged evolution in an accretionary prism: Geological Society of America Bull., v. 96, p. 1113-1130.

Christensen, O. D., 1993, Carlin trend geologic overview, in Christensen, O. D., ed., Gold deposits of the Carlin trend, Nevada: Economic geology Guidebook series v. 18, p. 12-27.

Clarke, S. H. B., and Poole, F. G., 1989, Starabound barite ore fields of North America (excluding Arkansas), in Brodtkorb, M. K., ed., Nonmetalliferous stratabound ore fields: Van Nostrand Reinhold, New York, p. 93-117.

Cline, J. S., Hofstra, A. H., and Landis, G. P., 1993, Mineral paragenesis and P-T-X of ore fluids at the Getchell Carlin-type gold deposit, Nevada: Geological Society of America Abstracts with Programs, v. 25, p. 21.

Cline, J. S., and Bodnar, R. J., 1994, Direct evolution of brine from a crystallizing silicic melt at the Questa, New Mexico, molybdenum deposit: Economic Geology, v. 89, p. 1780-1802.

Cox, D. P., Ludington, S., Sherlock, M. G., Singer, D. A., Berger, B. R., and Tingley, J. V., 1991, Mineralization patterns in time and space in the Great Basin of Nevada, in Raines, G. L., Lisle, R. E., Schafer, R. W., and Wilkinson, W. H., eds., Geology and ore deposits of the Great Basin, Symposium Proceedings: Reno, Geol. Soc. Nevada, p. 193-198.

Craig, J. R., and Vaughan, D. J., 1981, Ore microscopy and ore petrography, John Wiley and Sons, 406p.

Erickson, R. L., Silberman, M. L., and Marsh, S. P., 1978, Age and composition of igneous rocks, Edna Mountain quadrangle, Humboldt County, Nevada: Journal of Research U.S. Geol. Survey, v. 6, no: 6, p. 727-743.

Faure, G., 1986, Principles of isotope geology, 2nd edition, John Wiley & Sons, p. 93-111.

Giggenbach, W. F., 1980, Geothermal gas equilibria: Geochimica et Cosmochimica Acta, v. 44, p. 2021-2032.

Haas, J. L., 1976, Thermodynamic properties of the coexisting phases and thermochemical properties of the NaCl component in boiling NaCl solutions: U.S. Geol. Survey Bull. no: 1421-B, p. B1-B71.

Hayasi, K., and Ohmoto, H., 1991, Solubility of gold in NaCl-and H_2S-bearing aqueous solutions at 250-350 °C: Geochimica et Cosmochimica Acta, v. 55, p. 2111-2126.

Henley, R. W., 1973, Solubility of gold in hydrothermal chloride solutions: Chemical Geology, v. 11, p. 73-87.

Henley, R. W., 1984, Gaseous components in geothermal processes, in, Robertson, J. M., ed., Fluid-Mineral equilibria in hydrothermal systems: Reviews in Economic Geology, v. 1, p. 45-55.

Hofstra, A. H., Landis, G. P., and Rowe, W. A., 1987, Sediment hosted disseminated gold mineralization at the Jerrit Canyon, Nevada: IV - Fluid geochemistry: Geological Society of America Abstracts with Programs, v. 19, p. 704.

Hofstra, A. H., Levethal, J. S., Worthrop, H. R., Landis, G. P., Rye, R. O., Birak, D. H., and Dahl, A. R., 1991, Genesis of sediment-hosted gold deposits by fluid mixing and sulfidation: Chemical reaction path modeling of ore deposition process documented in the Jerrit Canyon district, Nevada: Geology, v. 19, p. 36-40.

Ilchik, R. P., 1990, Geology and geochemistry of the Vantage gold deposits, Alligator Ridge-Bald Mountain mining district, Nevada: Economic Geology, v. 85, p. 50-75.

Knutsen, G. C., and West, P.W., 1984, Geology of Rain disseminated gold deposit, Elko County, Nevada, in Wilkins, J. Jr., ed., Gold and silver deposits of the Basin and Range province, western U.S.A.: Arizona Geological Society Digest, v. XV, p. 73-76.

Kuehn, C. A., 1989, Studies of disseminated gold deposits near Carlin, Nevada: Evidence for a deep geologic setting of ore formation: Unpub. Ph. D. thesis, Pennsylvania State University, 395p.

Kuehn, C. A., and Rose, A. W., 1992, Geology and geochemistry of wall-rock alteration at the Carlin gold deposit, Nevada: Economic Geology, v.87, p. 1697-1721.

Kuehn, C. A., and Rose, A. W., 1995, Carlin gold deposits, Nevada: Origin in a deep zone of mixing between normally pressured and overpressured fluids: Economic Geology, v. 90, p. 17-36.

Kuyper, B. A., 1988, Geology of the McCoy gold deposit, Lander County, Nevada, in Schafer, R. W., Cooper, J. J., and Vikre, P. G., eds., Bulk mineable precious metal deposits of the western United States, Symposium Proceedings: Reno, Geol. Soc. Nevada, p. 173-185.

Landis, G. P., and Hofstra, A. H., 1991, Fluid inclusion gas chemistry as a potential minerals exploration tool: Case studies from Creede, Co, Jerrit Canyon, NV, Coeur d'Alene district, ID and MT, southern Alaska mesothermal veins, and mid-continent MVT's: Journal of Geochemical Exploration v. 42, p. 25-59.

LaPointe, D. D., Tingley, J. V., and Jones, R. B., 1991, Mineral resources of Elko County, Nevada: Nevada Bureau of Mines and Geology Bulletin 106, 236p.

Madrid, R. J., 1987, Stratigraphy of the Roberts Mountain allochthon in north-central Nevada: Unpub. Ph.D. thesis, Stanford University, 341p.

Maher, B. J., Browne, Q. J., and McKee, E. H., 1993, Constaints on the age of gold mineralization and metallogenesis in the Battle Mountain-Eureka mineral belt, Nevada: Economic Geology, v. 88, p. 469-478.

McDougall, I., and Harrison, T. M., 1988, Geochronology and thermochronology by the ^{40}Ar/^{39}Ar method, Oxford University Press, New York, 212p.

McIntosh, W. C., and Cather, S. M., 1994, ^{40}Ar/^{39}Ar geochronology of basaltic rocks and contsraints on late Cenozoic stratigraphy and landscape development in the Red Hill-Quemado area, New Mexico: New Mexico Geological Society Guidebook, 45th Field Conference, p. 209-224.

Miller E. L., Kanter. L. R., Larue, D. K., and Turner, R. J., 1982, Structural fabric of the Paleozoic Golconda Alochthon, Antler Peak quadrangle, Nevada: Progressive deformation of an oceanic sedimentary assemblage: Journal of Geophysical Research, v. 87, p. 3795-3804.

Murchey, B. L., 1990, Age and depositional setting of silicieous sediments in the upper Paleozoic Havallah sequence near Battle Mountain, Nevada: Implications for theee paleogeography and structural evolution of the western margin of North America, in Harwood, D., and Miller, M. M., ed., Paleozoic and early Mesozoic Paleogeographic relations; Sierra Nevada, Klamath Mountains and related terranes: Geol. Society of America Special Paper 225, p. 137-155.

Murowchick, J. B., and Barnes, H. L., 1986, Marcasite precipitation from hydrothermal solutions: Geochimica et Cosmochimica Acta, v. 50, p. 2615-2629.

Murowchick, J. B., 1992, Marcasite inversion and the petrographic determination of pyrite ancestry: Economic Geology, v. 87, p. 1141-1152.

Myers, G. L., and Meinert, D. L., 1991, Alteration, mineralization, and gold distribution in the Fortitude gold skarn, in Raines, G. L., Lisle, R. E., Schafer, R. W., and Wilkinson, W. H., eds., Geology and ore deposits of the Great Basin, Symposium Proceedings: Reno, Geol. Soc. Nevada, p. 407-417.

Norman, D. I., Ting, W., Putnam, B. R., and Smith, R. W., 1985, Mineralization of the Hansonburg Mississippi Valley-type deposit, New Mexico: Insight from composition of gases in fluid inclusions: Canadian Mineralogist, v. 23, p. 353-368.

Norman, D. I., and Musgrave, J. A., 1994, N_2-Ar-He composotions in fluid inclusions: Indicators of fluid source: Geochimica et Cosmochimica Acta, v. 58, p. 1119-1131.

Norman, D. I., Moore, J. N., Yonaka, B., and Musgrave J., 1996, Gaseous species in fluid inclusions: A tracer of fluids and indicator of fluid processes: Proceedings: Twenty-first workshop on geothermal reservoir engineering, p. 8.

Percival, T. J., and Radtke, A. S., 1994, Sedimentary-rock-hosted disseminated gold mineralization in the Alsar district, Macedonia: The Canadian Mineralogist, v. 32, p. 649-665.

Potter, R. W., Babcock, R. S., and Brown, D. L., 1977, A new method for determining the solubility of salts in aqueous solutions at elevated temperatures: Journal of Research U.S. Geol. Survey, v. 5, no: 3, p. 389-395.

Radtke, A. S., Rye, R. O., and Dickson, F. W., 1980, Geology and stable isotope studies of the Carlin gold deposit, Nevada: Economic Geology, v. 75, p. 641-672.

Reynolds, T. J., and Beane, R. E., 1985, Evolution of hydrothermal fluid characteristics at the Santa Rita, New Mexico, porphyry copper deposit: Economic Geology, v. 80, p. 1328-1347.

Richards, J. P., and Kerrich, R., 1993, The Porgera gold mine, Papua New Guinea: Magmatic hydrothermal to epithermal evolution of an alkalic-type precious metal deposit: Economic Geology, v. 88, p. 1017-1052.

Roberts, R. J., 1964, Stratigraphy and structure of the Antler Peak quadrangle, Humboldt and Lander Counties, Nevada: U.S. Geological Survey Professional Paper 459A, 93p.

Roberts R. J., Radtke, A. R., and Coats, R. R., 1971, Gold-bearing deposits in north-central Nevada and southwestern Idaho: with a section on periods of plutonism in north-central Nevada, M. L., Silberman, and E. H. McKee, Economic Geology, v. 66, p. 14-33.

Roedder, E., 1984, Fluid inclusions: Mineralogical Society of America, Reviews in Mineralogy, v. 12, 644p.

Romberger, S. B., 1985, Geochemistry of gold in hydrothermal deposits, in Shawe, D. R., and Ashley, R. P., eds., Introduction to geology and resources of gold, and geochemistry of gold: U.S. Geol. Survey Bull. 1857, p. A9-A25.

Romberger, S. B., 1986, Ore deposits; PS4, Disseminated gold deposits: Geoscience Canada v. 13, no:1, p. 23-31.

Rose, A. W., and Kuehn, C. A., 1987, Ore deposition from acidic CO_2-rich solutions at the Carlin gold deposits, Eureka County, Nevada: Geological Society of America Abstracts with Programs, v. 19, p. 824.

Rosler, H. J., and Lange, L., 1972, Geochemical tables: Elsevier Publishing Company, p. 112-118.

Rye. R. O., 1985, A model for the formation of carbonate-hosted disseminated gold deposits based on geologic, fluid-inclusion, geochemical, and stable-isotope studies of the Carlin and Cortez deposits, Nevada, in Tooker, E. W., ed., Geologic characteristics of sediment-and volcanic-hosted disseminated gold deposits; search for an occurrence model: U.S. Geol. Survey Bull., 1646, p. 35-42.

Rytuba, J. J., 1977, Mutual solubilities of pyrite, pyrrhotite, quartz and gold in aqueous NaCl solutions from 200° to 500 °C, and 500 to 1,500 bars and genesis of the Cortez gold deposit, Nevada: Unpub. Ph.D. thesis, Stanford University, 122p.

Rytuba, J. J., 1985, Geochemistry of hydrothermal transport and deposition of gold and sulfide minerals in Carlin-type gold deposits, in Tooker, E. W., ed., Geologic characteristics of sediment-and-volcanic-hosted disseminated gold deposits—search for an occurrence model: U.S. Geol. Survey Bull. 1646, p. 27-34.

Samson, S. D., and Alexander, E. C., 1987, Calibration of the interlaboratory 40Ar-39Ar dating standard; MMhb-1: Chemical Geology, v. 66, p. 27-34.

Seedorff, E., 1991, Magmatism, extension, and ore deposits of Eocene to Holocene age in the Great Basin-mutual effects and preliminary proposed genetic relationships, in Raines, G. L., Lisle, R. E., Schafer, R. W., and Wilkinson, W. H., ed., Geology and ore deposits of the Great Basin, Symposium Proceedings: Reno, Geol. Soc. Nevada, p. 133-178.

Seward, T. M., 1973, Thio complexes of gold and the transport of gold in hydrothermal ore solutions: Geochimica et Cosmochimica Acta, v. 37, p. 370-399.

Shawe, D. R., 1991, Structurally controlled gold trends imply large gold resources in Nevada, in Raines, G. L., Lisle, R. E., Schafer, R. W., and Wilkinson, W. H., eds., Geology and ore deposits of the Great Basin, Symposium Proceedings: Reno, Geol. Soc. Nevada, p. 199-212.

Shenberger, D. M., and Barnes, H. L., 1989, Solubility of gold in aqueous sulfide solutions from 150 to 350 °C: Geochimica et Cosmochimica Acta, v. 53, p. 269-278.

Shepherd, T. J., Bottrell, S. H., and Miller, M. F., 1991, Fluid inclusion volatiles as an exploration guide to black shale-hosted gold deposits, Dolgellau gold belt, North Wales, UK: Journal of Geochemical Exploration, v. 42, p. 5-24.

Silberling, N. J., 1975, Age relations of the Golconda thrust fault, Sonoma Range, north-central Nevada: Geological Society of America Special Paper 163, 28p.

Silberman, M. L., and McKee, E. H., 1971, K-Ar dates of granitic plutons in north-central Nevada: Isochron/West, no: 1, p. 15-32.

Sillitoe, R. H., and Bonham, J. F., Jr., 1990, Sediment-hosted gold deposits: Distal products of magmatic-hydrothermal systems: Geology, v. 18, p. 157-161.

Smith, P. E., Evensen, N. M., and York, D., 1993, First successful 40Ar-39Ar dating of glauconies: Argon recoil in single grains of cryptocrystalline material: Geology, v. 21, p. 41-44.

Speed, R. C., 1979, Collided Paleozoic platelet in the Western U.S.: Journal of Geology, v. 87, p. 279-292.

Speed, R. C., and Sleep, N. H., 1982, Antler orogeny and foreland basin: A model: Geological Society of America Bull., v.93, p. 815-828.

Theodore, T. G., 1991, Preliminary geologic map of the Valmy quadrangle, Humboldt County, Nevada: U.S. Geological Survey Open File Rept. 91-430, 10p.

Thurlow, J. G., Swanson, E. A., and Strong, D. F., 1975, Geology and lithogeochemistry of the Buchans polymetallic sulfide deposits, Newfoundland: Economic Geology, v. 70, p. 130-144.

Tooker, E. W., 1985, Disscussion of the disseminated -gold-ore-occurrence model, in Tokeer, E. W., ed., Geologic characteristics of sediment-and-volcanic-hosted disseminated gold deposits—search for an occurrence model: U.S. Geol. Survey Bull. 1646, p. 107-150.

Verville, G. J., and Sanderson, G. A., 1988, Early atokan fusulinids from the lower antler overlap sequence, Lander adn Humboldt Counties, Nevada: J. Paleontology v. 64, no: 4, p. 520-529.

Wells, J. D., Elliott, J. E., and Obradovich, J. D., 1971, Age of the igneous rocks associated with ore deposits, Cortez-Buckhorn area, Nevada: U.S. Geological Survey Professional Paper 750C, p. 127-135.

Wells, J. D., and Mullens, T. E., 1973, Gold-bearing arsenian-pyrite determined by microprobe analysis, Cortez and Carlin gold mines, Nevada: Economic Geology, v. 68, p. 187-201.

Wotruba, P. R., Benson, R. G., and Schmidt, K. W., 1988, Geology of the Fortitude gold-silver skarn deposits, Copper Canyon, Lander County, Nevada, in Schafer, R. W., Cooper, J. J., and Vikre, P. G., eds., Bulk mineable precious metal deposits of the western United States, Symposium Proceedings: Reno, Geol. Soc. Nevada, p. 159-171.

APPENDIX A
Fluid inclusion microthermometry data

	Th (C)	*Tm (C)*	*TsNaCl (C*	*Th(cor.)*	*Tm(cor.)*	*Ts(cor.)*	*F*	*Remarks*	*Salinity(eq.wt.%NaCl)*
quartz #12	266.8	-3.8		269.4	-3				4.96
	288.6	-3.7		291.4	-2.9				4.8
	292.6	-3.3		295.2	-2.5				4.18
	278.1	-4.9		280.7	-4.1				6.59
	264.2	-4.6		266.8	-3.8				6.16
	263.6	-4.7		266.2	-3.9				6.3
	249.8	-5		248.9	-3		0.9		4.96
	255.2	-3.9		254.4	-1.9		0.9		3.23
	261.8	-3.8		261.1	-1.8		0.92		3.06
	259.4	-4.1		258.7	-2.1		0.95		3.55
	276.4	-4		274.8	-2		0.9		3.39
	280.4	-4.8		278.6	-2.8		0.85		4.65
	261.5	-3.2		258.1	-2.8		0.92		4.65
	282.2	-3.6		276.8	-3.1		0.91		5.11
	263.4	-3.1		260	-2.7		0.92		4.49
	275	-2.9		270	-2.5		0.92		4.18
	283.7	-4.4		277.9	-3.9		0.9		6.3
	277.2	-3.9		272.2	-3.4		0.9		5.56
	259.2	-3.4		256	-3		0.95		4.96
	274.3	-3.6		264.9	-3.3		0.9		5.41
	285	-4.5		275	-4.2		0.9		6.74
	255	-2.8		246.2	-2.5		0.85		4.18
	265	-4.5		255.8	-4.2		0.9		6.74
	278.3	-3.5		268.7	-3.2		0.85		5.26
	256	-3.4		247.2	-3.1		0.95		5.11
	284	-3.2		274.2	-2.9		0.85		4.8
	291	-3.2		281	-2.9		0.9		4.8
	281	-3.1		271.2	-2.8		0.9		4.65
	278	-2.9		268.4	-2.6		0.95		4.34
	285	-3		275	-2.7		0.9		4.49
	276	-2.9		266.4	-2.6		0.9		4.34
	273	-2.8		263.6	-2.5		0.9		4.18
	283	-3		273.2	-2.7		0.9		4.49
	291	-3.3		281	-3		0.9		4.96
	288	-3.2		278	-2.9		0.95		4.8
	275	-3		265.6	-2.7		0.9		4.49
	252	-2.9		243.4	-2.6		0.92		4.34
	279	-3		269.4	-2.7		0.9		4.49
	277	-3.2		267.4	-2.9		0.92		4.8
	278	-3.3		268.4	-3		0.85		4.96
	238	-3.2		229.8	-2.9		0.9		4.8
	286	-3		276	-2.7		0.9		4.49
	279	-3.1		269.4	-2.8		0.9		4.65
	235	*-1.5*		*226.8*	*-1.2*		*0.9*	secon.?	2.07
	260	-3		251	-2.7		0.92		4.49
	292	-3.3		281.8	-3		0.85		4.96
	289	-3.1		279	-2.8		0.9		4.65
	286	-3.3		276	-3		0.9		4.96
	285	-3.2		275	-2.9		0.9		4.8
	286	-5		276	-4.6		0.9		7.31
	287	-5		277	-4.6		0.9		7.31
	286	-5		276	-4.6		0.9		7.31
	260	-1.1		253	-1		0.95		1.74
	267	-1.2		260	-1.1		0.95		1.91
	225	*-1.2*		*216.5*	*-1.1*		*0.95*	secon.?	*1.91*
	220	*-1.1*		*211.5*	*-1*		*0.95*	secon.?	*1.74*
	395	-2.8		383	-2.7		0.5		4.49
	260	-2.6		253	-2.5		0.85		4.18
	245	-1.3		237	-1.2		0.9		2.07
	278	-3.2		270	-3.1		0.1		5.11
	250	-1.2		243	-1.1		0.9		1.91
	246	-1.5		238.5	-1.4		0.9		2.41
	258	-1.4		251	-1.3		0.9		2.24
	253	-1.8		246	-1.7		0.9		2.9
	397	*-10.6*		389.8	*-10.5*		*0.6*		14.46
quartz #20	240	-3.6		232	-3.2		0.9		5.26
	255	-2.9		246.2	-2.6		0.85		4.34
	269	-2.8		259.8	-2.5		0.85		4.18
	279	-4.2		269.4	-3.8		0.85		6.16
	254	-2.6		245.2	-2.3		0.85		3.87

	Th (C)	*Tm (C)*	*TsNaCl (C)*	*Th(cor.)*	*Tm(cor.)*	*Ts(cor.)*	*F*	*Remarks*	*Salinity(eq.wt.%NaCl)*
	246	-4.1		237.4	-3.7		0.9		6.01
	259	-3		250	-2.7		0.9		4.49
	250	-3		241.4	-2.7		0.95		4.49
	245	-3.3		236.6	-3		0.9		4.96
	245	-2.7		236.6	-2.4		0.9		4.03
	247	-3.1		237	-2.8		0.9		4.65
	252	-3		243.3	-2.7		0.9		4.49
	263	-3.5		254	-3.1		0.9		5.11
	155	*-1.5*		*147*	*-1.2*		*0.95*	secon. ?	*2.07*
	143	*-1.3*		*136*	*-1*		*0.92*	secon. ?	*1.74*
	380	-2.4		373	-2.3		0.3		3.87
	410	-3.3		403	-3.2		0.4		5.26
qtz. #clt. 626	258	-3.3		249	-2.9		0.9		4.8
	278	-3.5		268.4	-3.1		0.9		5.11
	290	-4.4		281	-4		0.9		6 45
	280	-3.6		270	-3.2		0.9		5.26
	281	-3.2		271	-2.8		0.92		4.65
	268	-3.6		259	-3.2		0.85		5.26
	255	-4		246.2	-3.6		0.9		5.86
	289	-4.2		279.6	-3.8		0.9		6.16
	267	-3.7		257.8	-3.3		0.9		5.41
	285	-3.8		273	-3.4		0.85		5.56
	282	-4.1		272	-3.7		0.85		6.01
	262	-3.3		253	-2.9		0.9		4.96
	279	-3.4		269	-3.1		0.9		5.11
	148	*-1.1*		*140*	*-0.8*		*0.95*	secon.?	*1.4*
	152	*-1.4*		*144.6*	*-1.1*		*0.92*	secon.?	*1.74*
	272	-3.5		262.4	-3.1		0.9		5.11
	275	-4		266.8	-3.6		0.95		5.86
	269	-3.6		259.7	-3.2		0.85		5.26
	280	-3.1		270	-2.7		0.9		4.49
	365		270	342		254	0.5		34.9
	346		275	325		258	0.5		35.1
	325		290	304		272	0.5		36
	378		295	354		277	0.6		36.3
	350		300	328		282	0.3		36.7
	300		251	282		236	0.6		33.8
	302		223	284		209	0.8		32.3
	305		317	286		297	0.6		37.7
	320	-5.3		300	-5.2		0.75		8.14
	306	-5.1		288	-5.1		0.75		8
	337		192	316		179	0.8		30.9
	325		185	305		174	0.8		30.7
	298		180	280		168	0.8		30.4
	280		225	263		211	0.65		32.4
	276		220	259		206	0.6		32.2
	252		370	237		346	0.6		41.4
	246		252	231		237	0.6		33.9
	243		245	228		230	0.5		33.5
	210		215	196		201	0.5		31.9
	237		258	223		243	0.6		34.2
	285		260	268		245	0.65		34.3
	265		263	249		247	0.6		34.5
	375	-1.6		351	-1.5		0.1		2.57
	355	-1.8		332	-1.7		0.1		2.9
	318		347	299		326	0.6		39.8
	367		305	344		286	0.5		36.9
	352		300	329		282	0.6		36.7
	347		210	325		196	0.6		31.7
	312		161	293		152	0.4		29.8
	278		352	262		330	0.6	boiling	40.1
	435	-2.2		408	-2.1		0.2	boiling	3.55
quartz #10	305		240	298		232	0.85		33.6
	278	-3.5		271	-3.4		0.9		5.56
	310		321	303		314	0.7		38.9
	355	-1.2		332	-1.1		0.1		1.91
	355	-1.1		332	-1		0.1		1.74
	395	-0.8		369	-0.7		0.1		1.23
	415	-0.9		389	-0.8		0.1		1.4
	406	-8.4		380	-8.3		0.7		12.05
	335	-19.5		314	-19.4		0.9		21.96
	398	-1.7		372	-1.6		0.25		2.74
	408	-1.6		382	-1.5		0.25		2.57

	Th (C)	*Tm (C)*	*TsNaCl (C*	*Th(cor.)*	*Tm(cor.)*	*Ts(cor.)*	*F*	*Remarks*	*Salinity(eq.wt.%NaCl)*
	386		128	362		121	0.8		28.6
	370		132	346		125	0.7		28.7
	307		180	289		169	0.7		30.5
	320		170	300		159	0.7		30
	315		145	295		138	0.7		29.2
	325	-20		305	-19.9		0.7		22.31
	350	-21		328	-20.9		0.7		22.98
	343	-13.5		321	-13.4		0.8		17.26
	337	-14.2		316	-14.1		0.8		17.87
	325		173	304		162	0.8		30.2
	333		185	312		174	0.8		30.7
quartz #9	325		245	318		238	0.3		33.9
	195	-2.8		185.5	-2.7		0.9		4.49
	308		298	301		291	0.7		37.3
	394	-3.3		387	-3.2		0.3		5.26
	375	-2.5		368	-2.4		0.25		4.03
	405	-2.5		398	-2.4		0.3		4.03
	398	-2.4		391	-2.3		0.2		3.87
	315		235	308		227	0.8		33.3
	382	-19.8		375	-19.7		0.7		22.17
	341	-17.7		334	-17.6		0.65		20.67
	335	-11.3		328	-11.2		0.85		15.17
	343	-12.6		326	-12.5		0.8		16.43
	346		250	329		242	0.8		34.1
	330		223	323		214.5	0.8		32.6
	235	-1.8		227	-1.7		0.95		2.9
	338	-10.3		322	-10.2		0.85	boiling	14.15
	386	-1.9		379	-1.8		0.2	boiling	3.06
	410	-1.8		384	-1.4		0.2		2.41
	279		330	262		309	0.8		38.6
	436	-2.8		411	-2.4		0.2		4.03
	386	-2.7		361	-2.3		0.1		3.87
	308		323	289		302	0.5		38
quartz #1	260	-1.1		252.5	-1		0.8		1.74
	252	-1		244.5	-0.9		0.9		1.57
	243	-0.9		235.5	-0.8		0.95		1.4
	242	-0.9		234.5	-0.8		0.85		1.4
	240	-1		232.5	-0.9		0.9		1.57
	305		140	297		130	0.8		28.9
	259	-2.5		244	-2.4		0.85		4.03
	265	-2.6		249	-2.5		0.9		4.18
	380	-2.8		354	-2.7		0.35		4.49
	385	-2.7		360	-2.6		0.35		4.34
	383	-2.8		358	-2.7		0.3		4.49
	387	-2.8		362	-2.7		0.4		4.49
	388	-2.3		358	-2.2		0.4		3.71
	372	-1.9		348	-1.8		0.3		3.06
	346		275	326		259	0.75		35.2
	360		205	338		191	0.75		31.5
	320		335	301		314	0.8		38.9
	313		350	294		328	0.7		40
	413	-7.5		387	-7.4		0.7		10.98
	345		370	323		346	0.5		41.4
	380	-2.3		355	-2.2		0.15		3.71
	308	-3.5		289	-3.4		0.8		5.56
	375	-2.4		351	-2.3		0.35		3.87
	384	-2.2		360	-2.1		0.3		3.55
	284	-20.5		269	-20.4		0.9		22.65
Barite #23	135	-1.2		135.6	-0.9				1.57
	118	-1.1		118.4	-0.8				1.4
	126	-1.1		126.9	-0.8				1.4
	103	-1		103.1	-0.7				1.23
	112	-1.2		112.3	-0.9				1.57
	137	-1.3		137.9	-1				1.74
	123	-1.1		123.8	-0.8				1.4
	109	-1.1		109.3	-0.8				1.4
	276	-1.2		278	-0.9			necked?	1.57
	201	-1.2		202	-0.9			necked?	1.57
Barite #12	177	-1.1		169.8	-0.8		0.95		1.4
	146	-1.2		138.6	-0.9		0.95		1.57
	154	-1.1		146.6	-0.8		0.95		1.4
	135	-1.1		128	-0.8		0.95		1.4
	141	-1.2		134	-0.9		0.95		1.57
	186	-1.2		179	-0.9		0.95		1.57

	Th (C)	*Tm (C)*	*TsNaCl (C*	*Th(cor.)*	*Tm(cor.)*	*Ts(cor.)*	*F*	*Remarks*	*Salinity(eq.wt.%NaCl)*
	139	-1.1		133	-0.8		0.95		1.4
	172	-1.1		165	-0.8		0.95		1.4
Barite #6	132	-1.1		127	-0.8		0.92		1.4
	121	-1		117	-0.7		0.95		1.23
	134	-1.2		129	-0.9		0.95		1.57
	110	-1.1		108	-0.8		0.95		1.4
Barite #29	138	-1.1		131	-0.8		0.95		1.4
	131	-1.1		126	-0.8		0.95		1.4
	115	-1		113	-0.7		0.95		1.23
	125	-1		121	-0.7		0.95		1.23
	142	-1.2		136	-0.9		0.95		1.57
	127	-1.1		123	-0.9		0.95		1.57
Barite #33	129	-1		124	-0.7		0.95		1.23
	112	-1.1		109	-0.8		0.95		1.4
	132	-1		127	-0.7		0.95		1.23
Barite #L3		-1.1			-0.8		1		1.4
		-1			-0.7		1		1.23
	152	-1.2		144	-0.9		0.95		1.57
	128	-1.1		123	-0.8		0.95		1.4
	176	-1.1		168	-0.8		0.95		1.4
	159	-1		151	-0.7		0.95		1.23

APPENDIX B

Fluid inclusion gas analyses data

mineral	crush#	He	CH4	H2O	N2	H2S	Ar	CO2	CnHn	SO2
qtz #1	5057a	0	0.23422	96.80829	0.23139	0.01138	0.00384	2.65567	0.01686	0.00145
	5057b	0	0.20487	96.56109	0.16505	0.00822	0.00252	3.00807	0.0124	0.00082
	5057c	0	0.19023	95.46595	0.28235	0.00609	0.00223	4.01819	0.01015	0.00054
	5057d	0	0.19477	96.60339	0.13087	0.00598	0.00188	3.02667	0.00988	0.00073
	5057e	0	0.18172	96.33635	0.13331	0.00689	0.00181	3.30548	0.00935	0.00074
qtz #9	5058a	0	0.24711	96.4595	0.13299	0.01386	0.00337	3.10501	0.01043	0.00088
	5058b	0	0.25777	95.39818	0.27566	0.019117	0.00388	4.00702	0.01205	0.00078
	5058c	0	0.34039	94.97226	0.29109	0.01006	0.00232	4.35413	0.01129	0.00051
	5058d	0	0.37667	95.57398	0.73298	0.00735	0.00741	3.28386	0.00991	0.00038
	5058e	0	0.38393	96.53539	0.36411	0.00589	0.00224	2.68712	0.00843	0.00061
	5058f	0	0.26359	95.61015	0.24252	0.01188	0.00168	3.85553	0.00858	0.00042
	5058g	0	0.25409	97.30255	0.29008	0.00377	0.00201	2.13705	0.00593	0.00039
	5058h	0	0.43476	94.90472	0.6525	0.01117	0.00262	3.97005	0.01077	0.00056
qtz #20	5059a	0	0.34268	96.89117	0.32847	0.00226	0.00121	2.42436	0.00463	0.00041
	5059b	0	0.14074	98.23922	0.18245	0.00106	0.00075	1.43224	0.00233	0.00011
	5059d	0	0.28277	95.94249	0.16836	0.00997	0.00244	3.55723	0.00947	0.00102
	5059e	0	0.44854	95.92838	0.22271	0.00408	0.0014	3.37744	0.00731	0.00078
	5059h	0	0.64545	93.78558	0.50999	0.00664	0.00183	5.02817	0.01242	0.00057
qtz #12	5060a	0	0.11469	98.81749	0.19942	0.00403	0.00398	0.84477	0.00845	0.00035
	5060b	0	0.20424	98.2406	0.12103	0.00927	0.00421	1.37643	0.01442	0.00086
	5060c	0	0.21234	98.61897	0.1242	0.00682	0.00212	1.00648	0.01112	0.00047
	5060d	0	0.249	98.54461	0.1685	0.00448	0.0018	1.00141	0.00934	0.00046
	5060e	0	0.13589	98.79761	0.08244	0.00454	0.001	0.96485	0.00626	0.00023
	5060f	0	0.19538	98.01057	0.18131	0.00672	0.00139	1.58662	0.01045	0.00044
	5060h	0	0.2865	98.13472	0.12215	0.00583	0.00166	1.41283	0.01183	0.00079
qtz #10	5061a	0	0.30053	96.62299	0.21696	0.00587	0.00182	2.83387	0.00891	0.00059
	5061b	0	0.30572	96.03432	0.80429	0.00736	0.00515	2.80393	0.01345	0.00068
	5061c	0	0.27212	96.57024	0.16722	0.00564	0.002	2.95274	0.01038	0.00061
	5061d	0	0.27973	97.28995	0.11737	0.00758	0.00206	2.26581	0.00996	0.00076
	5061e	0	0.28926	97.1364	0.1371	0.00415	0.00171	2.39877	0.00978	0.00068
	5061f	0	0.31187	97.21015	0.12206	0.00544	0.00157	2.31799	0.00928	0.00071
qtz clt626	5062b	0	0.31524	97.85677	0.13414	0.00485	0.00206	1.66268	0.0078	0.00044
	5062c	0	0.30944	97.12357	0.18653	0.01027	0.00174	2.3511	0.01005	0.00052
	5062d	0	0.19159	98.58313	0.07893	0.0039	0.00159	1.10929	0.00608	0.00054
	5062e	0	0.25678	98.10508	0.10157	0.0052	0.00127	1.50766	0.00758	0.00052
	5062f	0	0.29842	97.03722	0.09924	0.00752	0.00151	2.53318	0.00796	0.00071
	5062g	0	0.20362	97.58829	0.0344	0.00904	0.00156	2.13246	0.00772	0.00069
	5062h	0	0.23446	97.51509	0.08133	0.00982	0.00151	2.12644	0.0083	0.00082
qtz #37a	5083a	0	0.36811	94.02815	1.36883	0.00317	0.00479	4.17518	0.02593	0.00114
	5083b	0	0.2018	94.89089	0.98213	0.00215	0.0031	3.87963	0.0172	0.00041
	5083c	0	0.18134	95.21296	0.69735	0.0012	0.00216	3.87647	0.01242	0.00036
	5083d	0	0.20326	95.07833	0.94893	0.00386	0.00343	3.71319	0.01721	0.00068
	5083e	0	0.15138	96.02743	0.33692	0.00418	0.00294	3.43147	0.0135	0.0009
qtz #37b	5085a	0	0.12964	98.26685	0.20764	0.00458	0.00294	1.3447	0.01021	0.00192
	5085b	0	0.17002	96.3711	0.52941	0.00199	0.00197	2.88184	0.01077	0.00078
	5085c	0	0.29708	94.7046	0.78961	0.00072	0.00151	4.1792	0.01534	0.00071
	5085d	0	0.31109	95.7803	0.70665	0.0005	0.00298	3.18118	0.01163	0.00061
	5085e	0	0.20222	95.83371	0.55253	0.00113	0.00159	3.3777	0.01096	0.00057
bar #10	5080a	0	0.11656	98.34644	1.29086	0.00095	0.00306	0.20596	0.01349	0.00021
	5080b	0	0.05992	98.84177	0.97804	0.00067	0.00186	0.0927	0.0083	8E-05
	5080c	0	0.11174	98.83779	0.9156	0.00072	0.00173	0.10378	0.00935	0.00012
bar #23	5081a	0	0.09734	98.8923	0.84457	0.001	0.00249	0.13242	0.00904	0.00025
	5081b	0	0.06913	99.03953	0.75326	0.0008	0.00215	0.11142	0.00668	0.00017
	5081c	0	0.10188	98.84631	0.87908	0.00171	0.00231	0.13222	0.00911	0.00046
	5081d	0	0.08742	99.02933	0.7107	0.00084	0.00186	0.14298	0.00691	0.00019
bar #29	5082a	0	0.03803	99.71965	0.19012	0.00017	0.0007	0.04503	0.00207	2E-05
	5082c	0	0.02933	99.59468	0.27552	0.00023	0.00127	0.09155	0.00259	0
	5082d	0	0.07165	99.3101	0.45032	0.00057	0.00158	0.14663	0.00467	9E-05
	5082e	0	0.06457	99.28036	0.46593	0.0006	0.00235	0.16515	0.00485	0.00079
bar #33	5043a	0	0.0808	99.505	0.27083	0.0011	0.0049	0.10459	0.00711	0.00023
	5043c	0	0.04568	99.62857	0.22343	0.00063	0.00384	0.08418	0.00103	7E-05
bar #12	5044d	0	0.07472	99.59734	0.1113	0.00946	0.00171	0.18246	0.00053	0.00025
pyr #27	5089a	0	5.59124	91.7271	0.44929	0.00063	0.00717	2.1725	0.04722	0.00026
	5089b	0	6.78976	90.58649	0.28708	0.0001	0.00189	2.28603	0.0424	0.00017
pyr #50	5090a	0	0.43507	97.585	0.09328	0.00453	0.00353	1.83626	0.01189	0.00094
	5090b	0	0.52988	97.75188	0.08943	0.00181	0.00166	1.59345	0.00875	0.00045
	5090c	0	0.64502	97.26894	0.02583	0.00275	0.0019	2.0178	0.00919	0.00078
	5090d	0	0.6837	97.48566	0.04932	0.00241	0.00197	1.74115	0.00887	0.00077

mineral	crush#	He	CH4	H2O	N2	H2S	Ar	CO2	CnHn	SO2
pyr #49	5091a	0	1.14181	98.13801	0.19284	0.00023	0.00259	0.5117	0.00964	0.00015
	5091b	0	1.6855	97.53857	0.22165	0.00022	0.00303	0.53393	0.01324	0.00011
pyr #28	**5086a**	**0**	**3.99371**	**85.05109**	**1.52086**	**0.00117**	**0.0094**	**9.37191**	**0.04627**	**0.00169**
	5086b	**0**	**3.36192**	**85.03129**	**1.40344**	**0.00072**	**0.00845**	**10.13995**	**0.04364**	**0.0009**
	5086c	**0**	**4.6073**	**82.93143**	**1.71401**	**0.00032**	**0.00675**	**10.6819**	**0.05244**	**0.00034**
pyr #28g	5087a	0	1.71389	88.36101	0.96375	0.00095	0.0053	8.91164	0.03396	0.0021
	5087b	0	1.87396	90.42329	0.68098	0.00048	0.00433	6.98447	0.02277	0.00075
	5087c	0	2.06544	91.17882	0.94577	0.00037	0.00394	5.76892	0.02837	0.0003
	5087d	0	2.78543	89.82878	1.73742	0	0.00405	5.60599	0.03159	0.0002
pyr #31	**5088b**	**0.00061**	**1.05795**	**97.47575**	**0.65444**	**0**	**0.0089**	**0.76004**	**0.04077**	**0.00105**
	5088c	**0.00064**	**0.5362**	**98.32498**	**0.59394**	**0**	**0.00785**	**0.51159**	**0.02448**	**0.00032**
	5088d	**0.00097**	**0.99353**	**96.67372**	**1.71206**	**0**	**0.02153**	**0.56685**	**0.0311**	**0.00023**
	5088e	**0.0011**	**0.62303**	**95.58051**	**2.83893**	**0**	**0.03792**	**0.88576**	**0.03269**	**8E-05**
pyr L3	5053a	0	0.04029	99.46317	0.26446	6E-05	0.00313	0.22781	0	0.00022
	5053b	0	0.06516	98.84677	0.46193	0.00044	0.00784	0.60658	0.00107	0.00058
	5053c	0	0.06084	99.12108	0.34983	0.00047	0.00765	0.4316	0.00178	0.00056
	5053d	0	0.018	99.36871	0.21457	0.00011	0.00319	0.39213	0	0.00032
	5056b	0	0.07142	98.90928	0.11241	0.00021	0.0014	0.90224	0	0.00036
	5056c	0	0.10643	98.97886	0.09497	0.00011	0.00117	0.81498	0.00096	0.0003
	5056d	0	0.13099	98.82702	0.0765	4E-05	0.00101	0.96284	0	0.00033

Table B-2. Data tables for calculations of boiling model for the stage 1 and 2 fluids.

First stage quartz, 5083b

CH4	0.2018	0.20185
H2O	94.89089	94.91243
N2	0.98213	0.98235
H2S	0.00215	0.00215
Ar	0.0031	0.00310
CO2	3.87963	3.88051
CnHn	0.0172	0.01720
SO2	0.00041	0.00041
Total	99.97731	100

t(c)	y	B(CO2)	1/(1+y*(B(CO2-1)	CL(CO2)
330		14.31199	1	3.88051
325	0.01	16.22931	0.86783	3.367642
320	0.01	18.40348	0.85176	2.868434
315	0.01	20.86892	0.83424	2.392976
310	0.01	23.66465	0.81523	1.950828
305	0.01	26.83490	0.79469	1.550307
300	0.01	30.42986	0.77262	1.197797
295	0.01	34.50643	0.74903	0.897183

t(c)	y	B(CH4)	1/(1+y*(BCH4-1))	CL(CH4)
330		32.68888	1	0.201846
325	0.01	38.33099	0.72817	0.146978
320	0.01	44.94693	0.69470	0.102105
315	0.01	52.70478	0.65918	0.067305
310	0.01	61.80164	0.62188	0.041856
305	0.01	72.46862	0.58320	0.02441
300	0.01	84.97673	0.54355	0.013268
295	0.01	99.64374	0.50341	0.006679

t(c)	y	B(H2S)	1/(1+y*(BH2S-1))	CL(H2S)
330		6.56750	1	0.00215
325	0.01	7.35275	0.94027	0.002022
320	0.01	8.23190	0.93256	0.001886
315	0.01	9.21616	0.92408	0.001742
310	0.01	10.31811	0.91476	0.001594
305	0.01	11.55181	0.90455	0.001442
300	0.01	12.93302	0.89339	0.001288
295	0.01	14.47938	0.88122	0.001135

t(c)	CO2/10	CH4	H2S*100	%CO2/10	%CH4	%H2S*100	0.5%CO2/10+%H2S*100	
330	0.388051	0.20185	0.215049	48.20835	25.07571	26.71594	50.82012	5083b
325	0.336764	0.14698	0.202203	49.09492	21.42702	29.47806	54.02552	
320	0.286843	0.10211	0.188566	49.66855	17.68012	32.65133	57.48560	
315	0.239298	0.06731	0.174250	49.76526	13.99708	36.23766	61.12029	
310	0.195083	0.04186	0.159397	49.22158	10.56077	40.21765	64.82844	
305	0.155031	0.02441	0.144183	47.90456	7.54281	44.55262	68.50490	
300	0.11978	0.01327	0.128812	45.74193	5.06690	49.19117	72.06213	
295	0.089718	0.00668	0.113511	42.74153	3.18204	54.07643	75.44719	

Second stage quartz #10, 5061a

CH4	0.30053	0.30056
H2O	96.62299	96.63116
N2	0.21696	0.21698
H2S	0.00587	0.00587
Ar	0.00182	0.00182
CO2	2.83387	2.83411
CnHn	0.00891	0.00891
SO2	0.00059	0.00059
	99.99154	100

t(c)	y	B(CO2)	1/(1+y*(B(CO2-1)	CL(CO2)
320		18.40348	1	2.83411
315	0.01	20.86892	0.83424	2.364341
310	0.01	23.66465	0.81523	1.927483
305	0.01	26.83490	0.79469	1.531756
300	0.01	30.42986	0.77262	1.183464
295	0.01	34.50643	0.74903	0.886447
290	0.01	39.12911	0.72396	0.641753
285	0.01	44.37108	0.69749	0.447617

t(c)	y	B(CH4)	1/(1+y*(BCH4-1))	CL(CH4)
320		44.94693	1	0.300555
315	0.01	52.70478	0.65918	0.198119
310	0.01	61.80164	0.62188	0.123207
305	0.01	72.46862	0.58320	0.071854
300	0.01	84.97673	0.54355	0.039056
295	0.01	99.64374	0.50341	0.019661
290	0.01	116.84227	0.46330	0.009109
285	0.01	137.00929	0.42371	0.00386

t(c)	y	B(H2S)	1/(1+y*(BH2S-1))	CL(H2S)
320		8.23190	1	0.00587
315	0.01	9.21616	0.92408	0.005425
310	0.01	10.31811	0.91476	0.004962
305	0.01	11.55181	0.90455	0.004489
300	0.01	12.93302	0.89339	0.00401
295	0.01	14.47938	0.88122	0.003534
290	0.01	16.21063	0.86798	0.003067
285	0.01	18.14889	0.85361	0.002618

t(c)	CO2/10	CH4	H2S*100	%CO2/10	%CH4	%H2S*100	0.5%CO2/10+%H2S*100	
320	0.283411	0.30056	0.587050	24.20214	25.66621	50.13165	62.23272	5061a
315	0.236434	0.19812	0.542479	24.19923	20.27761	55.52316	67.62278	
310	0.192748	0.12321	0.496239	23.73181	15.16963	61.09855	72.96446	
305	0.153176	0.07185	0.448874	22.72959	10.66233	66.60807	77.97287	
300	0.118346	0.03906	0.401020	21.19297	6.99398	71.81305	82.40954	
295	0.088645	0.01966	0.353386	19.19996	4.25853	76.54151	86.14149	
290	0.064175	0.00911	0.306731	16.88756	2.39704	80.71540	89.15918	
285	0.044762	0.00386	0.261830	14.41827	1.24324	84.33850	91.54763	

APPENDIX C
$^{40}Ar/^{39}Ar$ analyses

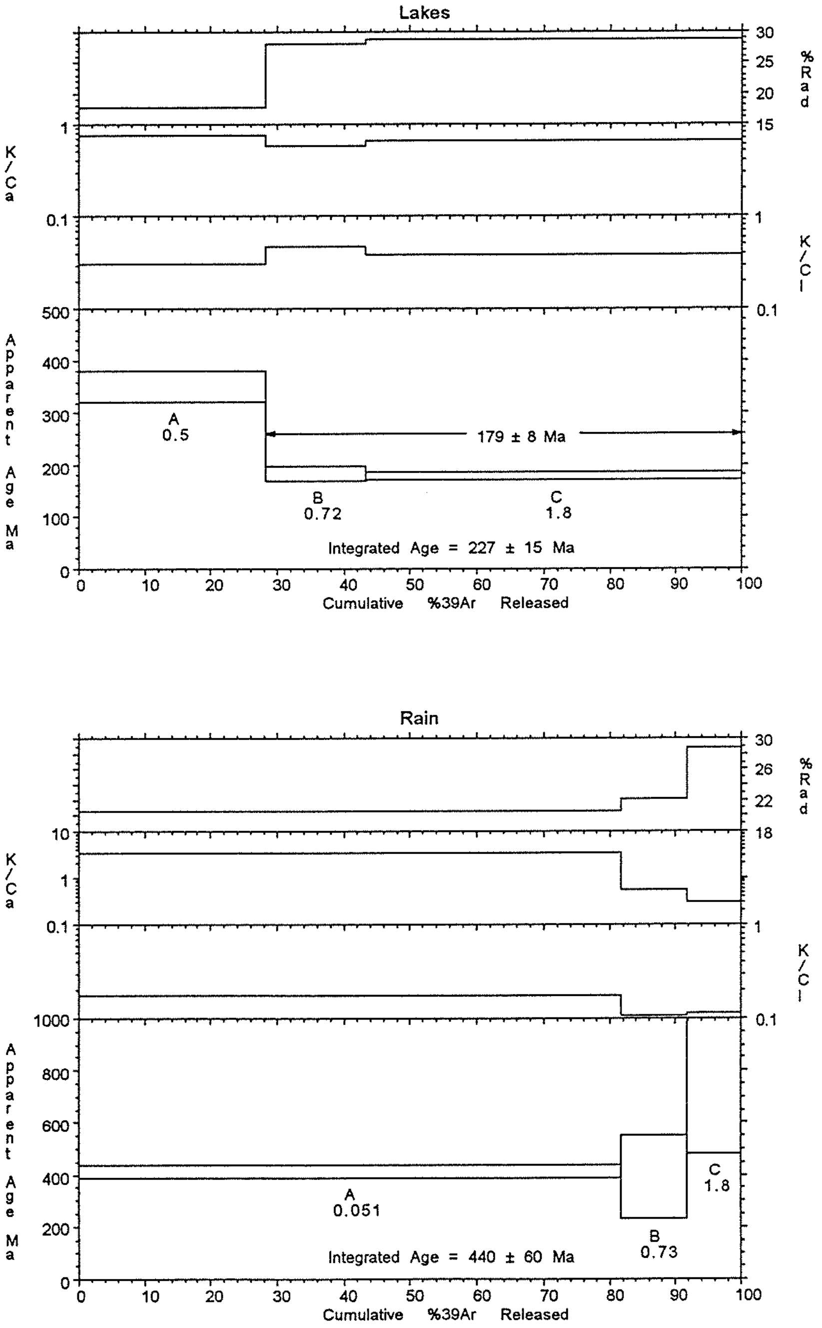

Figure C-1. Age spectra for laser analyses.

Figure C-1 continued

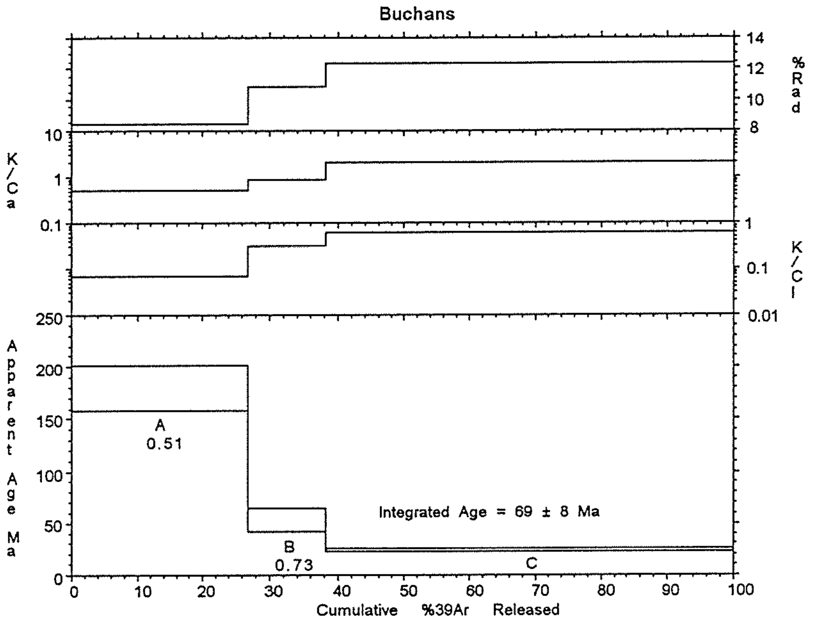

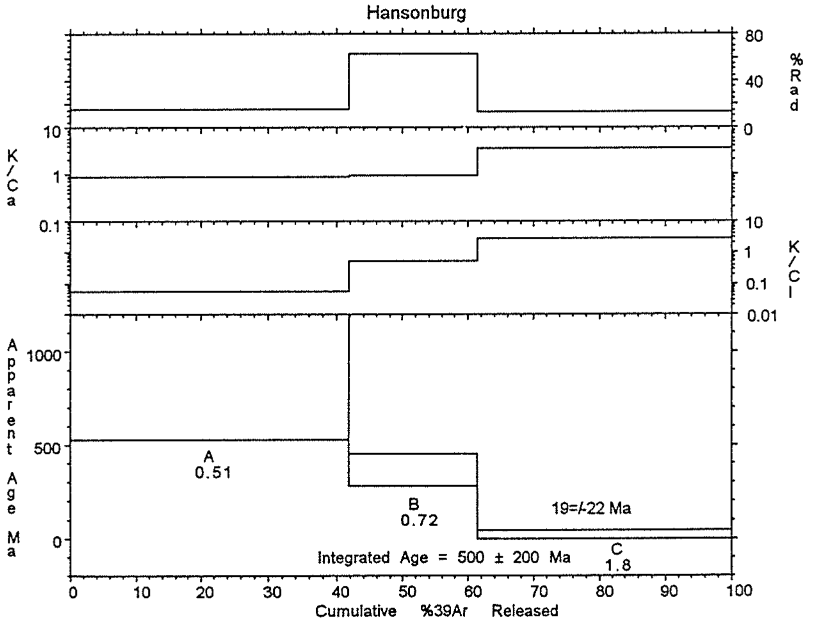

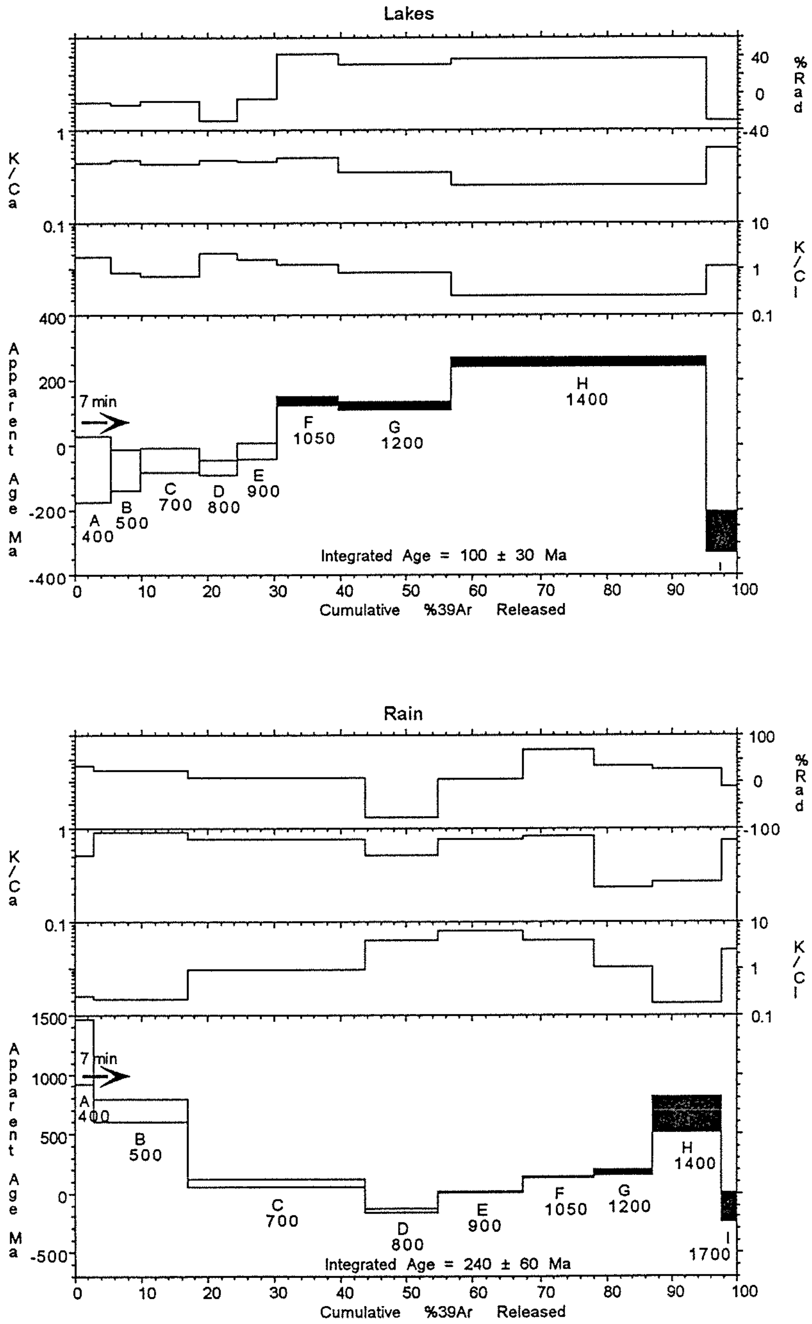

Figure C-2. Age spectra for furnace analyses. Black colored steps represent reliable data. Gettering time is marked with an arrow.

Figure C-2 continued

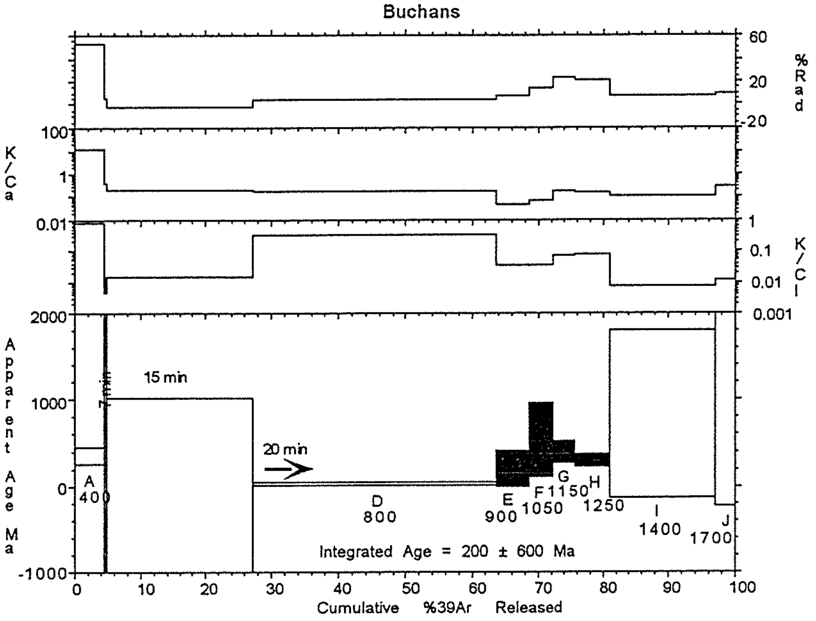

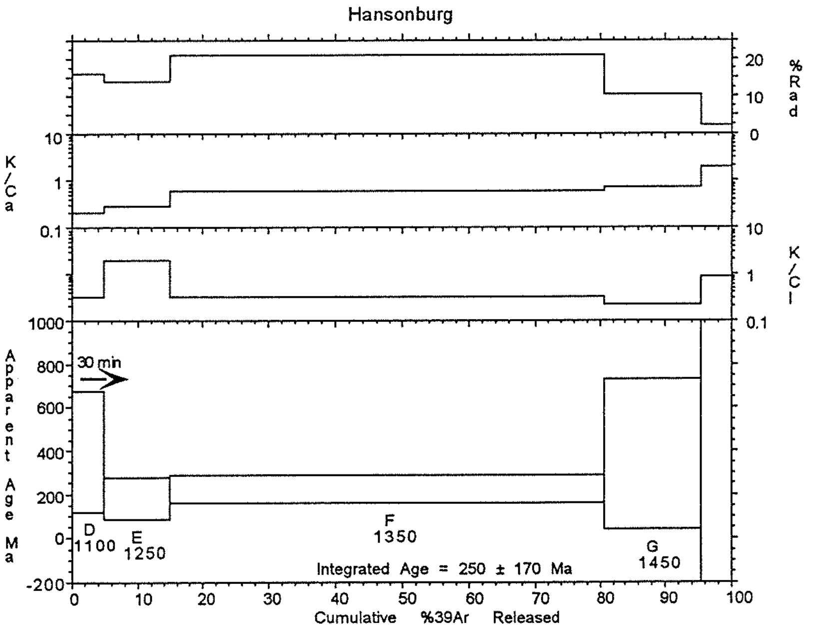

Figure C-2 continued

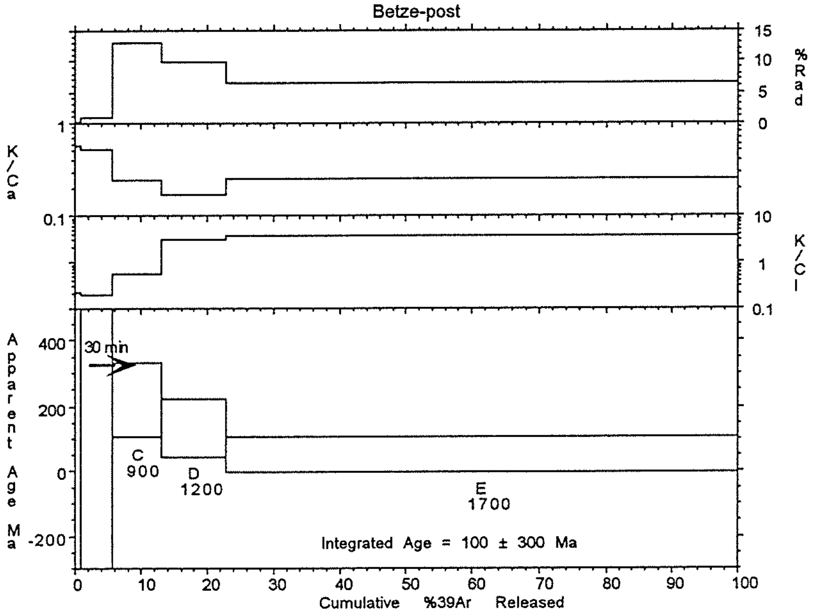

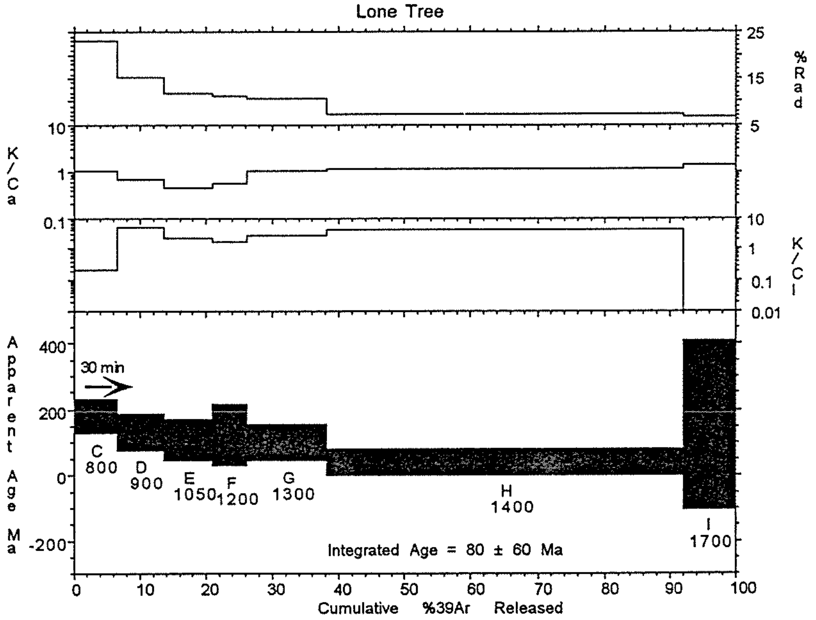

Table C-1. Results of laser step heating analyses for barite samples

Run #	Power	40/39	37/39	36/39	39K moles	K/Ca	Cl/K	%40*	%39Ar	Age	±Err
Lone Tree		**barite**	**? mg**	**J=0.002300**							
2364-01A	0.29	157.85	0	4.65e-01	1.3e-17	-	0.01	13.0	3.64	83	47
2364-01B	0.42	181.98	1.7e-02	6.09e-01	2.4e-17	29.9	0.007	1.1	10.36	8	26
2364-01C	0.65	17.93	2.93e-04	4.62e-02	2.0e-16	1741.9	-0.0001	23.7	66.39	17.6	1.8
2364-01D	1.70	26.53	1.94e-03	6.92e-02	1.2e-16	263.0	0.0025	22.8	100.00	24.9	3.4
total gas age					3.6e-16				n=4	22.6	6.1
Lone Tree		**barite**	**11 mg**	**J=0.001591**							
2919-01A	0.39	5320	8.55e-01	1.81e+01	1.2e-17	0.6	0.23	-0.7	32.59	-109	-
2919-01B	0.73	172	6.68e-01	5.32e-01	1.2e-17	0.76	0.07	8.6	65.50	42	57
2919-01C	1.60	124	6.53e-01	3.85e-01	1.2e-17	0.78	0.08	8.5	100.00	30	52
total gas age					3.6e-17				n=3	-11	410
Lone Tree		**barite**	**5 mg**	**J=0.001591**							
2919-02A	0.39	1860	3.96e-01	6.18e+00	1.2e-17	1.3	0.23	2.0	27.2	103	572
2919-02B	0.71	128	2.52e-01	3.24e-01	1.4e-17	2.0	0.02	25.0	59.45	89	42
2919-02C	1.60	194	4.67e-01	5.44e-01	1.8e-17	1.1	0.02	17.3	100.00	93	63
total gas age					4.5e-17				n=3	94	195
Lone Tree		**barite**	**5.4 mg**	**J=0.001591**							
2919-03A	0.38	881	7.66e-01	2.84e+00	1.1e-17	0.67	0.08	4.7	27.50	114	312
2919-03B	0.72	132	2.70e-01	3.60e-01	1.3e-17	1.9	0.05	19.5	60.80	72	58
2919-03C	1.60	182	2.68e-01	5.29e-01	1.5e-17	1.9	0.04	13.9	100.00	70	79
total gas age					3.9e-17				n=3	83	136
Lone Tree		**barite**	**8.3 mg**	**J=0.001591**							
2919-04A	0.38	3270	7.28e-02	1.09e+01	1.9e-17	7.0	0.11	1.7	31.10	156	642
2919-04B	0.72	132	1.10e-01	3.39e-01	1.2e-17	4.6	0.02	23.8	50.33	87	54
2919-04C	1.60	187	2.37e-01	5.83e-01	3.0e-17	2.2	0.01	7.9	100.00	42	38
total gas age					6.1e-17				n=3	86	229
Lone Tree		**barite**	**5.6 mg**	**J=0.001591**							
2919-05A	0.38	1710	0.00e+00	5.54e+00	1.2e-17	-	0.11	4.5	30.46	209	471
2919-05B	0.73	178	2.41e-01	4.45e-01	1.0e-17	2.1	0.04	26.3	56.99	129	69
2919-05C	1.60	168	2.60e-02	4.19e-01	1.7e-17	20.0	0.005	26.4	100.00	123	62
total gas age					3.9e-17				n=3	151	188

Table C-1 continued

Run #	Power	40/39	37/39	36/39	39K moles	K/Ca	Cl/K	%40*	%39Ar	Age	±Err
Getchell		**barite**	**8.1 mg**	**J=0.001591**							
2920-01A	0.38	15000	6.73e-01	4.87e+01	7.0e-18	0.76	0.65	4.0	18.61	1215	4190
2920-01B	0.72	434	1.33e+00	1.12e+00	1.8e-17	0.38	0.09	23.8	66.27	274	56
2920-01C	1.60	139	1.94e+00	3.08e-01	1.3e-17	0.26	0.09	34.7	100.00	133	36
total gas age					3.8e-17				n=3	402	819
Getchell		**barite**	**4.2 mg**	**J=0.001591**							
2920-02A	0.38	800	8.03e+00	2.44e+00	4.7e-17	0.06	0.51	9.9	58.64	214	55
2920-02B	0.72	216	2.72e+01	5.66e-01	1.5e-17	0.02	0.34	23.4	77.81	142	49
2920-02C	1.60	673	1.10e+01	1.99e+00	1.8e-17	0.05	0.23	12.7	100.00	231	140
total gas age					8.0e-17				n=3	204	73
Lakes		**barite**	**6.16 mg**	**J=0.001604**							
2770-01A	0.5	756.0	6.83e-01	2.11e+00	9.3e-17	0.75	0.31	17.7	28.09	350	29
2770-01B	0.72	236.0	8.83e-01	5.73e-01	5.0e-17	0.58	0.2	28.1	43.18	182	14
2770-01C	1.78	227.0	7.81e-01	5.48e-01	1.9e-16	0.65	0.25	28.6	100.0	178.8	8.4
total gas age					3.3e-16				n=3	227	15
Rain		**barite**	**4.10 mg**	**J=0.001599**							
2771-01A	0.05	783.0	1.50e-01	2.10e+00	1.4e-16	3.4	0.54	20.6	81.66	413	26
2771-01B	0.73	677.0	9.37e-01	1.78e+00	1.7e-17	0.54	0.91	22.2	91.71	388	160
2771-01C	1.79	1200.0	1.65E+00	2.90E+00	1.4e-17	0.31	0.83	28.8	100.0	795	315
total gas age					1.7e-16				n=3	442	64
Buchans		**barite**	**4.99 mg**	**J=0.001558**							
2772-01A	0.51	776.0	1.01e+00	2.40e+00	2.2e-16	0.51	1.4	8.5	26.76	175	21
2772-01B	0.73	175.0	5.64e-01	5.27e-01	9.5e-17	0.90	0.32	10.9	38.13	52	11
2772-01C	1.78	68.3	2.52e-01	2.02e-01	5.1e-16	2.00	0.16	12.4	100.0	23.6	1.8
total gas age					8.3e-16				n=3	67.6	8.0
Hansonburg		**barite**	**2.15 mg**	**J=0.001601**							
2773-01A	0.51	2850.0	5.82e-01	8.09e+00	1.5e-17	0.88	1.8	16.1	41.75	994	465
2773-01B	0.72	224.0	5.43e-01	2.84e-01	7.2e-18	0.94	0.18	62.5	61.32	364	83
2773-01C	1.78	48.3	1.46e-01	1.41e-01	1.4e-17	3.50	0.04	13.9	100.0	19	22
total gas age					3.7e-17				n=3	493	219

Table C-1 continued

Run #	Power	40/39	37/39	36/39	39K moles	K/Ca	Cl/K	%40*	%39Ar	Age	±Err
Betze-post		**barite**	**4.00 mg**	**J=0.001584**							
2774-01A	0.50	158.0	1.30e+00	5.50e-01	4.3e-17	0.39	0.01	-3.0	67.72	-13	17
2774-01B	0.73	106.0	2.20e+00	4.21e-01	7.2e-18	0.23	0.06	-17.2	78.96	-52	80
2774-01C	1.78	83.1	1.06e+01	2.87e-01	1.3e-17	0.05	0.03	-1.2	100.0	-3	41
total gas age					6.4e-17				n=3	-16	28
Bredehorn		**barite**	**2.00 mg**	**J=0.001562**							
2775-01A	0.51	19200	1.14e+00	6.16e+01	1.0e-17	0.45	0.54	5.2	54.09	-	-
2775-01B	0.73	9360	2.87e-01	4.06e+01	5.9e-18	1.80	0.18	3.5	84.88	753.3	-
2775-01C	1.80	4830	4.60e-01	1.51e+01	2.9e-18	1.10	-0.006	7.5	100.0	806.2	-
total gas age					1.9e-17				n=3	-	-

Table C-2. Results of furnace step heating analyses for barite samples

Run #	Temp	40/39	37/39	36/39	39K moles	K/Ca	Cl/K	%40*	%39Ar	Age	±Err
Lakes		**barite**	**97.6 mg**	**J=0.001603**							
2855-01A	401	235.0	1.15e+00	8.81e-01	2.5e-16	0.44	0.054	-10.6	5.38	-73	103
2855-01B	500	202.0	1.07e+00	7.69e-01	2.1e-16	0.48	0.11	-12.7	9.90	-75	65
2855-01C	700	170.0	1.18e+00	6.27e-01	4.2e-16	0.43	0.14	-8.8	18.81	-43	36
2855-01D	800	74.9	1.08e+00	3.30e-01	2.6e-16	0.47	0.044	-30.2	24.36	-66	23
2855-01E	900	96.3	1.12e+00	3.44e-01	2.8e-16	0.46	0.061	-5.6	30.30	-15	25
2855-01F	1050	115.0	1.01e+00	2.20e-01	4.3e-16	0.51	0.078	43.3	39.57	138	14
2855-01G	1200	140.0	1.47e+00	3.26e-01	8.1e-16	0.35	0.12	31.4	56.76	122	10
2855-01H	1400	258.0	2.02e+00	5.52e-01	1.8e-15	0.25	0.38	36.8	95.24	255	14
2855-01I	1700	293.0	8.12e-01	1.28e+00	2.2e-16	0.63	0.084	-29.3	100.0	-267	63
total gas age					4.7e-15				n=9	103	26
Rain		**barite**	**122.7 mg**	**J=0.001599**							
2856-01A	400	1680.0	9.71e-01	3.27e+00	9.8e-17	0.53	0.39	34.8	2.85	-	278
2856-01B	500	1230.0	5.69e-01	3.17e+00	4.9e-16	0.90	0.42	24.0	17.00	700	94
2856-01C	700	328.0	6.67e-01	1.01e+00	9.2e-16	0.77	0.10	9.0	43.76	83	33
2856-01D	800	62.4	9.75e-01	3.71e-01	3.7e-16	0.52	0.024	-75.9	54.68	-142	14
2856-01E	900	59.6	6.74e-01	1.89e-01	4.4e-16	0.76	0.015	6.5	67.37	11.2	8.2
2856-01F	1050	72.2	6.16e-01	7.83e-02	3.7e-16	0.83	0.023	68.0	78.09	136.3	7.8
2856-01G	1200	182.0	2.15e+00	4.01e-01	3.1e-16	0.24	0.087	35.1	86.99	175	25
2856-01H	1400	1120.0	1.87e+00	2.85e+00	3.6e-16	0.27	0.51	24.8	97.62	664	152
2856-01I	1700	313.0	6.82e-01	1.19e+00	8.2e-17	0.75	0.037	-12.6	100.0	-117	127
total gas age					3.4e-15				n=9	239	55
Buchans		**barite**	**88.0 mg**	**J=0.001558**							
2857-01A	400	256.0	4.17e-02	4.09e-01	2.6e-17	12.0	0.11	52.8	3.83	345	95
2857-01B	500	19500.0	1.24e+00	6.24e+01	2.6e-18	0.41	22.0	5.6	4.20	-	-
2857-01C	700	3810.0	2.62e+00	1.31e+01	1.3e-16	0.19	6.8	-1.3	23.11	-146	-
2857-01D	800	280.0	2.70e+00	9.12e-01	2.1e-16	0.19	0.28	4.0	54.24	31	15
2857-01E	900	952.0	1.07e+01	2.98e+00	3.0e-17	0.05	2.7	7.7	58.65	196	202
2857-01F	1050	1460.0	6.65e+00	4.22e+00	3.2e-17	0.08	2.8	14.6	63.29	517	419
2857-01G	1150	680.0	2.74e+00	1.77e+00	3.2e-17	0.19	1.4	23.2	67.94	397	128
2857-01H	1250	527.0	3.12e+00	1.41e+00	4.8e-17	0.16	1.2	21.1	74.92	289	73
2857-01I	1400	4830.0	4.79e+00	1.51e+01	1.4e-16	0.11	13.0	7.5	95.90	807	954
2857-01J	1700	4850.0	1.75e+00	1.49e+01	2.8e-17	0.29	8.4	9.2	100.0	950	-
total gas age					6.8e-16				n=10	281	599

Table C-2 continued

Run #	Temp	40/39	37/39	36/39	39K moles	K/Ca	Cl/K	%40*	%39Ar	Age	±Err
Hansonburg		**barite**	**69 mg**	**J=0.001601**							
2858-01A	501	100000	0.0	2.88e+02	1.1e-18	-	50.0	15.0	0.41	-	-
2858-01B	700	73800	0.0	2.05e+02	4.8e-18	-	2.0	17.8	2.36	-	-
2858-01C	900	6820	6.03e+00	1.94e+01	4.3e-18	0.08	7.1	15.8	4.10	-	-
2858-01D	1100	960	2.48e+00	2.74e+00	1.1e-17	0.21	0.29	15.8	8.65	393	280
2858-01E	1250	482	1.76e+00	1.41e+00	2.4e-17	0.29	0.05	13.5	18.36	179	94
2858-01F	1350	396	8.53e-01	1.06e+00	1.6e-16	0.60	0.29	20.7	81.52	222	66
2858-01G	1450	1410	7.14e-01	4.28e+00	3.5e-17	0.71	0.42	10.2	95.58	373	350
2858-01H	1700	2320	2.63e-01	7.72e+00	1.1e-17	1.9	0.11	1.8	100.0	117	
total gas age					2.5e-16				n=8	397	365
Betze-post		**barite**	**65.3 mg**	**J=0.001584**							
2859-01A	500	7120	8.83e-01	2.41e+01	1.8e-18	0.58	0.43	-0.1	0.88	-11	-
2859-01B	700	7040	9.73e-01	2.37e+01	9.7e-18	0.52	0.50	0.6	5.61	114	-
2859-01C	900	608	2.08e+00	1.79e+00	1.5e-17	0.25	0.17	12.8	13.11	210	113
2859-01D	1200	486	3.06e+00	1.49e+00	2.0e-17	0.17	0.03	9.4	22.70	126	89
2859-01E	1700	273	2.03e+00	8.67e-01	1.6e-16	0.25	0.02	6.1	100.0	47	53
total gas age					2.0e-16				n=5	69	281
Bredehorn		**barite**	**159.3 mg**	**J=0.001562**							
2854-01A	401	185	9.59e-01	5.17e-01	2.8e-16	0.53	0.05	17.2	6.27	87	50
2854-01B	500	4550	1.14e+00	1.29e+01	1.9e-16	0.45	0.55	16.2	10.47	-	555
2854-01C	700	2810	1.23e+00	8.70e+00	3.2e-16	0.42	0.49	8.6	17.54	580	275
2854-01D	800	279	8.55e-01	8.06e-01	1.4e-16	0.60	0.16	14.8	20.66	112	48
2854-01E	900	619	1.17e+00	1.81e+00	7.3e-17	0.44	0.10	13.4	22.28	220	134
2854-01F	1050	935	1.39e+00	2.86e+00	5.6e-17	0.37	0.13	9.7	23.53	239	198
2854-01G	1200	513	8.23e-01	1.75e+00	4.9e-16	0.62	0.05	-0.7	34.50	-10	100
2854-01H	1700	1840	8.12e-01	6.16e+00	2.9e-15	0.63	0.09	1.0	100.0	53	318
total gas age					4.5e-15				n=8	148	271

Table C-2 continued

Run #	Temp	40/39	37/39	36/39	39K moles	K/Ca	Cl/K	%40*	%39Ar	Age	±Err
Lone Tree		**barite**	**87.1 mg**	**J=0.001591**							
2860-01A	501	1410	0.0	4.95e+00	8.9e-18	-	0.09	-3.5	1.93	-147	762
2860-01B	700	2560	8.73e-02	8.67e+00	4.0e-17	5.8	0.41	-0.2	10.50	-16	323
2860-01C	800	287	4.90e-01	7.49e-01	2.8e-17	1.0	0.47	22.8	16.50	178	51
2860-01D	900	302	7.52e-01	8.69e-01	2.9e-17	0.68	0.02	15.1	22.73	126	55
2860-01E	1050	322	1.09e+00	9.64e-01	3.0e-17	0.47	0.04	11.6	29.30	104	60
2860-01F	1200	380	9.22e-01	1.14e+00	2.2e-17	0.55	0.05	11.1	33.96	117	91
2860-01G	1300	336	4.70e-01	1.02e+00	4.9e-17	1.1	0.04	10.5	44.64	98	52
2860-01H	1400	192	4.50e-01	6.06e-01	2.2e-16	1.1	0.02	6.9	92.79	37	38
2860-01I	1700	808	3.57e-01	2.56e+00	3.3e-17	1.4	-0.0004	6.5	100.0	144	257
total gas age					4.6e-16				n=9	65	100

Table C-3. The concentrations of potassium in ppm calculated from the 39Ar signal.

Laser analyses

Sample ID	J	Lamda	Lamda(e)	39Ar	40K (moles)	Total K (moles)	% Abun.	Weight (mg)	Total K (ppm)
Lakes	0.001604	5.543E-10	5.8E-11	3.3E-16	2E-12	1.682E-08	0.0001167	6.16	106.75413
Rain	0.001599	5.543E-10	5.8E-11	1.7E-16	1E-12	8.692E-09	0.0001167	4.1	82.884326
Buchans	0.001558	5.543E-10	5.8E-11	8.3E-16	5.1E-12	4.355E-08	0.0001167	4.99	341.24469
Hansonburg	0.001601	5.543E-10	5.8E-11	3.7E-17	2.2E-13	1.889E-09	0.0001167	2.15	34.357989
Betzepost	0.001584	5.543E-10	5.8E-11	6.4E-17	3.9E-13	3.303E-09	0.0001167	4	32.286474
Bredehorn	0.001562	5.543E-10	5.8E-11	1.9E-17	1.2E-13	9.944E-10	0.0001167	2	19.440095
Lone Tree 2919-01	0.001591	5.543E-10	5.8E-11	3.6E-17	2.2E-13	1.85E-09	0.0001167	11	6.5749953
Lone Tree 2919-02	0.001591	5.543E-10	5.8E-11	4.5E-17	2.7E-13	2.312E-09	0.0001167	5	18.081237
Lone Tree 2919-03	0.001591	5.543E-10	5.8E-11	3.9E-17	2.3E-13	2.004E-09	0.0001167	5.4	14.509635
Lone Tree 2919-04	0.001591	5.543E-10	5.8E-11	6.1E-17	3.7E-13	3.134E-09	0.0001167	8.3	14.765133
Lone Tree 2919-05	0.001591	5.543E-10	5.8E-11	3.9E-17	2.3E-13	2.004E-09	0.0001167	5.6	13.991433
Getchell 2920-01	0.001591	5.543E-10	5.8E-11	3.8E-17	2.3E-13	1.953E-09	0.0001167	8.1	9.4250618
Getchell 2920-02	0.001591	5.543E-10	5.8E-11	8E-17	4.8E-13	4.111E-09	0.0001167	4.2	38.267168
Lakes*	0.0016036	5.543E-10	5.8E-11	4.7E-15	2.8E-11	2.396E-07	0.0001167	97.6	95.986758
Rain*	0.0015993	5.543E-10	5.8E-11	3.4E-15	2E-11	1.738E-07	0.0001167	122.7	55.379923
Buchans*	0.0015581	5.543E-10	5.8E-11	6.8E-16	4.2E-12	3.568E-08	0.0001167	88	15.85226
Hansonburg*	0.0016018	5.543E-10	5.8E-11	2.5E-16	1.5E-12	1.276E-08	0.0001167	69	7.2298353
Betzepost*	0.0015842	5.543E-10	5.8E-11	2E-16	1.2E-12	1.032E-08	0.0001167	65.3	6.17971
Bredehorn*	0.0015627	5.543E-10	5.8E-11	4.5E-15	2.7E-11	2.354E-07	0.0001167	159.3	57.780548
Lone Tree*	0.0015911	5.543E-10	5.8E-11	4.6E-16	2.8E-12	2.364E-08	0.0001167	87.1	10.609616

* Furnace analyses